Astronomy Letters, Vol. 28, No. 12, 2002, pp. 793–798. Translated from Pis'ma v Astronomicheskiĭ Zhurnal, Vol. 28, No. 12, 2002, pp. 883–888.

The Baryon Mass Distribution for Nearby Galaxy Clusters

A. A. Voevodkin*, A. A. Vikhlinin, and M. N. Pavlinsky

Space Research Institute, Russian Academy of Sciences, ul. Profsoyuznaya 84/32, Moscow, 117810 Russia

Received June 28, 2002

Abstract—Based on ROSAT X-ray data, we constructed the baryon mass function for a statistically complete sample of galaxy clusters at redshifts of 0.01–0.1. Since the derived function is similar to the total mass function for clusters, it can be used to determine cosmological parameters. © *2002 MAIK "Nauka/Interperiodica".*

Key words: *theoretical and observational cosmology; galaxy clusters; large-scale structure of the Universe; baryon mass function.*

INTRODUCTION

Studies of galaxy clusters provide data for the experimental determination of cosmological parameters. Theory predicts the significant dependence of the cluster mass function on cosmological parameters. This dependence was used in a number of recent experimental works (see, e.g., Markevitch 1998; Henry 2000). However, because of the difficulties arising in experimental mass determination, instead of direct measurements of the cluster mass, the authors of such studies commonly use its relationship to the intergalactic-gas temperature, which introduces additional systematic uncertainties (see, e.g., Evrard *et al.* 2002).

In this paper, we suggest a slightly different approach to investigating the mass function. If the fraction of baryons in a cluster, $f_{\rm bar}$, does not depend on its total mass, as predicted theoretically (White *et al.* 1993) and increasingly confirmed experimentally in recent years (see, e.g., Allen *et al.* 2002), then the mass function for clusters including their dark matter can be determined from the baryon mass function. In turn, its comparison with theory will make it possible to determine cosmological parameters. This work continues our previous study (Voevodkin *et al.* 2002) of galaxy-cluster parameters using ROSAT X-ray data. We describe in detail the derivation of the baryon mass function for a new, expanded sample of clusters.

All numerical values were obtained for the following cosmological parameters: $H_0 = 50$ km s^{-1} Mpc^{-1}, $\Omega = 1$, and $\Lambda = 0$.

*E-mail: lesha@hea.iki.rssi.su

THE SAMPLE OF CLUSTERS

Our sample of clusters was drawn from the HIFLUSS catalog described by Reiprich and Bohringer (2002). In turn, this catalog is based on the ROSAT all-sky survey. The sky regions near the Galactic plane and those corresponding to the Magellanic Clouds and the nearby Virgo cluster of galaxies were excluded when compiling the catalog, because the X-ray sources located in these regions make it difficult to detect clusters in them and to measure their parameters.

We additionally selected clusters from the HIFLUSS catalog that satisfied the following conditions:

(1) the X-ray flux in the 0.5- to 2.0-keV band corrected for Galactic absorption exceeds 1.4×10^{-11} erg s^{-1} cm^{-2};

(2) the redshift lies within the range $0.01 \le z \le 0.1$.

The motivation for choosing these criteria can be found in Voevodkin *et al.* (2002). The resulting sample contains clusters with a wide range of masses.

Table 1 lists the selected clusters, measured X-ray fluxes and luminosities, masses, and other cluster parameters determined here.

MEASURING THE CLUSTER MASSES

We determined the cluster masses within the radius corresponding to the baryon overdensity $\delta = 324$ relative to the mean baryon density in the Universe, $\rho_{\rm bar} = (1+z)^3 5.55 M_\odot/{\rm kpc}^3$, which may be considered to be known from the comparison of the theory for primordial nucleosynthesis with light-element abundance observations (Burles *et al.* 2001). It is for this δ that Jenkins *et al.* (2001) performed a detailed

1063-7737/02/2812-0793$22.00

Table 1. A list of clusters and their properties

Cluster	z	f_x,[a] 10^{-11} erg s^{-1} cm^{-2}	L_x,10^{44} erg s^{-1}	M_{324}, 10^{14} $M_\odot$	$M_{324}^{\rm gas}$, 10^{14} $M_\odot$	r_{324}, Mpc
2A0335	0.0349	6.82	3.53	1.53 ± 0.19	1.23 ± 0.19	2.64
A85	0.0556	4.33	5.67	2.60 ± 0.30	2.20 ± 0.33	3.08
A119	0.0442	2.42	2.00	2.66 ± 0.26	2.23 ± 0.30	3.15
A262	0.0155	4.67	0.48	0.60 ± 0.12	0.44 ± 0.10	1.98
A399	0.0715	1.76	3.80	3.14 ± 0.74	2.64 ± 0.71	3.23
A400	0.0238	1.65	0.39	0.73 ± 0.06	0.55 ± 0.07	2.09
A401	0.0739	3.17	7.32	5.84 ± 0.64	5.07 ± 0.75	3.97
A478	0.0882	4.54	14.90	5.22 ± 0.58	4.52 ± 0.67	3.78
A496	0.0328	5.38	2.46	1.68 ± 0.21	1.37 ± 0.22	2.73
A576	0.0389	1.60	1.03	0.99 ± 0.31[b]	–	–
A754	0.0542	4.36	5.40	4.12 ± 0.41	3.55 ± 0.50	3.60
A1060	0.0137	6.18	0.49	0.59 ± 0.12	0.44 ± 0.10	1.96
A1367	0.0214	4.82	0.94	1.17 ± 0.18	0.94 ± 0.18	2.44
A1644	0.0474	2.27	2.16	2.44 ± 0.52	2.01 ± 0.49	3.04
A1651	0.0860	1.53	4.79	2.74 ± 0.41	2.30 ± 0.42	3.05
A1656	0.0231	18.30	4.14	4.13 ± 0.48	3.51 ± 0.54	3.71
A1736	0.0461	1.72	1.55	1.37 ± 0.42[b]	–	–
A1795	0.0622	3.91	6.40	2.42 ± 0.21	2.03 ± 0.26	2.99
A2029	0.0766	4.27	10.54	4.62 ± 0.57	3.94 ± 0.63	3.66
A2052	0.0353	2.97	1.57	0.88 ± 0.14	0.69 ± 0.13	2.19
A2063	0.0355	2.48	1.33	1.19 ± 0.18	0.94 ± 0.17	2.44
A2065	0.0726	1.42	3.16	2.38 ± 0.73[b]	–	–
A2142	0.0894	4.00	13.45	7.78 ± 0.57	6.80 ± 0.84	4.31
A2147	0.0353	3.21	1.70	2.77 ± 0.45	2.28 ± 0.45	3.19
A2199	0.0299	6.53	2.48	1.56 ± 0.12	1.26 ± 0.16	2.67
A2256	0.0581	3.67	5.25	3.80 ± 0.30	3.25 ± 0.41	3.49
A2589	0.0416	1.61	1.18	0.85 ± 0.12	0.64 ± 0.11	2.20
A2634	0.0309	1.49	0.60	0.89 ± 0.10	0.71 ± 0.11	2.21
A2657	0.0400	1.74	1.18	1.13 ± 0.13	0.90 ± 0.13	2.37
A3112	0.0750	1.90	4.56	2.12 ± 0.32	1.76 ± 0.32	2.83
A3158	0.0591	2.30	3.40	2.40 ± 0.37	1.98 ± 0.37	2.99
A3266	0.0589	3.55	5.21	4.35 ± 0.42	3.76 ± 0.51	3.65
A3376	0.0455	1.40	1.23	1.17 ± 0.14	0.95 ± 0.15	2.39
A3391	0.0514	1.53	1.72	2.46 ± 0.34	2.01 ± 0.35	3.04
A3395	0.0506	1.93	2.09	3.59 ± 0.54	2.96 ± 0.54	3.45
A3526	0.0112	16.00	0.85	0.90 ± 0.14	0.69 ± 0.13	2.26
A3558	0.0480	4.07	3.98	3.51 ± 0.32	2.97 ± 0.39	3.44
A3562	0.0490	1.86	1.90	2.56 ± 0.24	2.12 ± 0.28	3.09
A3571	0.0391	7.53	4.87	3.34 ± 0.46	2.82 ± 0.48	3.41
A3581	0.0214	2.02	0.39	0.47 ± 0.15[b]	–	–
A3667	0.0556	4.61	6.02	6.30 ± 0.59	5.47 ± 0.74	4.14
A4038	0.0292	3.53	1.28	0.87 ± 0.14	0.67 ± 0.13	2.29
A4059	0.0460	2.01	1.80	1.23 ± 0.19	0.96 ± 0.18	2.43
EXO 0422	0.0390	1.90	1.23	1.14 ± 0.35[b]	–	–
Hydra A	0.0522	2.92	3.39	1.62 ± 0.18	1.32 ± 0.19	2.64
MKW3s	0.0453	2.10	1.83	1.10 ± 0.17	0.88 ± 0.16	2.34
MKW4	0.0210	1.44	0.27	0.38 ± 0.04	0.28 ± 0.04	1.63
NGC 1550	0.0120	2.67	0.16	0.19 ± 0.06	0.13 ± 0.04	1.35
NGC 507	0.0155	1.56	0.16	0.25 ± 0.03	0.17 ± 0.02	1.47
A S1101	0.0580	1.48	2.13	0.80 ± 0.11	0.63 ± 0.11	2.08

[a] The X-ray flux in the 0.5–2-keV band was measured within a circle of radius $7r_c$ (see the text for the definition of r_c).

[b] The baryon mass was determined from the M–L correlation.

theoretical analysis and derived a universal formula for the mass function of collapsed objects.

In our previous paper, we described in detail the technique for measuring the baryon mass (i.e., the total mass of the intergalactic gas and the stellar matter of galaxies) in clusters. Here, we give only a brief description. First, we measured the mass of the intergalactic gas using the deprojection method (Fabian *et al.* 1981) by assuming that its distribution is spherically symmetric. Then, using our empirical relation derived previously (Voevodkin *et al.* 2002),

$$\frac{M_*}{M_{\rm gas}} = 0.22\left[\frac{M_{\rm gas}}{10^{14}M_\odot}\right]^{-0.28}, \qquad (1)$$

which relates the gas mass in a cluster to the stellar mass, we calculated the total baryon mass in the cluster. The gas mass in the clusters A1060, A1644, and NGC 1550 was determined in a slightly different way. It was not possible to use the deprojection method due to the low measurement accuracy. Therefore, we determined the gas masses in these clusters by fitting the brightness profile with the β model.

Table 1 gives the measured gas and baryon masses and the corresponding overdensity radii r_{324}. The sample presented here contains more clusters than our previous sample used in analyzing the correlations between cluster baryon mass and temperature. Therefore, similar relations were also derived for the new data. The clusters A754, A1367, A2142, A2147, A2256, A3266, A3376, A3395, A3558, and A3667 appear to be in the process of merging two or more building blocks. As a result, the determination of their baryon mass is not completely reliable. Therefore, we also determined the parameters of the M–T correlation without these clusters. Table 2 gives the inferred parameters both for the correlation between cluster temperature and gas mass and for the correlation between cluster temperature and baryon mass.

Five of the 50 selected clusters (A576, A1736, A2065, A3581, and EXO 422) lacked high-quality X-ray data that allow their baryon masses to be measured. Therefore, we estimated them from the correlation between cluster mass and X-ray luminosity derived below.

THE BARYON MASS FUNCTION

Calculating the Volume

For the construction of the mass function from a flux-limited sample of objects, the volume in which a cluster can be detected is given by

$$V(M) = \int p(L|M)V(L)dL, \qquad (2)$$

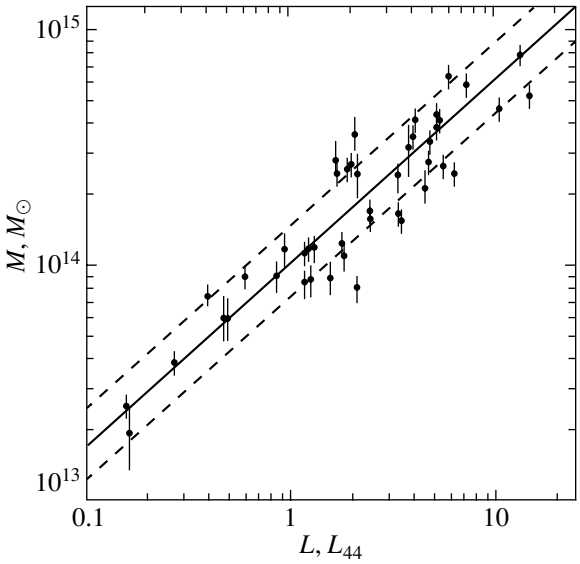

Fig. 1. Correlation between baryon mass M_{324} and cluster luminosity. The dashed lines indicate the characteristic (1σ) scatter.

where the function $p(L|M)$ defines the luminosity distribution for a cluster of a given mass M and $V(L)$ is the volume inside which a cluster of luminosity L produces an observed flux above the threshold value. The quantity $V(L)$ can easily be found from geometric calculations. Thus, the form of $p(L|M)$ must be determined. To determine it, let us analyze the relation between cluster luminosity and mass (see Fig. 1). The luminosities were measured in the energy range 0.5–2 keV within a circle of radius $7r_c$, where $r_c = 0.124(T/1\ \text{keV})^{1/2}$ Mpc (Vikhlinin *et al.* 1999). Since the luminosity outside the radius $7r_c$ typically accounts for no more than 3% of the luminosity inside this radius, the measured luminosities can be considered as the total ones. We see from Fig. 1 that the M–L relation can be fitted by a power function of the form $M = AL^\alpha$:

$$\log M[M_\odot] = 14.01 + (0.78 \pm 0.04)\log L[L_{44}]. \quad (3)$$

We see, however, that there is a significant scatter

Table 2. Correlation coefficients in the relation $\log M_{324}[M_\odot] = a + b\log T$ [keV]

Parameter	a	b
Gas	12.9	1.86 ± 0.10
Gas, symmetric clusters	13.0	1.80 ± 0.10
Gas + stars	13.1	1.75 ± 0.10
Gas + stars, symmetric clusters	13.1	1.69 ± 0.10

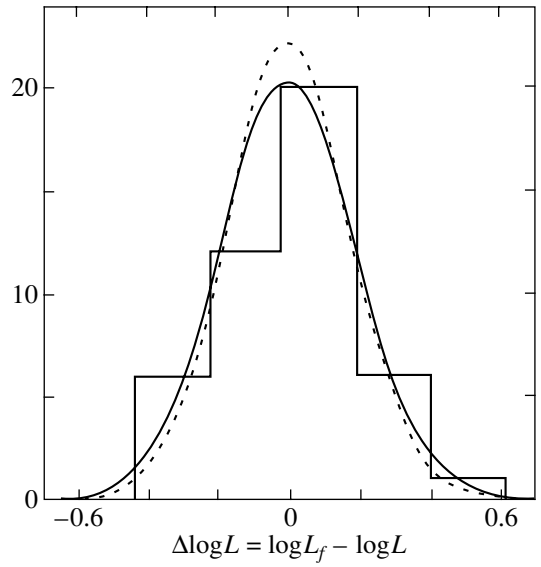

Fig. 2. A histogram of the deviations of the measured luminosity from the approximation formula (3). The solid line indicates a Gaussian fit to the histogram of deviations and the dotted line corresponds to a Gaussian with a dispersion from which the contribution from the mass measurement errors were subtracted.

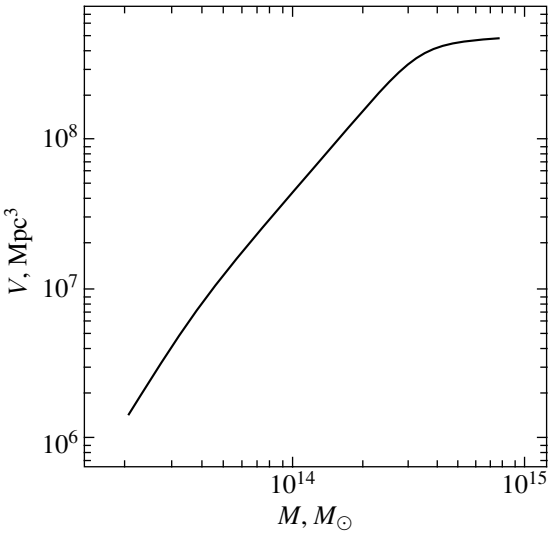

Fig. 3. The volume in which a cluster of a given mass can be detected.

of points about the mean relation. To determine the distribution function of deviations, we constructed a histogram of the logarithms of the deviations (see Fig. 2) of the measured luminosity from the mean relation (3). The histogram can be satisfactorily fitted by a Gaussian distribution with a zero mean and the variance $\sigma^2 = 0.036$. Below, the function $p(L|M)$ was assumed to be described by a logarithmic Gaussian distribution.

Apart from the true scatter, the derived variance includes the scatter due to the measurement errors of the cluster masses. Subtracting the well-known contribution of the measurement errors in quadrature yields the variance of the true scatter $\sigma^2 = 0.030$ (the dotted line in Fig. 2).

Thus, the volume in which a cluster can be detected is given by the formula

$$V(M) = \int_{-3\sigma}^{+3\sigma} p(x)V(L_f(M)10^{-x})dx, \quad (4)$$

where $L_f(M)$ is defined by formula (3) and $p(x)$ is the Gaussian distribution with a zero mean and the variance $\sigma^2 = 0.030$. Figure 3 shows the relation between volume and cluster mass derived in this way.

The Cumulative Mass Function

The cumulative mass function is defined as the number of clusters with masses larger than M per unit comoving volume. In practice, the cumulative mass function is estimated as $\sum_{M \geq M_i} 1/V_i$, where V_i is the volume for a cluster with a measured mass.

Figure 4 shows the derived cumulative mass function. Below, we will need various model fits to the derived mass function. A proper determination of these fits requires allowance for a number of nontrivial statistical effects. Let us demonstrate the complete procedure using the fit by the Schechter (1976) function as an example:

$$f(M) = A\left(\frac{M}{M_*}\right)^{\alpha} \exp\left(-\frac{M}{M_*}\right). \quad (5)$$

To calculate the parameters of the fit, we used the maximum-likelihood method. The likelihood function is (Cash 1979)

$$S(\boldsymbol{\theta}) = \sum_i \ln W(M_i, \sigma_{M_i}, \boldsymbol{\theta}) \quad (6)$$
$$- \int_0^{\infty} f(M, \boldsymbol{\theta})V(M)dM,$$

where the summation is performed over the clusters under study, $\boldsymbol{\theta}$ is the set of parameters to be determined, and $W(M_i, \sigma_{M_i}, \boldsymbol{\theta})$ is the probability density of observing a cluster in the range from M to $M + dM$. If the cluster mass were measured accurately, then the function W would be defined by the product $f(M, \boldsymbol{\theta})V(M)$. However, because of the measurements errors in the masses σ_{M_i}, the function W is given by the convolution

$$W(M_i, \sigma_{M_i}, \boldsymbol{\theta}) \quad (7)$$

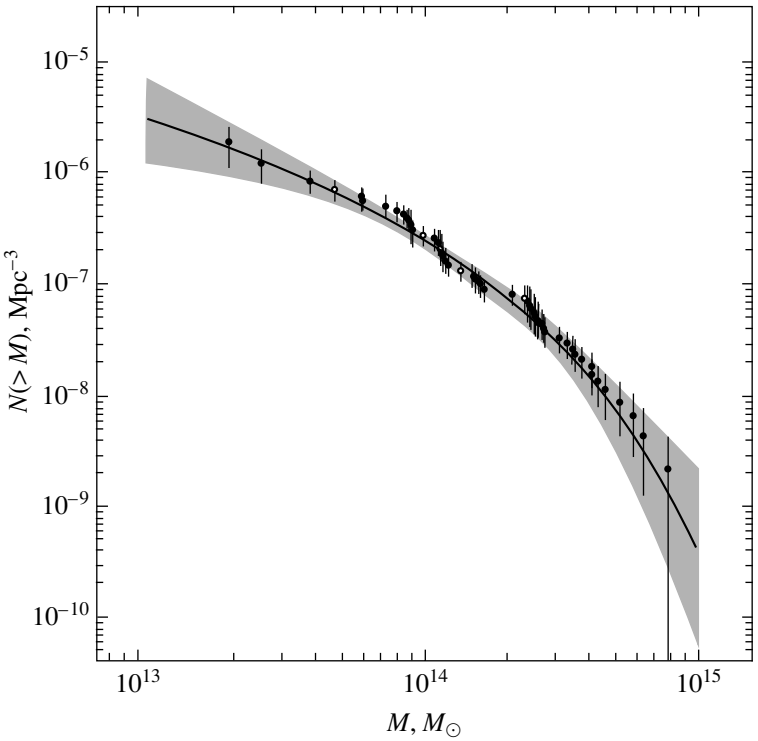

Fig. 4. The cumulative baryon mass function for the selected galaxy clusters. The open circles represent the clusters whose masses were determined from the $M-L$ correlation. The gray region corresponds to the set of Schechter functions with the parameters α and M_* belonging to the 68% confidence region shown in Fig. 5.

$$= \int_{M_i-2\sigma_{M_i}}^{M_i+2\sigma_{M_i}} f(M,\boldsymbol{\theta})V(M)p(M-M_i)dM,$$

where $p(x)$ is the Gaussian distribution with a zero mean and the variance $\sigma^2_{M_i}$.

Maximizing the function S yields the following parameters: $A = 1.2 \times 10^{-7}$ Mpc^{-3}, $\alpha = -1.71$, and $M_* = 2.53 \times 10^{14} M_\odot$. The Schechter function corresponding to these parameters is indicated by the solid line in Fig. 4.

Apart from the best-fit parameters, their uncertainties must also be known. The standard method of estimating the uncertainties in parameters (Cash 1979) involves finding the regions where the difference between the value of the likelihood function at some fixed parameter values and its maximum value does not exceed some fixed Δ. The values of Δ equal to 1.15 and 2.3 correspond to the 68 and 90% confidence regions of the parameters, respectively. Figure 5 shows the regions found in this way and the gray region in Fig. 4 corresponds to all the parameters of the fit admissible at the 68% confidence level.

DISCUSSION

Most of the studies aimed at determining cosmological parameters were carried out by using the cluster temperature function (see, e.g., Markevitch 1998; Henry 2000). Instead of the mass, its dependence on temperature is used in such studies, which introduces an additional uncertainty into the parameters estimated in this way. This uncertainty appears mainly

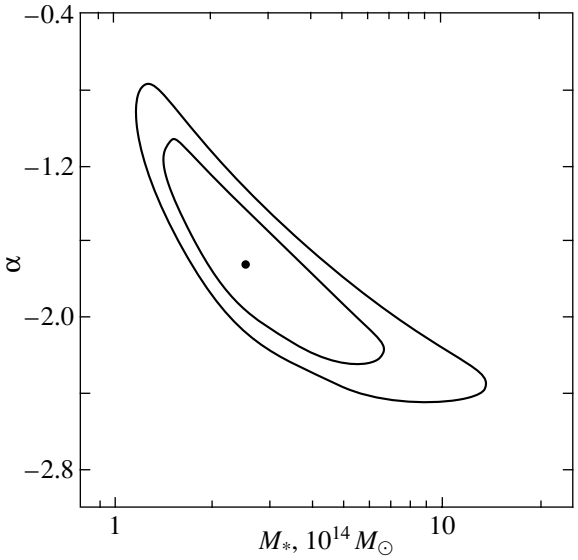

Fig. 5. The 68 and 90% confidence contours for α and M_* inferred by maximizing the likelihood function.

because the absolute calibration of the $M-T$ correlation is inaccurate, but also because of the significant scatter in this relation.

Here, we presented the measurement of the baryon mass function in clusters and described in detail the method of its modeling. Since the resulting baryon mass function was constructed on a statistically complete sample of galaxies, it can be used as follows. If the fraction of baryons in the total cluster mass, $f_{\rm bar}$, is assumed to be a universal quantity independent of their total mass, then the mass function derived here can be identified with a scaled total mass function of the clusters. Thus, it can be used to constrain the cosmological parameters.

ACKNOWLEDGMENTS

This work was supported by the Russian Foundation for Basic Research (project nos. 00-02-17124 and 02-02-06658) and the Commission of the Russian Academy of Sciences for Work with Youth.

REFERENCES

1. S. Allen, R. Schmidt, and A. Fabian, astro-ph/0205007.
2. S. Burles, K. Nollett, and M. Turner, Astrophys. J. **552**, 1 (2001).
3. W. Cash, Astrophys. J. **228**, 939 (1979).
4. A. Evrard, T. MacFarland, H. Couchman, *et al.*, Astrophys. J. **573**, 1 (2002).
5. A. Fabian, E. Hu, L. Cowie, and J. Grindlay, Astrophys. J. **248**, 47 (1981).
6. J. Henry, Astrophys. J. **534**, 565 (2000).
7. A. Jenkins, C. Frenk, S. White, *et al.*, Mon. Not. R. Astron. Soc. **321**, 372 (2001).
8. M. Markevitch, Astrophys. J. **50**, 27 (1998).
9. T. Reiprich and H. Bohringer, Astrophys. J. **567**, 716 (2002).
10. P. Schechter, Astrophys. J. **203**, 297 (1976).
11. A. Vikhlinin, W. Forman, and C. Jones, Astrophys. J. **525**, 47 (1999).
12. A. A. Voevodkin, A. A. Vikhlinin, and M. N. Pavlinsky, Pis'ma Astron. Zh. **28**, 417 (2002) [Astron. Lett. **28**, 366 (2002)].
13. S. White, J. Navarro, A. Evrard, and C. Frenk, Nature **366**, 429 (1993).

Translated by A. Dambis

Astronomy Letters, Vol. 28, No. 12, 2002, pp. 799–810. Translated from Pis'ma v Astronomicheskiĭ Zhurnal, Vol. 28, No. 12, 2002, pp. 889–901.

The X-ray Burst Detected in 1991 from the Transient Source SAX J1747.0−2853

S. A. Grebenev[1, 2, 3*], A. A. Lutovinov[1], M. N. Pavlinsky[1], and R. A. Sunyaev[1, 3]

[1] *Space Research Institute, Russian Academy of Sciences, Profsoyuznaya ul. 84/32, Moscow, 117810 Russia*

[2] *INTEGRAL Science Data Center, Versoix, Switzerland*

[3] *Max-Planck-Institut für Astrophysik, Karl Schwarzschild Strasse 1, Garching bei München, 86740 Germany*

Received June 25, 2001; in final form, February 14, 2002

Abstract—We present the observations of an intense X-ray burst from the recurrent transient source SAX J1747.0−2853 located near the Galactic center. The burst was detected by the ART-P telescope onboard the Granat observatory on October 20, 1991. The burst time profile exhibits features that clearly point to an increase in the photospheric radius of the neutron star at the burst onset. This increase is attributable to an expansion of its outer hydrogen-rich atmospheric envelope under radiation pressure. After hydrogen-envelope outflow and photospheric contraction, the radiation flux emerging from deep within the star continued to rise, which several seconds later led to a recurrent, weaker photospheric expansion attributable to the outflow of the outer helium-envelope layers. Based on the described picture, we determined the distance to the source, $d = 7.9 \pm 0.4$ kpc. No radiation was detected by the ART-P telescope from the source in quiescence. Actually, the source itself was discovered only seven years later by the BeppoSAX satellite during its X-ray activity. © *2002 MAIK "Nauka/Interperiodica"*.

Key words: *neutron stars, X-ray sources, X-ray bursts, photospheric expansion, comptonization.*

INTRODUCTION

The source SAX J1747.0−2853 was discovered by the Wide-Field Camera (WFC) onboard the BeppoSAX satellite during its outburst late in March 1998 (in't Zand *et al.* 1998). The pointing of the main (NFI) BeppoSAX X-ray telescopes one day after its discovery allowed the source to be localized with an accuracy of $\lesssim 1'$ (R.A. $= 17^{\rm h}47^{\rm m}02^{\rm s}$, Decl. $= -28°52'.5$, epoch 2000.0) and showed it to have a hard power-law spectrum extending to 150–200 keV (Bazzano *et al.* 1998; Natalucci *et al.* 2000). The spectrum was characterized by a photon index $\alpha \simeq 2.4$; an additional thermal component (with a blackbody temperature $kT_{bb} \simeq 0.6$ keV) distorted by strong ($N_{\rm H} \simeq 7 \times 10^{22}$ cm^{-2}) interstellar absorption appeared in the spectrum at low energies. The 2–28-keV flux from the source reached a maximum, ∼15 mCrab, on March 23, 1998, and subsequently began to slowly decrease. The observations on April 13–15 (Sidoli *et al.* 1998) showed that the flux decreased by a factor of ∼10 in three weeks; i.e., the exponential decay time was ∼8 days.

A recurrent, stronger outburst of the source was detected by the RXTE (Markwardt *et al.* 2000), BeppoSAX (Campana *et al.* 2000), and ASCA (Murakami *et al.* 2000) satellites in the first half of March 2000. The X-ray flux during this outburst was, on average, ∼40 mCrab and reached 140 mCrab at its brightness maximum (March 7). Additional weaker outbursts were observed during several ensuing months (in't Zand 2001). This behavior suggests that SAX J1747.0−2853 belongs to the group of recurrent X-ray transients. Curiously, the source position in the sky coincides, within the measurement errors, with the position of the X-ray transient GC X−3. The latter was discovered on April 21, 1976, during the flight of a rocket launched at the Goddard Space Flight Center (Cruddace *et al.* 1978) and was subsequently observed on June 17, 1976, in a Birmingham University rocket experiment. Three months later, the RMC instrument with a rotating modulation collimator onboard the Ariel 5 satellite discovered the source GX + 0.2, −0.2 in this region (Proctor *et al.* 1978). Although this region is densely populated (located at ∼19′ from the Galactic center), it can probably be assumed that the same recurrent source was observed in all of the above cases.

The recent Chandra observation on July 18, 2001, revealed the source in a state with an extremely weak radiation flux, ∼0.6 mCrab, which corresponds to a luminosity of $\sim 2.5 \times 10^{35}$ erg s^{-1} in the energy range 0.5–10 keV at a distance of 8 kpc (Wijnands

*E-mail: sergei@hea.iki.rssi.ru

1063-7737/02/2812-0799$22.00

et al. 2002). The source spectrum was even harder, $\alpha \simeq 1.8$, than that observed during its bright state. This result indicates that the source is distinguished by complex temporal behavior and can remain active even between outbursts during its off state.

Fourteen type-I X-ray bursts were detected from the source during its outburst in the spring of 1998; at least two more bursts were detected in March 2000. This strongly suggests that the compact object in SAX J1747.0–2853 is a weakly magnetized neutron star. The time profile of one of the bursts exhibits features that point to an expansion of the neutron-star photosphere at the burst onset. Here, we present the observations of such a burst from this source with an even higher intensity and even clearer evidence of photospheric expansion. This burst was detected by the ART-P telescope onboard the Granat observatory on October 20, 1991. It should be immediately noted that the ART-P telescope detected no radiation from SAX J1747.0–2853 in quiescence.

OBSERVATIONS

The ART-P telescope onboard the Granat orbiting astrophysical observatory consisted of four independent modules. Each module was a position-sensitive detector with a geometric area of 625 cm^2 equipped with a collimator and a coded mask whose opaque elements always covered half of the detector. The instrument had a $3.^\circ4 \times 3.^\circ6$ field of view (beam FWHM) and an angular resolution of $5'$ (the coded-mask element size). Because of the higher spatial resolution of the detector ($\sim$1.25 arcmin), the localization accuracy for bright discrete sources was several times higher. The telescope was sensitive to photons in the energy range 2.5–60 keV (the photon arrival time was accurate to within $\sim$3.9 μs; the ART-P dead time was 580 μs) and had an energy resolution of $\sim$22% in the 5.9-keV iron line. Unfortunately, the observation during which the X-ray burst was detected from SAX J1747.0–2853 was carried out by the ART-P module with a reduced sensitivity at energies $h\nu \leq 6$ keV because of voltage problems on one of the anode grids (see Grebenev *et al.* 2002). For this reason, we were unable to perform a comprehensive spectral analysis of the source radiation. For a more detailed description of the telescope, see Sunyaev *et al.* (1990).

During 2.5 years of the ART-P in-orbit operation (1990–1992), the telescope was regularly pointed at the Galactic-center region. The total exposure time exceeded 8.3×10^5 s; several tens of X-ray bursts were detected from various sources (Grebenev *et al.* 2000, 2002; Lutovinov *et al.* 2001). The burst observed on October 20, 1991, was identified with SAX J1747.0–2853. The two lower panels in Fig. 1 show the light curve obtained during October 19.41–20.33 (UT) in the energy range 3–26 keV. The regular $\sim$30-s-long breaks in the light curve result from the telescope-accumulated data transmission to onboard memory. We clearly see 12 X-ray bursts of different intensities. Even if we take into account the fact that this was one of the longest ART-P observing sessions, which lasted almost one day (the pure exposure time minus the above breaks in information flow was 72 600 s), the number of detected bursts appreciably exceeded their usual number. For comparison, the upper panel shows the light curve obtained in the preceding session of October 18.46–18.85 (UT), during which only two bursts were detected over 25 500 s of observations. Because of the low sensitivity of the ART-P module used at the soft energies noted above, we failed to localize most of the bursts detected on these days. The strongest burst observed $\sim$52 350 s after the beginning of the October 19–20 session (the flux was at a maximum on October 20 at $00^h26^m42^s$ UT) was an exception.

LOCALIZATION AND RADIATION FLUXES

Figure 2 (left panel) shows the image of the sky within the ART-P field of view (S/N-ratio map) accumulated during the entire session of October 19–20. X-ray emission was detected at a statistically significant level from three sources: A 1742–294, 1E 1740.7–2942, and SLX 1744–299/300. The latter is actually the pair SLX 1744–299 and SLX 1744–300 spaced $2.'5$ apart; they are very difficult to resolve with the ART-P telescope (see Pavlinsky *et al.* 1994). Yet another usually bright source, 1E 1743.1–2843, was detected near the edge of the field of view at 3.7σ confidence. Almost all of the above sources (except 1E 1740.7–2942) are X-ray bursters. There are also several other well-known bursters within the field of view (e.g., SLX 1732–304 in the globular cluster Terzan 1), from which no persistent emission was detected during the session under consideration. However, they could potentially be the burst sources.

The right panel in Fig. 2 shows the ART-P image of the same field obtained only in the burst time (25 s). None of the above persistent sources were detected at a signal-to-noise ratio S/N $\geq 2.7\sigma$ in such a short time. The image exhibits only one source detected at 5.6σ confidence. It lies at the point with coordinates R.A. $= 17^h43^m48.^s51$, Decl. $= -28^\circ50^m59.^s33$ (epoch 1950.0),[1] which coincides with the position

[1] R.A. $= 17^h46^m59.^s05$, Decl. $= -28^\circ52^m03.^s17$ (epoch 2000.0).

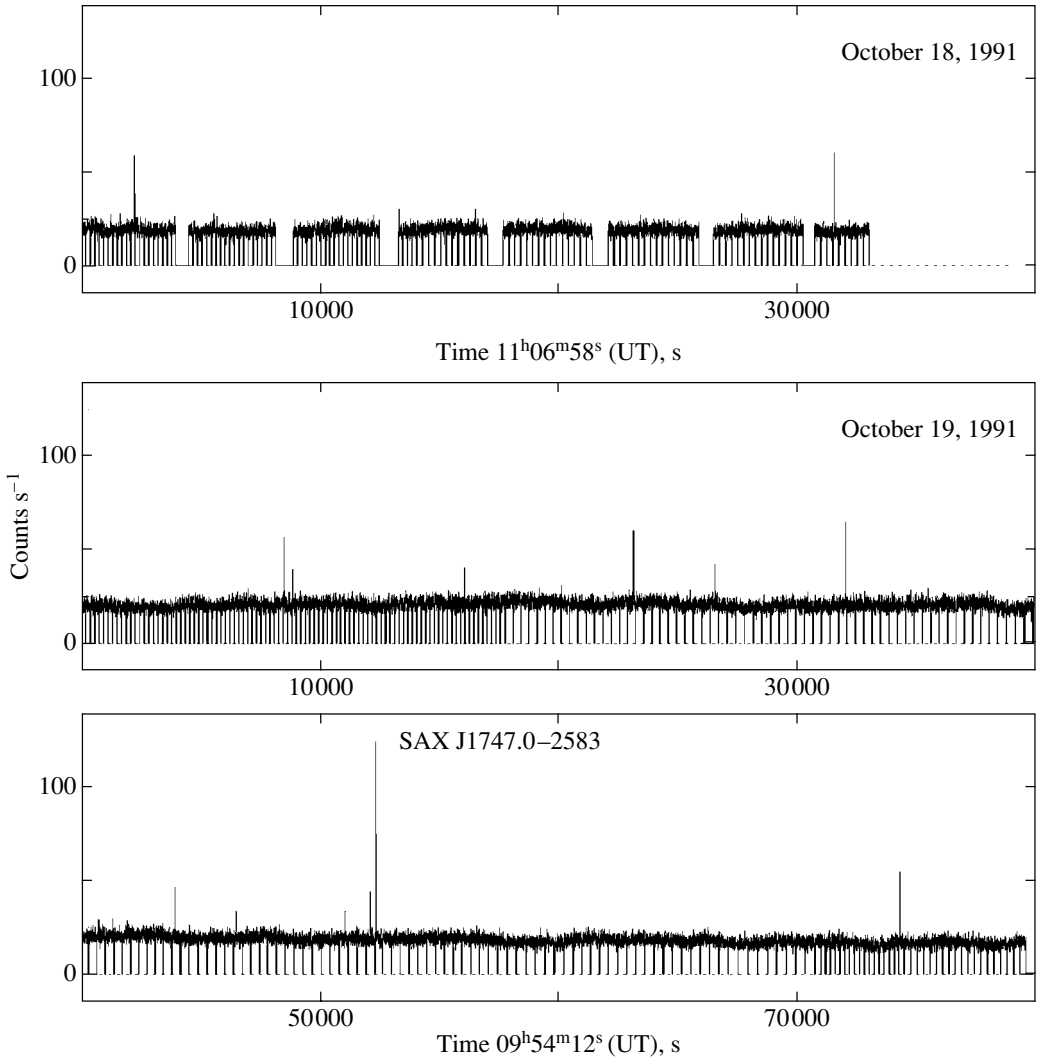

Fig. 1. The ART-P 3–26 keV light curves obtained during the observations of the Galactic-center region on October 18 (upper panel) and 19–20 (lower panels), 1991. The time resolution was 4 s; the time from the session beginning is along the horizontal axis. The intense X-ray burst was identified with SAX J1747.0–2853. Some of the bursts observed during the second session may also be associated with the activity of this source, because their number appreciably exceeds the usual number of bursts detected from this region (see the upper panel).

of the X-ray transient SAX J1747.0–2853 to within 47″ (Bazzano *et al.* 1998). A magnified image of the region near the source is shown in Fig. 3. The positions of the X-ray transients SAX J1747.0–2853 (A), GX + 0.2, −0.2 (B), and GC X-3 (C) mentioned in the Introduction as well as of the sources 1E 1743.1–2852 (D) and 1E 1743.4–2852 (E) detected by the EINSTEIN observatory (Watson *et al.* 1981) are marked in this figure. The last source is most likely the nearby F0 star SAO 185730 rather than an X-ray binary. Since the contours in this figure are shown at the signal-to-noise ratios S/N = 1.6, 2.6, 3.6, 4.6, and 5.6σ (measured from the peak top at 1σ steps), the radius of the error circle for the source position can be easily estimated, $\simeq 4'.2$. This is the statistical error at a 1σ confidence level; the systematic error is much smaller than this value ($\simeq 45''$).

Note that the confidence level of the burst detection in the light curve, $\sim 50\sigma$, appreciably exceeds 5.6σ obtained in image analysis. This is because the efficiency and, in particular, the spatial resolution of the detector degrade at low energies (as mentioned above). In constructing the light curve shown in Fig. 1, we summed all the photons detected in the energy range 3–26 keV, irrespective of their spatial coordinate. Therefore, the degradation of the detector spatial resolution was of no importance.

The photon fluxes in the energy ranges 4–10, 10–18, and 18–26 keV and the 4–26-keV luminosities estimated by analyzing the images for the

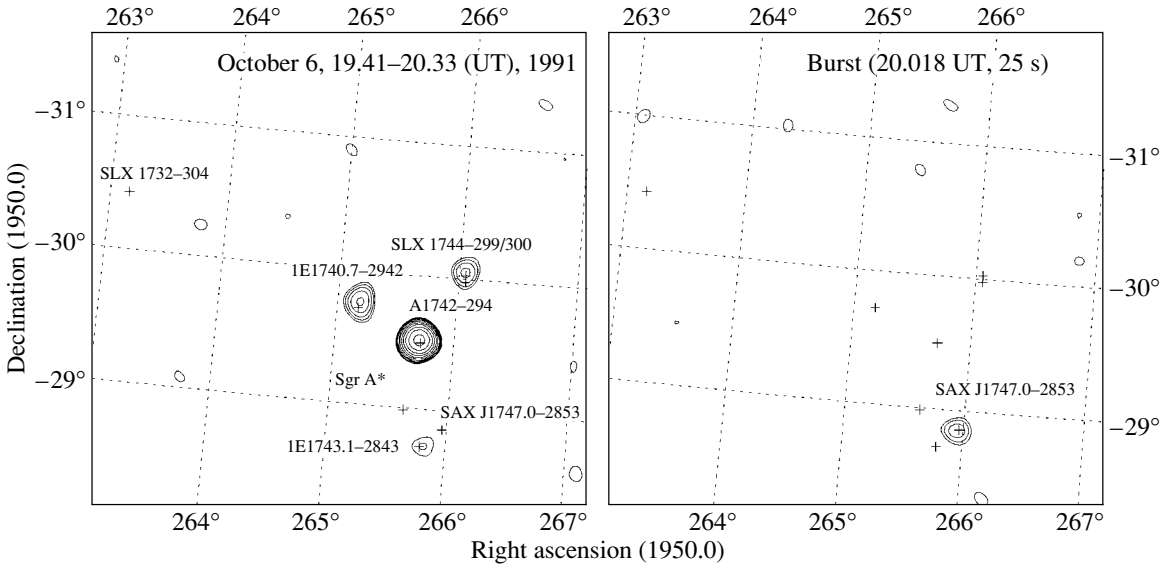

Fig. 2. The 4–26-keV images of the sky region within the ART-P field of view obtained during the entire observing session of October 19–20, 1991, except 25 s during which a strong X-ray burst was observed (left panel) and during the burst (right panel). The error regions of the sources at 2.7, 3.5, 4.6, 5.9, 7.7, or more σ confidence levels (given at logarithmic steps) are indicated by contours.

sources detected within the ART-P field of view are given in Table 1. It lists the fluxes and luminosities for SAX J1747.0–2853, as measured during the burst (the values averaged over 25 s); for the source radiation in quiescence, the table gives the corresponding 3σ upper limits. The fluxes were corrected for the contribution of Galactic diffuse radiation determined from the same image. In estimating the luminosity, we assumed all sources to be located near the Galactic center at a distance of 8 kpc.

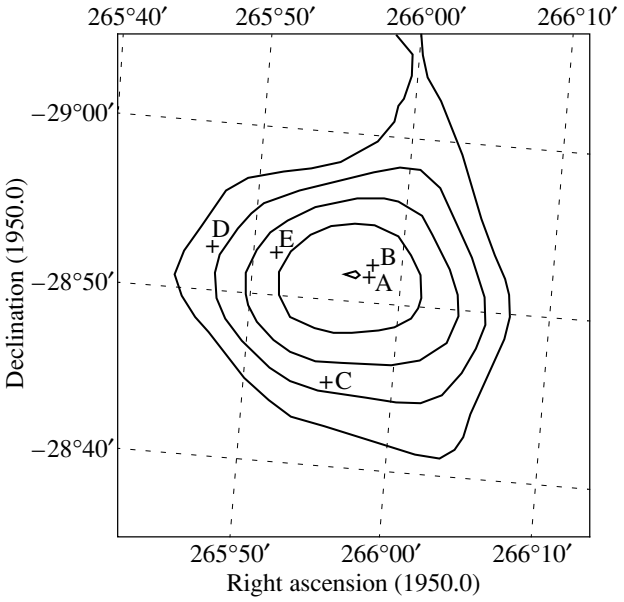

Fig. 3. A magnified ART-P 4–26-keV image of the sky region near SAX J1747.0–2853 during the burst detected on October 20 at $00^h26^m42^s$ UT. The error regions of the burst source at 1.6, 2.6, 3.6, 4.6, and 5.6σ confidence levels (measured from the peak top at 1σ steps) are indicated by contours. The position of SAX J1747.0–2853 is marked by the letter A; the positions of the other known sources in this region are marked by the letters B, C, D, and E (see the text).

The table also provides information on the observation efficiency for each source in a given session corrected for finite collimator transmission. The low confidence level at which the source 1E 1743.1–2843 was detected is attributable precisely to the low efficiency of its observation (it lies at the edge of the field of view). The actual flux from this source was comparable to the measured flux from 1E 1740.7–2942 and appreciably exceeded the flux from SLX 1744–299/300. The observation efficiency for SAX J1747.0–2853 was higher. During the session, the ART-P axis could deviate from the pointing position within 30 arcmin, because the satellite orientation (rotation) changed, and the observation efficiency for the source smoothly varied on a time scale of the order of 1000 s. This was the reason why the observation efficiency for SAX J1747.0–2853 during the burst differed by $\sim$20% from its session-averaged efficiency.

The photon fluxes from the bright sources listed in Table 1 were typical of the fall of 1991 (Pavlinsky *et al.* 1992, 1994). The radiation from all these sources (in particular, 1E 1740.7–2942 and SLX 1744–299/300) was hard. We mentioned above that SAX J1747.0–2853 during its 1998 outburst also had a hard power-law ($\alpha \simeq 2.4$) photon spectrum.

Table 1. Radiation fluxes and luminosities of the sources detected by the ART-P telescope in the field of view during the observation of October 19–20, 1991[a]

Source	Photon flux, mCrab			Luminosity,[b] 10^{36} erg s^{-1}	ξ [c]
	4–10 keV	10–18 keV	18–26 keV		
A 1742–294	51.8 ± 3.9	50.3 ± 2.2	30.2 ± 4.6	8.46 ± 0.33	65
1E 1740.7–2942	15.3 ± 4.1	18.8 ± 2.3	19.0 ± 4.9	3.28 ± 0.35	59
SLX 1744–299/300	≤ 6.0[d]	7.1 ± 1.3	8.5 ± 2.8	0.98 ± 0.20	73
1E 1743.1–2843	13.2 ± 6.1	14.2 ± 3.5	9.2 ± 7.4	2.35 ± 0.52	27
SAX J1747.0–2853	≤ 12.6[d]	≤ 7.2[d]	≤ 15.3[d]	≤ 1.08[d]	35
Burst from image	499 ± 419	1138 ± 224	586 ± 309	158 ± 31	43
from light curve	1030 ± 57	1139 ± 48	602 ± 83	186 ± 6	43

[a] Uncorrected for interstellar absorption.

[b] The 4–26-keV luminosity for the assumed distance of 8 kpc.

[c] The collimator transmission efficiency in percent.

[d] The 3σ upper level.

RADIATION DURING THE BURST

Figure 4 shows the time profiles of the X-ray burst detected by the ART-P telescope on October 20, 1991, in the energy ranges 4–26, 4–10, and 10–26 keV with a 1-s resolution. Time "0" on the horizontal axis corresponds to the time when the radiation flux reached a maximum ($00^h26^m42^s$ UT); the time taken as the burst onset is marked by an arrow. Although this event undoubtedly belongs to type-I bursts produced by the thermonuclear explosion of a mixture of hydrogen and helium on the neutron-star surface, the derived time profiles differ greatly from the canonical profiles of type-I bursts with a sharp rise and a subsequent slow exponential decay of the X-ray flux (Lewin 1993). In the soft energy range, the profile of this burst was a broad, almost symmetric pulse of radiation. In the hard energy range, a second pulse that preceded the first pulse in time, a precursor peak, appeared in the burst profile.

Such a behavior points to a photospheric expansion of the neutron star at the early ($t \lesssim 10$ s) burst stage [see Lewin *et al.* (1993) for an overview of the observational manifestations of bursts with photospheric expansion]. The photospheric expansion is attributable to the expansion and subsequent outflow of the outer hydrogen-rich atmospheric layers in the neutron star under radiation pressure (Ebisuzaki *et al.* 1983). For such an expansion to take place, an energy that is enough to produce a near-Eddington emergent flux must be released during the explosion,

$$F_{\rm ed} = \frac{GM_* m_p \mu_{\rm e}}{R_*^2} \frac{c}{\sigma_{\rm T}}. \qquad (1)$$

Here, M_* is the mass of the neutron star, R_* is its radius, $\sigma_{\rm T}$ is the Thomson cross section for photon scattering by electrons, and $\mu_{\rm e}$ is the number of nucleons per electron. In the outer hydrogen-rich envelope with a normal cosmic helium abundance (6.7%

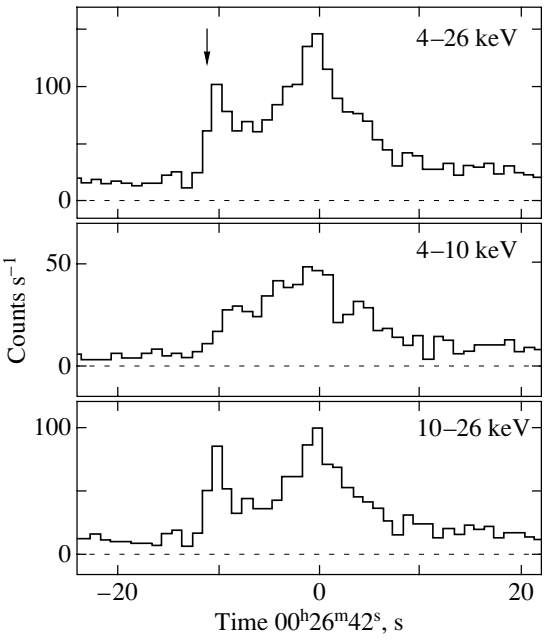

Fig. 4. Time profiles of the X-ray burst detected by the ART-P telescope from SAX J1747.0–2853 on October 20 at $00^h26^m42^s$ UT in the energy ranges 4–26, 4–10, and 10–26 keV. The double-peaked structure of the profile in the hard energy range is attributable to a decrease in the temperature of the neutron-star photosphere during its expansion. The arrow marks the burst onset.

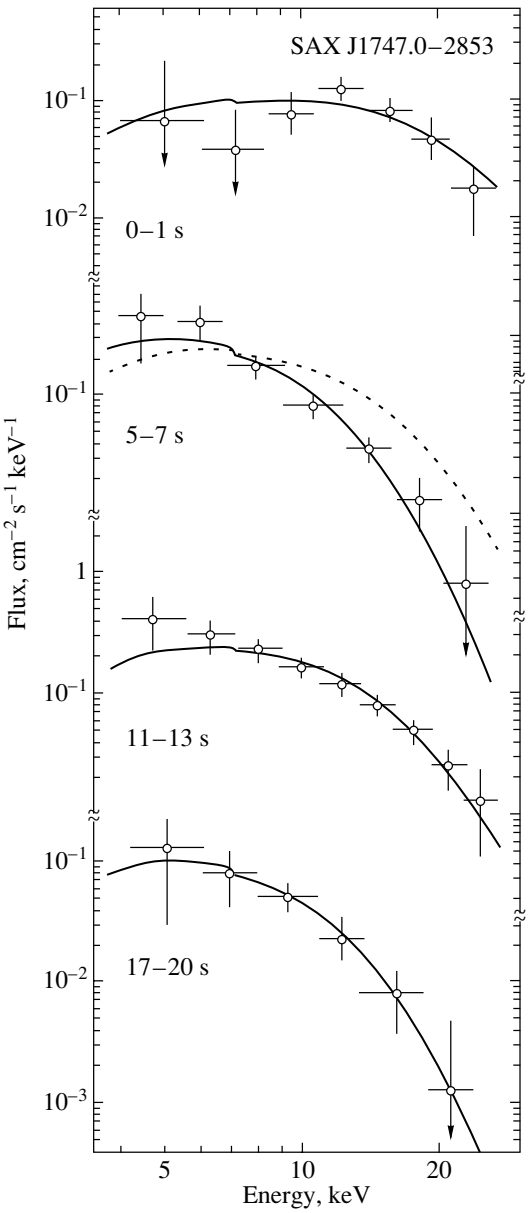

Fig. 5. Spectral evolution of the X-ray burst detected from SAX J1747.0–2853 by the ART-P telescope on October 20, 1991. The errors correspond to one standard deviation. The numbers indicate the measurement times of the spectra, in seconds from the burst onset. The solid lines represent their blackbody fits; the dashed line represents the fit to the spectrum measured immediately after the burst maximum (11–13 s after the burst onset). The blackbody temperature kT_{bb} of the spectra is 4.7, 2.0, 3.1, and 2.4 keV. The cooling of the neutron-star photosphere shortly after the burst onset is indicative of its expansion under radiation pressure.

of hydrogen by the number of atoms) $\mu_e \simeq 1.12$; accordingly,

$$F_{ed}(H) \simeq 1.6 \times 10^{25} \left(\frac{M_*}{1.4M_\odot}\right) \times \left(\frac{R_*}{10\ \mathrm{km}}\right)^{-2} \mathrm{erg\ s^{-1}cm^{-2}}. \quad (2)$$

In deeper layers, the radiation pressure plays a lesser role and the atmosphere with radiation fluxes comparable to $F_{ed}(H)$ remains stationary here. This is because, first, $\mu_e \simeq 2$ and $F_{ed}(He) \simeq 1.9F_{ed}(H)$ due to helium enrichment during slow hydrogen burning and, second, the cross section for photon scattering by electrons σ_{es} appreciably decreases compared to σ_T due to the higher temperature in these layers. The helium shell can become nonstationary when the flux $F \gtrsim F_{ed}(He)$ emerging from deep within the star increases further (Paczynski 1983; Paczynski and Anderson 1986). Below, we will see that the burst under discussion developed according to this scenario.

The expansion and subsequent contraction (the decrease in radius R_{ph}) of the photosphere took place at constant luminosity $L \simeq L_{ed}(H) = 4\pi R_*^2 F_{ed}(H) \simeq 1.8 \times 10^{38}(M/1.4M_\odot)$ erg s^{-1} and were accompanied first by its rapid cooling and then by its reheating. The radiation flux emerging from the photosphere $F = \sigma T_{eff}^4 = L/4\pi R_{ph}^2$, where σ is the Stefan–Boltzmann constant, and, accordingly, the effective radiation temperature decreased during the expansion as $T_{eff} \sim R_{ph}^{-1/2}$. The dip in the burst profile and the appearance of a double-peaked structure at high energies are attributable precisely to the drop in radiation temperature within several seconds after the explosion and to the reduction in the number of hard photons.

The described picture is confirmed by the four photon spectra measured at different burst stages (see Fig. 5): during the precursor peak, in the interval between the two peaks, at the main peak, and at the burst decay stage. We see that the hard (with a color temperature $kT_{bb} \simeq 4.7$ keV) radiation spectrum measured in the first second after the burst onset becomes soft ($kT_{bb} \simeq 2.0$ keV) ~5 s later and then again becomes hard ($kT_{bb} \simeq 3.1$ keV) near the flux maximum. The radiation temperature measured at the burst decay stage, $kT_{bb} \simeq 2.4$ keV, is lower than the radiation temperature at the main peak; this is the so-called radiation cooling effect characteristic of the exponential stage of type-I bursts (Lewin *et al.* 1993). Radiation cooling is also suggested by the decrease (which is clearly seen in Fig. 4) in the characteristic flux decay time in the burst profile when passing from low energies ($t_{exp} = 4.97 \pm 0.50$ s in the range 4–10 keV) to higher energies ($t_{exp} = 4.42 \pm 0.36$ s in the range 10–26 keV).

The accumulation time of the spectra shown in Fig. 5 is 1–3 s. A statistically significant photon spectrum cannot be obtained in such a short time based on image analysis (the total confidence level

Table 2. Evolution of the spectral radiation parameters for the X-ray burst detected from SAX J1747.0−2853 on October 20, 1991.

Time,[a] s	Flux,[b] mCrab	Flux,[c] 10^{-8} erg cm^{-2} s^{-1}	kT_{bb}, keV	R_{bb},[d] km	χ^2_N [e]
0−1	1510 ± 200	3.42 ± 0.47	4.69 ± 0.60	2.19 ± 0.46	0.84
1−3	1100 ± 120	2.46 ± 0.27	2.65 ± 0.27	5.58 ± 1.33	1.29
3−5	980 ± 115	2.21 ± 0.26	2.05 ± 0.21	9.34 ± 2.46	1.20
5−7	970 ± 120	2.19 ± 0.27	2.00 ± 0.23	10.35 ± 2.95	0.81
7−9	1510 ± 140	3.39 ± 0.31	2.54 ± 0.22	7.28 ± 1.46	0.89
9−11	2480 ± 165	5.49 ± 0.37	2.67 ± 0.15	8.20 ± 1.07	1.74
11−13	1840 ± 150	4.14 ± 0.33	3.06 ± 0.25	5.34 ± 0.98	0.61
13−15	1290 ± 130	2.89 ± 0.29	2.87 ± 0.26	5.06 ± 1.01	0.93
15−17	930 ± 120	2.01 ± 0.26	2.52 ± 0.26	5.48 ± 1.31	1.03
17−20	380 ± 70	0.81 ± 0.16	2.38 ± 0.37	4.00 ± 1.52	1.18
20−23	280 ± 70	0.63 ± 0.15	2.85 ± 0.70	2.25 ± 1.22	0.64

[a] The time from the burst onset $00^h26^m31^s$ (UT).

[b] The 4−26-keV photon flux uncorrected for interstellar absorption.

[c] The 4−26-keV radiation flux uncorrected for absorption.

[d] For the assumed distance of 8 kpc.

[e] The χ^2 value normalized to the number of degrees of freedom.

of the burst in the image was only 5.6σ over a wide energy range). Therefore, we used the detector count rates in narrow spectral channels to reconstruct the spectra. The background count rate in each channel was defined as the mean rate measured within ~300 s immediately before the burst and within ~300 s after the burst. Apart from the instrumental and diffuse backgrounds, it included the background related to the steady-state radiation from compact sources in the field. Therefore, the spectra presented in the figure refer only to the burst proper. They contain no contribution of X-ray radiation from the source produced by accretion. We disregarded the possible variability in the background due to a partial eclipse of the region of energy release responsible for the persistent emission of the source by the expanding opaque photosphere (such an eclipse was observed by the RXTE satellite during a strong X-ray burst in 4U 1724−307 in the globular cluster Terzan 2; see Molkov *et al.* 2000). Table 1 contains the 25-s-averaged burst flux in various energy ranges estimated in this way. This estimate is in good agreement with the estimate obtained through image analysis but it has a much smaller statistical uncertainty.

The color temperature kT_{bb}, which characterizes the hardness of the measured spectra, was determined above by assuming that the spectra were Planckian in shape:

$$F_\nu^{bb} = \pi B_\nu(T_{bb}) \left(\frac{R_{bb}}{d}\right)^2, \quad (3)$$

where

$$B_\nu(T_{bb}) = \frac{2h\nu^3}{c^2}\left[\exp\left(\frac{h\nu}{kT_{bb}}\right) - 1\right]^{-1}.$$

If a local thermodynamic equilibrium were maintained in the neutron-star photosphere and if it actually radiated as a blackbody, then the derived color temperature would be equal to the effective radiation temperature and the bolometric luminosity of the photosphere would be $L_B = 4\pi R_{bb}^2 \sigma T_{bb}^4$. In this case, Eq. (3) could be rewritten as

$$F_\nu^{bb} = \left(\frac{L_B}{d^2 \sigma T_{bb}^4}\right)\frac{h\nu^3}{2c^2}\left[\exp\left(\frac{h\nu}{kT_{bb}}\right) - 1\right]^{-1}. \quad (4)$$

At low energies, the observed source spectra are distorted by interstellar absorption with a hydrogen column density $N_H \simeq 7 \times 10^{22}$ cm^{-2} for standard heavy-element abundances (Bazzano *et al.* 1998; Wijnands *et al.* 2002). Below, we assume N_H to be fixed. The model spectra for the derived parameters are indicated in Fig. 5 by solid lines. To trace the spectral evolution in more detail, we separated out

eleven consecutive time intervals (one is 1 s long, eight are 2 s long, and the last two are 3 s long) in the burst profile. For each of them, the spectrum was constructed in accordance with the procedure described above and fitted by a blackbody model. The fitting results are presented in Table 2. Apart from the photospheric parameters and the χ^2_N value, which characterizes the quality of the fit, this table gives estimates of the photon flux (in mCrab) and the radiation flux (in erg cm^{-2} s^{-1}) in the energy range 4–26 keV for each time interval. At burst maximum, the flux from the source reached ~2.5 Crab. Note that the blackbody model unsatisfactorily describes the spectrum measured at burst maximum ($\chi^2_N \simeq 1.74$).

The temperature kT_{bb}, radius R_{bb}, and bolometric luminosity L_B of the neutron-star photosphere are plotted against time in Fig. 6. In estimating R_{bb} and L_B, we assumed the distance to the source to be 8 kpc, as above. The dotted lines indicate two Eddington luminosities for a $M = 1.4M_\odot$ neutron star under the assumption of hydrogen-rich and purely helium atmospheres. We see that during the photospheric expansion, the bolometric luminosity was actually approximately constant and close to the Eddington luminosity $L_{ed}(H) \simeq 1.8 \times 10^{38}$ erg s^{-1}. For a convenient comparison, the lower panel shows the evolution of the X-ray luminosity derived from direct measurements in the energy range 4–26 keV. At temperatures $kT_{bb} \sim 2$–4 keV, the luminosity in this range accounts for 80–95% of the bolometric luminosity. The luminosity difference was largest precisely during the hydrogen-envelope outflow (points 3, 4, and 5 in the two lower panels of the figure).

In general, the figure confirms that the neutron-star photosphere actually expanded at the initial burst stage. During this expansion, its radius increased at least by a factor of 5, while its temperature decreased by more than a factor of 2.

DISCUSSION

The X-ray burst detected by the ART-P telescope from the transient source SAX J1747.0–2853 undoubtedly belongs among interesting and, in some respects, even unique events. Besides, the history of its discovery is instructive. Only the degradation of the spatial resolution of the ART-P detector, because of which the burst localization reliability proved to be not as high as it could be (only 5.6σ), and the absence of a persistent source at the localization position, despite the long duration of the observations ($\sim 8 \times 10^5$ s), did not allow us to claim the discovery of a new X-ray source, GRS 1744–285 (GRS—"Granat" Source), long ($\gtrsim$6.5 years) before its discovery by the BeppoSAX satellite. The burst detection raised the question of whether a population of ultraweak X-ray bursters with fluxes much lower than 1 mCrab could exist near the Galactic center. Such bursters manifest themselves and, thus, give the chance to detect them only during bursts.

The double-peaked structure of the burst points to the expansion and subsequent contraction of the neutron-star photosphere shortly after its onset. The rise in luminosity that continued after the contraction suggests that the outflow of the outer hydrogen-rich envelope under radiation pressure took place during this period. The envelope was either completely ejected or expanded to an extent that it became transparent. The observed photospheric contraction is very difficult to explain in a different way. A hydrogen envelope must inevitably be formed in the stellar atmosphere during the accretion of matter with normal elemental abundances, because hydrogen burns into helium at a large depth. The helium-envelope outflow could begin and, as we show below, began only during the further rise in luminosity because of the factor of 2 smaller opacity than that for hydrogen, $\kappa_{es}(He) = \sigma_{es}/2m_p$. This process affected only the outer, cooler layers of the helium envelope, where the opacity is larger than that deep in the envelope. Since the explosion energy is not enough to eject the entire helium envelope, in this case (in contrast to the hydrogen-envelope ejection stage) the subsidence of the photosphere was attributable to the started decrease in the radiation flux coming from deep within the star. In general, the described picture accounts for the observed profile and the spectral evolution of the burst in SAX J1747.0–2853. However, several points need to be explained.

Comptonization, Radius, and Luminosity of the Photosphere

Even if we take into account expansion, the photospheric radius R_{bb} is smaller than the typical neutron-star radius $R_* \simeq 10$–15 km. One of the causes could be an oversimplified approach to describing the spectra by a blackbody model. As was shown by London *et al.* (1984), Sunyaev and Titarchuk (1986), Ebisuzaki and Nomoto (1986), and Babul and Paczynski (1987), because of Comptonization, the spectra of the radiation emerging from the photospheres of X-ray bursters during bursts could differ greatly from Planckian spectra. In particular, in the X-ray range, these spectra are dominated by the Wien radiation component whose temperature corresponds to the electron temperature of the outer photospheric layers $T_e \simeq T_{bb}$ and appreciably exceeds the effective temperature $T_{eff} = (F/\sigma)^{1/4}$. In this

case, the observed X-ray spectrum uncorrected for interstellar absorption must be

$$F_\nu^w \simeq \pi\left(\frac{R_{\rm ph}}{d}\right)^2\left(\frac{T_{\rm eff}}{T_{\rm e}}\right)^4\frac{2h\nu^3}{c^2}\exp\left(-\frac{h\nu}{kT_{\rm e}}\right) \quad (5)$$
$$=\left(\frac{L_{\rm B}}{d^2\sigma T_{\rm e}^4}\right)\frac{h\nu^3}{2c^2}\exp\left(-\frac{h\nu}{kT_{\rm e}}\right).$$

In contrast to formula (3), formula (5) does not allow the photospheric radius of the neutron star to be determined until the dependence of $T_{\rm e}$ on $T_{\rm eff}$ is known. At the same time, the expression on its right-hand side makes it possible to estimate the bolometric luminosity of the photosphere $L_{\rm B}$. Note that this expression is similar to formula (4). This similarity suggests that the validity range of formula (4) is broader than the expected one and confirms that the results of our $L_{\rm B}$ measurements presented in Fig. 6 are correct. The temperature estimates shown in this figure are also valid only if the temperature of the outer photospheric layers $T_{\rm e}$, rather than the effective radiation temperature, is meant by T_{bb}.

The dependence of $T_{\rm e}$ on $T_{\rm eff}$ was analyzed by several authors under various assumptions about the atmospheric structure and the neutron-star luminosity based on numerical calculations (London *et al.* 1986; Lapidus *et al.* 1986; Ebisuzaki 1987) and on calculations using simplified analytic assumptions (Babul and Paczynski 1987; Titarchuk 1988; Pavlov *et al.* 1991; Shaposhnikov and Titarchuk 2002). According to Pavlov *et al.* (1991), in the simplest case of an exponential atmosphere,

$$T_{\rm e} \simeq T_{\rm eff}(0.14\ln\xi + 0.59)^{-4/5}\xi^{2/15}(L_{\rm B}/L_{\rm ed})^{3/20}, \quad (6)$$

where $\xi = (10/\mu_{\rm e} - 2)/(1 - L_{\rm B}/L_{\rm ed})$. Assuming, for definiteness, that $\xi = 240$, which corresponds to $L_{\rm B} \simeq 0.967L_{\rm ed}({\rm H})$ and $L_{\rm B} \simeq 0.988L_{\rm ed}({\rm He})$ for hydrogen and helium envelopes, respectively, we obtain $T_{\rm e} \simeq 1.62T_{\rm eff}$ and $R_{\rm ph} \simeq 2.62R_{bb}$. Hence, based on Table 2, we find that the photospheric radius was 5.8 ± 1.2, 27.1 ± 7.7, 21.5 ± 2.8, and 5.9 ± 3.2 km at the burst onset, at the time of the largest expansion, near the flux maximum, and at the burst decay stage, respectively. These estimates assume the distance to the system to be $d \simeq 8$ kpc. They depend on ξ, although not too strongly, i.e., on the extent to which the luminosity is close to the Eddington limit.

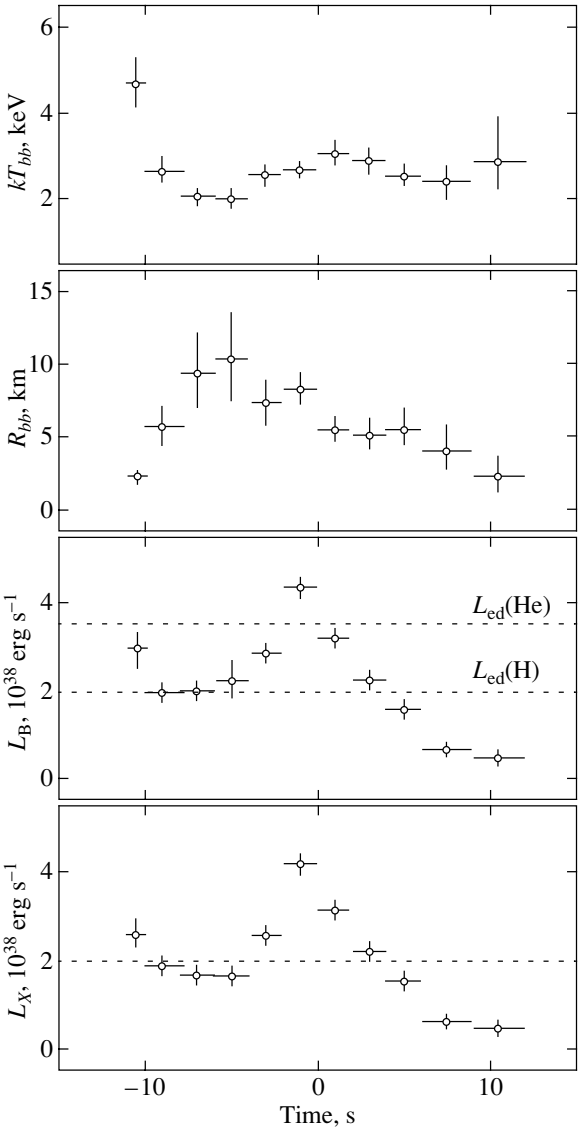

Fig. 6. Evolution of the spectral radiation parameters for the X-ray burst detected from SAX J1747.0–2853 on October 20, 1991. Time "0" on the horizontal axis corresponds to the time when the flux reached a maximum ($00^{\rm h}26^{\rm m}42^{\rm s}$ UT). The values and 1σ errors of the temperature kT_{bb}, radius R_{bb}, and bolometric luminosity $L_{\rm B} = 4\pi R_{bb}^2\sigma T_{bb}^4$ of the burst in the blackbody model are given. The distance to the source is assumed to be 8 kpc. The dotted lines indicate the Eddington luminosities $L_{\rm ed}$ for a $1.4M_\odot$ neutron star in the case of hydrogen-rich (with a helium abundance of 6.7% by the number of atoms) and purely helium atmospheres. The lower panel shows the evolution of the X-ray luminosity L_X, as inferred from direct measurements in the energy range 4–26 keV. The figure suggests an expansion of the neutron-star photosphere shortly after the burst onset accompanied by its cooling.

The Initial Pulse of Radiation

The role of Comptonization was more significant in the first moments after the burst onset, during the precursor peak, when the radiation spectrum was hardest and the bolometric luminosity $L_{\rm B}$ was a factor of $\sim$1.5 higher than the Eddington limit for a hydrogen-rich medium. At that time, the atmospheric expansion had just begun and $R_{\rm ph} \simeq R_*$. The radius R_* measured in this way was larger than the true

stellar radius R_*^0 because of the gravitational redshift,

$$R_* = R_*^0\left(1 - \frac{2GM_*}{R_*^0 c^2}\right)^{-1/2} \quad (7)$$

(e.g., Zel'dovich and Novikov 1971). In general, it must be larger than $R_{*,\,\min} = 3\sqrt{3}GM_*/c^2 \simeq 10.9(M_*/1.4M_\odot)$ km. The limiting value $R_{*,\,\min}$ is achieved for a star with $R^0_{*,\,\min} = 3GM_*/c^2 \simeq 6.3(M_*/1.4M_\odot)$ km, for which the correction for the redshift is $g = (1 - 2GM_*/R_*^0c^2)^{-1/2} \simeq 1.73$. The fact that the above estimate of $R_* \simeq (5.9 \pm 1.2)(d/8\ \mathrm{kpc})$ km is smaller than $R_{*,\,\min}$ clearly indicates that either not all of the neutron-star surface was affected by the explosion at this time or the spectrum was distorted via Comptonization more strongly than the expected one. This is attributable to a super-Eddington radiation flux and to a very high temperature of the stellar photosphere. The actual photospheric temperature (corrected for the redshift $T_0 = gT$) is even higher than the observed temperature. It can reach ~8 keV, at which formula (6) is definitely invalid. The actual photospheric luminosity also exceeds the observed luminosity $L_\mathrm{B}^0 = g^2 L_\mathrm{B}$. Concurrently, however, because of general-relativity effects, the local Eddington luminosity increases compared to its Newtonian value $L_\mathrm{ed}^0 = gL_\mathrm{ed}$, which partly compensates for the decrease in the observed ratio $L_\mathrm{B}/L_\mathrm{ed} = g^{-1}L_\mathrm{B}^0/L_\mathrm{ed}^0$.

In any case, it should be recognized that our data provide strong evidence that the photospheric luminosity during the first pulse of radiation was a super-Eddington one. After the first pulse, the internal (coming from deep within the atmosphere) luminosity may also have been at the same super-Eddington (for a hydrogen envelope) level and its decrease to the observed Eddington luminosity may have been attributable to the expenditure of energy on the atmospheric expansion. The calculations by Ebisuzaki *et al.* (1983) directly point to this possibility.

The Neutron-Star Radius

Since the photospheric radius R_ph during the burst decay approached R_*, the value of R_ph obtained for this epoch can be used to estimate the observed neutron-star radius $R_* \simeq (5.9 \pm 3.2)(d/8\ \mathrm{kpc})$ km. After the correction for the redshift using formula (7) and assuming the stellar mass to be $M_* \simeq 1.4M_\odot$, we find a 3σ upper limit for the true radius, $R_*^0 \leq 12.7(d/8\ \mathrm{kpc})$ km. This limit is in reasonable agreement with the typical neutron-star radius, 10–15 km.

Note that correction for the redshift cannot appreciably change the photospheric radius estimated for the expansion stage ($R_\mathrm{ph}^0 \simeq 25$ km at $R_\mathrm{ph} \simeq 27.1$ km). At the same time, general-relativity effects are also important here, because they contribute appreciably to the stability of the inner atmospheric layers in the neutron star, inhibiting their expansion under radiation pressure $L_\mathrm{ed}^0 = gL_\mathrm{ed}$.

The Distance to the Source

Assuming that the source luminosity during the photospheric expansion was equal to the Eddington limit for a medium with normal elemental abundances ($\mu_\mathrm{e} \simeq 1.12$), we can estimate the distance to the source,

$$d = 8(L_\mathrm{ed}/L_\mathrm{B})^{1/2}\ \mathrm{kpc} \simeq (7.89 \pm 0.37) \times (M/1.4M_\odot)^{1/2}\ \mathrm{kpc}. \quad (8)$$

Here, we used $L_\mathrm{B} \simeq (2.07 \pm 0.20) \times 10^{38}(d/8\ \mathrm{kpc})^2\ \mathrm{erg\ s^{-1}}$ obtained by averaging points 2, 3, and 4 in Fig. 6 for the bolometric luminosity. The estimated d is in excellent agreement with the distance to the Galactic center, in the field of which the source SAX J1747.0–2853 is located.

Expansion of the Helium Envelope

We see from Fig. 6 that after the hydrogen envelope was ejected (or greatly expanded and, hence, became transparent), the source luminosity continued to rise and exceeded the Eddington limit for a helium atmosphere near the burst maximum. At this time, a recurrent, weaker photospheric expansion began. This expansion manifested itself in photospheric cooling (the highest temperature in the curve of temperature variations was reached not at point 6, which corresponds to the flux maximum, but only at point 7) and in an increase of the radius (the rejection of point 6 compared to points 5 and 7 in the curve of radius evolution). For a convenient comparison, we give the temperature and radius obtained by averaging points 5 and 7 in these curves ($\langle kT_{bb}\rangle \simeq 2.80 \pm 0.17$ keV and $\langle R_{bb}\rangle \simeq 6.31 \pm 0.87$ km) and the corresponding values for point 6 ($kT_{bb} \simeq 2.67 \pm 0.15$ keV and $R_{bb} \simeq 8.20 \pm 1.07$ km). Although the statistical significance of the rejection is moderately high, the combination of all three factors (the luminosity excess above the Eddington limit, decrease in temperature, and the increase in radius) may be considered as a serious argument that the recurrent photospheric expansion actually took place.

Energy Release and the Burst Recurrence Time

Integrating L_B over time yields the total energy released in the burst, $E \simeq 4.7 \times 10^{39}(1+\xi)(d/8\ \mathrm{kpc})^2$ erg, and the mass of the exploded matter, $M \simeq E/\epsilon_N \simeq 2.6 \times 10^{21}(1+\xi)(d/8\ \mathrm{kpc})^2$ g. Here, $\epsilon_N \simeq 0.002$ s^2 is the helium burning efficiency and ξ is the fraction of energy spent on the envelope expansion. As we mentioned above, it could be appreciable. The mass of the matter involved in the expansion is small compared to M, $M_{esc} \lesssim \xi E R_*/GM_* = \epsilon_N/(0.5R_g/R_*c^2)\xi M \simeq 0.009\xi M$, where $R_g = 2GM_*/c^2$ is the gravitational radius of the neutron star. In what follows, as above, we assume that $M_* \simeq 1.4M_\odot$ and $R_* \simeq 10$ km. Using the 3σ upper limit on the accretion rate in the source that follows from the limit on its X-ray luminosity L_X in quiescence given in Table 1, $\dot{M} = L_X R_*/GM_* \leq 9 \times 10^{-11} M_\odot\ \mathrm{yr}^{-1}$, we can estimate the time it takes for this amount of matter to fall to the stellar surface, i.e., the characteristic recurrence time of such strong bursts, $\tau_r \simeq 5.3(1+\xi)$ days. It is now clear why only one such burst was detected in this session ($\Delta t \simeq 0.85$ days) over the period of ART-P observations of the source. In turn, the absence of bursts from SAX J1747.0–2853 over the entire period of ART-P observations of this region (i.e., over a period of $\sim$10 days) suggests that, on average, the luminosity of this source was a factor of $\sim$2 lower than our limit. This source was detected in a state with such a luminosity by the Chandra satellite in 2001 (Wijnands *et al.* 2002).

ACKNOWLEDGMENTS

This study was supported by the Russian Foundation for Basic Research (project nos. 99-02-18178 and 02-02-17347), the Ministry of Industry and Science of Russia (grant no. 00-15-99297 of the Russian President), and the Program "Astronomy: Nonstationary Astronomical Objects" of the Russian Academy of Sciences. S.A.G. is grateful to the INTEGRAL Science Data Center and the Max-Planck-Institut für Astrophysik for hospitality during the work on this paper. We wish to thank K.G. Sukhanov, flight director, the staffs of the Lavochkin Research and Production Center, RNIIKP, and the Deep Space Communications Center in Evpatoria; the Evpatoria team of the Space Research Institute (Russian Academy of Sciences); the team of I.D. Tserenin; B.S. Novikov, S.V. Blagii, A.N. Bogomolov, V.I. Evgenov, and N.G. Khavenson; and A.V. D'yachkov from the Space Research Institute who operated the Granat Observatory, provided the scientific planning of the mission, and performed preliminary telemetry data processing. We also wish to thank the team of M.N. Pavlinsky (Space Research Institute) and the staff of the former Research and Development Center of the Space Research Institute in Bishkek who designed and manufactured the ART-P telescope.

REFERENCES

1. A. Babul and B. Paczynski, Astrophys. J. **323**, 582 (1987).
2. A. Bazzano, P. Ubertini, J. in't Zand, *et al.*, IAC Circ. **6873** (1998).
3. S. Campana, G. L. Israel, and L. Stella, IAC Circ. **7401** (2000).
4. R. G. Cruddace, G. Fritz, S. Shulman, *et al.*, Astrophys. J. **222**, L95 (1978).
5. T. Ebisuzaki, Publ. Astron. Soc. Jpn. **39**, 287 (1987).
6. T. Ebisuzaki and K. Nomoto, Astrophys. J. **305**, L67 (1986).
7. T. Ebisuzaki, T. Hanawa, and D. Sugimoto, Publ. Astron. Soc. Jpn. **35**, 17 (1983).
8. S. A. Grebenev, A. A. Lutovinov, M. N. Pavlinsky, *et al.*, Preprint no. 2031, IKI RAN (Institute for Space Research, Russian Academy of Sciences, Moscow, 2000).
9. S. A. Grebenev, A. A. Lutovinov, M. N. Pavlinsky, *et al.*, Pis'ma Astron. Zh. **28** (2002) (in press) [Astron. Lett. **28** (2002) (in press)].
10. J. in't Zand, A. Bazzano, M. Cocchi, *et al.*, IAC Circ. **6846** (1998).
11. J. in't Zand, astro-ph/0104299 (2001).
12. I. I. Lapidus, R. A. Sunyaev, and L. G. Titarchuk, Pis'ma Astron. Zh. **12**, 918 (1986) [Sov. Astron. Lett. **12**, 383 (1986)].
13. W. Lewin, J. van Paradijs, and R. Taam, Space Sci. Rev. **62**, 223 (1993).
14. R. A. London, R. E. Tamm, and W. M. Howard, Astrophys. J. **287**, L27 (1984).
15. R. A. London, R. E. Tamm, and W. M. Howard, Astrophys. J. **306**, 170 (1986).
16. A. A. Lutovinov, S. A. Grebenev, M. N. Pavlinsky, *et al.*, Pis'ma Astron. Zh. **27**, 586 (2001) [Astron. Lett. **27**, 501 (2001)].
17. C. B. Markwardt, F. E. Marshall, and J. H. Swank, IAC Circ. **7377** (2000).
18. S. V. Molkov, S. A. Grebenev, and A. A. Lutovinov, Astron. Astrophys. **357**, L41 (2000).
19. H. Murakami, M. Sakano, K. Koyama, *et al.*, IAC Circ. **7379** (2000).
20. L. Natalucci, A. Bazzano, M. Cocchi, *et al.*, Astrophys. J. **543**, L73 (2000).
21. B. Paczynski, Astrophys. J. **267**, 315 (1983).
22. B. Paczynski and N. Anderson, Astrophys. J. **302**, 10 (1986).
23. M. N. Pavlinsky, S. A. Grebenev, and R. A. Sunyaev, Pis'ma Astron. Zh. **18**, 291 (1992) [Sov. Astron. Lett. **18**, 116 (1992)].
24. M. N. Pavlinsky, S. A. Grebenev, and R. A. Sunyaev, Astrophys. J. **425**, 110 (1994).
25. G. G. Pavlov, Yu. A. Shibanov, and V. E. Zavlin, Mon. Not. R. Astron. Soc. **253**, 193 (1991).

26. R. J. Proctor, G. K. Skinner, and A. P. Willmore, Mon. Not. R. Astron. Soc. **185**, 745 (1978).
27. N. Shaposhnikov and L. Titarchuk, Astrophys. J. **567**, 1077 (2002).
28. L. Sidoli, S. Mereghetti, G. L. Israel, *et al.*, Astron. Astrophys. **336**, L81 (1998).
29. R. A. Sunyaev, S. I. Babichenko, D. A. Goganov, *et al.*, Adv. Space Res. **10** (2), 233 (1990).
30. R. A. Sunyaev and L. G. Titarchuk, Pis'ma Astron. Zh. **12**, 857 (1986) [Sov. Astron. Lett. **12**, 359 (1986)].
31. L. G. Titarchuk, Pis'ma Astron. Zh. **14**, 537 (1988) [Sov. Astron. Lett. **14**, 229 (1988)].
32. M. G. Watson, R. Willingale, J. E. Grindlay, and P. Hertz, Astrophys. J. **250**, 142 (1981).
33. R. Wijnands, J. M. Miller, and Q. D. Wang, astro-ph/0202151 (2002).
34. Ya. B. Zel'dovich and I. D. Novikov, *Gravitational Theory and Evolution of Stars* (Nauka, Moscow, 1971).

Translated by V. Astakhov

Astronomy Letters, Vol. 28, No. 12, 2002, pp. 811–820. Translated from Pis'ma v Astronomicheskiĭ Zhurnal, Vol. 28, No. 12, 2002, pp. 902–912.

Quasi-Periodic X-ray Oscillations in the Source Scorpius X-1

S. I. Kuznetsov*

Space Research Institute, Russian Academy of Sciences, Profsoyuznaya ul. 84/32, Moscow, 117810 Russia

Received July 5, 2002

Abstract—The RXTE observations of Scorpius X-1 in 1996–1999 are presented. The properties of its quasi-periodic X-ray oscillations are studied in detail. The results obtained are used for analysis in terms of the transition-layer model (TLM) and the relativistic-precession model (RPM) for a slowly rotating neutron star. Theoretical predictions of the two models are compared and their self-consistency is verified. The tilt of the magnetosphere to the accretion-disk plane, the neutron-star mass, and its angular momentum are determined in terms of the models. © *2002 MAIK "Nauka/Interperiodica".*

Key words: *accretion, neutron stars, Scorpius X-1, X-ray sources, low-mass binary X-ray sources, quasi-periodic oscillations.*

INTRODUCTION

Scorpius X-1 is a low-mass X-ray binary with an accreting neutron star and is one of the brightest X-ray sources. Its spectral properties suggest that Scorpius X-1 belongs to the class of Z-type sources (Hasinger and van der Klis 1989), whose characteristic feature is a Z-shaped track in the color–color diagram. In this interpretation, the spectral properties are presented in the hard–soft color indices, each of which is defined as the harder-to-softer flux ratio in the corresponding energy band. The Z-shaped track is commonly divided into three parts called branches: the horizontal (HB, the upper part of the diagram), normal (NB, the intermediate part), and flaring (FB, the lower part) branches. The position on the Z track is generally believed to be associated with the rate of accretion in the direction from HB to FB. Six sources are currently known to exhibit Z tracks in the color–color diagram: Scorpius X-1, Cygnus X-2, GX 17+2, GX 5-1, GX 340+0, and GX 349+2.

The power-density spectra (Fourier transforms of the flux) of Z-type sources exhibit low-frequency (5–100 Hz) X-ray quasi-periodic oscillation (QPO) peaks. The names of the QPOs correspond to the branch with which their origin is identified: horizontal- (HBO), normal- (NBO), and flaring-branch (FBO) oscillations. HBOs (15–100 Hz) can also be detected in the NB spectral state. However, as one recedes from HB, the statistical significance of the QPO peaks decreases and they become undetectable. When moving along the Z track (from HB to FB) in its NB–FB segment, a QPO peak detectable in the 5–20 Hz range (NBO/FBO) emerges in the power-density spectra. For all the currently known Z-type sources, QPOs were also found in the range 200–1100 kHz (van der Klis 2000). Two kHz QPO peaks (ν_1 and ν_2 are the lower and upper peaks, respectively) can be simultaneously observed with a frequency difference of $\sim$200–400 Hz. For a series of successive observations (i.e., on short time scales from several hours to several days), an increase in the flux is accompanied by an increase in the frequencies of the two peaks, but their difference ($\Delta\nu = \nu_2 - \nu_1$) is not conserved (van der Klis *et al.* 1997).

The observations of Scorpius X-1 revealed all the QPO types characteristic of the low-frequency ($<$100 Hz) range in the power-density spectrum. At high frequencies, two kHz QPO peaks (ν_1 and ν_2) were found in the RXTE/PCA data [first detected by van der Klis *et al.* (1996)]. Here, we study the QPO properties in detail. Our results are used for analysis in terms of the transition-layer model (TLM) and the relativistic-precession model (RPM). We compare theoretical predictions of the two models and verify their self-consistency. The X-ray flux variability of the source at low frequencies (0.1–128 Hz) is investigated by taking into account the power-law behavior of the power-density spectrum at frequencies above and below the break frequency.

DATA AND OBSERVATIONS

For our time analysis, we used data from the Proportional Counter Array (PCA) instrument (Jahoda *et al.* 1996) onboard the RXTE observatory (Bradt *et al.* 1993) retrieved from the Goddard Space Flight Center Electronic Archive.

*E-mail: sik@hea.iki.rssi.ru

1063-7737/02/2812-0811$22.00

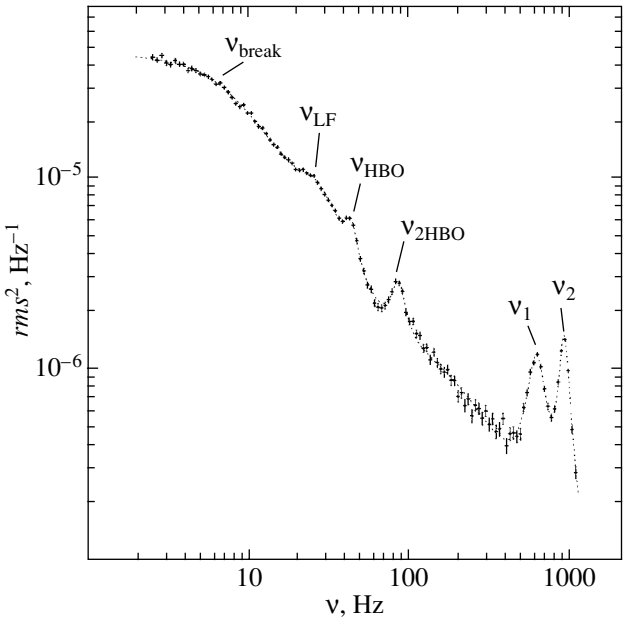

Fig. 1. The power-density spectrum for the Z-type source Scorpius X-1. The data were averaged over four consecutive observing intervals from 05 : 04 : 13 UTC on May 25, 1996. The total observing time is $\sim 10^4$ s [see a similar power-density spectrum in Titarchuk *et al.* (1999)]. The X-ray QPO peaks are shown: HBOs ($\nu_{\rm HBO}$) and their second harmonic ($\nu_{\rm 2HBO}$) and the kHz QPO peaks (ν_1 and ν_2). The break frequency is denoted by $\nu_{\rm break}$. A model fit to the data (for more details, see the text) is indicated by the dotted line. Broadband noise was detected at a statistically significant level in the average power-density spectrum at low frequencies ($\nu_{\rm LF}$).

The source Scorpius X-1 was observed by the RXTE observatory during eleven series of pointing observations (10056, 10057, 10059, 10061, 20053, 20426, 30035, 30036, 30406, 40020, and 40706): in February and May 1996; in March, April, and August 1997; in January, February, and from May until July 1998; and in January and July 1999. The observations of Scorpius X-1 over this period correspond to three different observational epochs of RXTE/PCA (1, 3, and 4 in the adopted classification), for which the boundaries of the PCA energy channels were changed.

To construct the power-density spectra, we used observational data with a resolution of $\sim$122 or $\sim$244 μs (2^{-13}, 2^{-12} s) from the zeroth to the 87th or 249th PCA energy channels. These ranges (0–87 and 0–249) correspond to a detectable photon flux $\sim$1.5–23.5, $\sim$1.9–32.3, and $\sim$2.0–38 keV for epochs 1, 3, and 4, respectively, or extend to $\sim$60 keV if the entire accessible PCA energy range (channels 0–249) was used.

Of all the observations, we used only those during which the angle between the source direction and the Earth's horizon was more than 10°. During the observations of Scorpius X-1, all five proportional counters were not always switched on to record events. If the operating condition of one of the counters changed during a continuous observation (whose duration did not exceed the duration of one orbit and was, on average, ≈ 3–3.5×10^3 s), then the time interval during which the total count rate changed abruptly was excluded from our analysis.

To analyze the variability of Scorpius X-1, we constructed its power-density spectra (van der Klis 1989) in the frequency range of 0.03125–2048 Hz (see Fig. 1). The properties of the low- and high-frequency flux variability were investigated in the bands 0.1–256 and 256–2048 Hz, respectively. No correction was made for the background radiation and dead time.

We analyzed individual observations with a duration up to $\sim 3.5 \times 10^3$ s. Fitting the power-density spectra by a constant and by a power law at frequencies below and above the break frequency did not yield acceptable results (according to the χ^2 test). The main reason was the absence of a sharp break and the resulting uncertainty in its measurement. The model in which, at frequencies much higher ($\nu/\nu_{\rm break} \gg 1$) and much lower ($\nu/\nu_{\rm break} \ll 1$) than the break, each part of the spectrum could be fitted by its own power law and the transition between them was not jumplike (previously, this model was successfully used for a time analysis of the Z-type source Cygnus X-2; see, e.g., Kuznetsov 2001) proved to be more suitable:

$$P(\nu) = A\nu^{-\alpha}[1 + (\nu/\nu_{\rm break})^{\beta}]^{-1}. \qquad (1)$$

The power-density spectra (see Fig. 1) were fitted by this model in the 0.1–256-Hz band with the additional introduction of one or two Lorenz lines to allow for the QPO peaks and their harmonics. To take into account the PCA dead-time effect, which causes the overall level to be shifted to the negative region [because of this effect, the Poissonian noise level subtracted from all spectra differed from 2.0, in units of the Leahi normalization; see van der Klis (1989) and Vikhlinin *et al.* (1994) for more details], we added a constant to the general model.

In searching for the kHz (in the range $\sim$500–1200 Hz) QPO peaks ν_1 and ν_2, we analyzed the power-density spectra at high frequencies. A constant with the addition of one or two Lorenz lines was used as the model. Individual observations in which the detection confidence level of kHz QPO peaks exceeded 3σ were used for the subsequent analysis.

Our analysis of the low-frequency flux variability in Scorpius X-1 revealed QPOs at a high confidence level in all the individual observations that corresponded to the HB or NB spectral states. Note that the HBO frequency is one of the main frequencies

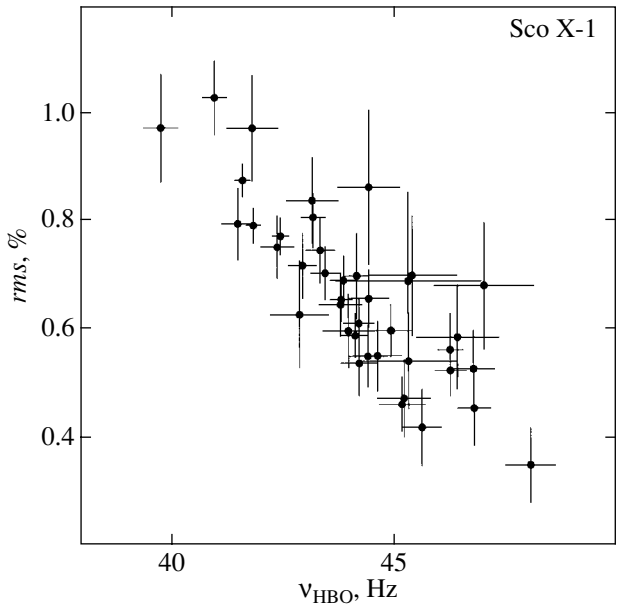

Fig. 2. The *rms* of the QPO peaks versus the HBO frequency. Individual observations are presented. As *rms* decreases, the detection confidence level of the QPO peaks falls, reaching $\sim 4\sigma$ for *rms* in the range ~ 0.4–0.5%.

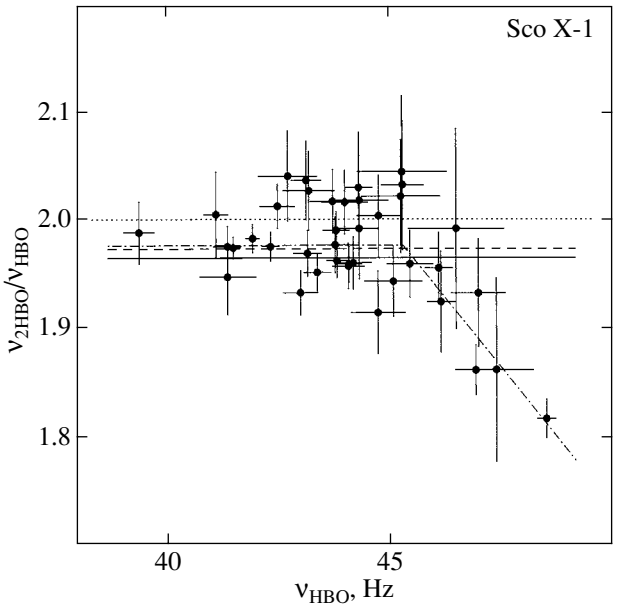

Fig. 3. The ratio of multiple HBO harmonics versus frequency $\nu_{\rm HBO}$. The solid, dash–dotted, dashed, and dotted lines represent, respectively, a constant fit to the data with statistical errors (minimization according to the χ^2 test), a constant fit with a break, the mean of individual observations (without errors), and the assumed harmonic ratio 2.0.

in most models, including the TLM and RPM. The two models (see below) unequivocally establish the correspondence between the three QPO peaks: the HBOs, and the lower and upper kHz QPOs.

To obtain the most accurate model parameters (the angle δ for the TLM and the neutron-star mass $M_{\rm NS}$ and angular momentum a for the RPM), which are invariants in each of the theories under consideration, it was necessary to calculate the three simultaneously observed main QPO frequencies (i.e., $\nu_{\rm HBO}, \nu_1$, and ν_2; see Fig. 1) as accurately as possible. Therefore, of all the preselected data in which both kHz QPO peaks (ν_1 and ν_2) were found, we used only those in which the main HBO peak ($\nu_{\rm HBO}$) and its second harmonic ($\nu_{\rm 2HBO}$) were detected at a confidence level above 4σ. In such observations, the two kHz QPO peaks were also reliably detected.

LOW-FREQUENCY X-RAY FLUX VARIABILITY

The Power of the HBO Peaks

In Fig. 2, *rms* is plotted against HBO frequency. The flux variability (i.e., rms^2) at the peak corresponds to the integral of the Lorenz line that best fits the QPO peak in the power-density spectrum. For the Z-type sources, to which Scorpius X-1 belongs, an increase in HBO frequency is accompanied by a decrease in *rms* (see, e.g., van der Klis 2000). As a result, the detection confidence level of HBO peaks is lower at high frequencies ($\sim$50–60 Hz). Figure 2 shows the range of HBO frequencies found for Scorpius X-1. During all observations, the deviation from the mean $\nu_{\rm HBO} \approx 43.5$ Hz did not exceed ~ 5 Hz (i.e., it changed by no more than 10% during all observations).

Horizontal-Branch Oscillations and Their Harmonics

In Scorpius X-1, quasi-periodic HBO peaks were found at low frequencies (<100 Hz). Together with the oscillations at the main frequency $\nu_{\rm HBO}$, we also found QPO peaks at frequencies close to the multiple ones. Note that the detection confidence level of HBO peaks decreases with frequency (see Fig. 2). That is why no multiple peaks were found (at a confidence level $>4\sigma$) for which $\nu_{\rm HBO} > 48$ Hz (the corresponding oscillation frequency of the second harmonic is $\nu_{\rm 2HBO} > 96$ Hz).

The frequency ratio $r_{2/1} = \nu_{\rm HBO}/\nu_{\rm 2HBO}$ of the multiple HBO harmonics is shown in Fig. 3. We clearly see that $r_{2/1}$ differs from 2.0: only a third of the 39 data points are above 2.0 (the dotted line in Fig. 3). Fitting by a constant yields $r_{2/1} = 1.965 \pm 0.004$ and $\chi^2_{\rm red} = 3.45$ (in what follows, $\chi^2_{\rm red} = \chi^2/{\rm d.o.f}$ is the reduced χ^2 value per degree of freedom), while fitting

by a constant with a break yields $r_{2/1} = 1.976 \pm 0.004$ and $\chi^2_{\rm red} = 1.05$ (and $r_{2/1} = -0.05 \times (\nu_{\rm HBO} - 45.31)$ in the range of a linear dependence). When the scatter of data points exceeds the statistical scatter and when the $\chi^2_{\rm red}$ value is much larger than unity (as in the case of a constant fit), it should be assumed that the uncertainty could be produced by stochastic processes rather than by the statistics alone. We can then ignore the measurement error and determine the mean $\bar{r}_{2/1} = \frac{1}{N}\sum r_{2/1}$ and the *rms* deviation from it $\sigma = \sqrt{\frac{\sum(r_{2/1} - \bar{r}_{2/1})^2}{(N-1)}}$. In this case, we obtained the following ratio of the second and first harmonics: $\bar{r}_{2/1} = 1.973$ and $\sigma = 0.050$. Under such an assumption, the harmonic ratio is compatible with 2.0, within the error limits.

Let us consider in more detail the case where the scatter of $r_{2/1}$ values about the mean is determined by the statistics alone and is incompatible with 2.0, within the error limits. Resonances in nonlinear oscillatory systems can emerge at frequencies at which an external periodic force acts on the oscillator. This requires that its frequency γ satisfy the condition

$$\gamma = \omega_0 \frac{p}{q}, \qquad (2)$$

where p and q are integers and ω_0 is the cyclic frequency of free system oscillations.

The power of the main peak must be maximal among all of the harmonics, because the intensity of resonance phenomena rapidly decreases with increasing p and q (Landau and Lifshitz 1965). In addition, if the frequency of the periodic external force γ differs from ω_0 by a small value ε (in the simplest case, $p = 1$ and $q = 1$), then in nonlinear oscillations, this can lead to a displacement of the *rms* maximum from the oscillator resonance frequency (Landau and Lifshitz 1965). In Scorpius X-1, the largest *rms* among all the HBO harmonics corresponds to the frequency $\nu_{\rm HBO}$ (see Fig. 2). We assume from the outset that the latter (and this assumption proved to be valid) was the fundamental harmonic and the deviation of the frequency ratio of the second and first harmonics from 2.0 is admitted in the forced oscillations of a nonlinear oscillator under the action of a periodic force.

Note that in this case, the frequency of the observed low-frequency oscillation peak is $\nu_{\rm HBO} \neq \omega_0/2\pi$. This is particularly important in comparing the self-consistency of the theoretical models under consideration, which interpret the emergence of QPOs (to be more precise, the following three QPOs: $\nu_{\rm HBO}$, ν_1, and ν_2) in binary systems with neutron stars.

If the deviation of the ratio of the multiple HBO harmonics $\nu_{2/1}$ from 2.0 is assumed to be attributable to forced nonlinear oscillations, then the observed $\nu_{\rm HBO}$ must be close but not exactly equal to $\omega_0/2\pi$, the assumed frequencies of free oscillations of the oscillator. Note that $\omega_0/2\pi$ rather than $\nu_{\rm HBO}$ corresponds to the low-frequency QPOs in the models considered below.

For this reason, for our analysis in terms of each of the models considered below, we use two values for the low-frequency QPOs: $\nu_{\rm HBO}$ and $\bar{\nu}_{\rm HBO}$. These values are the fundamental HBO harmonic and the mean between half the frequency of the second harmonic $\nu_{\rm 2HBO}$ and the fundamental harmonic $\nu_{\rm HBO}$. For the latter case, from all the observations, we chose those in which the confidence level of each HBO peak was higher than 4σ.

THEORETICAL MODELS

For our analysis in terms of the two models in question, we used the average spectra and the main frequencies: $\nu_{\rm HBO}$ (as well as $\bar{\nu}_{\rm HBO} = 1/2(\nu_{\rm HBO} + 1/2\nu_{\rm 2HBO})$, the mean between the fundamental harmonic and half the second harmonic), ν_1 and ν_2. The following approximate asymptotic relations between the frequencies are known from the observations of low-mass X-ray binaries (Stella *et al.* 1999): (1) $\Delta\nu = \nu_2 - \nu_1 \propto \nu_2^2$; and (2) $\nu_{\rm HBO} \propto \nu_1$. These observed features are consistent with each of the theories under consideration.

The Transition-Layer Model (TLM)

We consider the motion of a clump of matter, the QPO source on the accretion-disk surface, in a Keplerian orbit around a neutron star (NS) in terms of this model. The magnetospheric axis is assumed to be not aligned with the normal to the disk surface but makes an angle δ. After multiple passages through a slightly tilted magnetosphere, the clump comes under the effect of Coriolis forces. These forces cause the main Keplerian oscillation frequency $\nu_{\rm K}$ to split up into two oscillation modes: radial ($\nu_{\rm h}$) and perpendicular to the disk plane ($\nu_{\rm L}$). The two modes are the solution of the equation for the rotation of a body in a noninertial frame of reference [see Osherovich and Titarchuk (1999) for more details on its derivation and solution]. In this model, the lower and upper kHz QPO peaks correspond to the Keplerian ($\nu_{\rm K} \equiv \nu_1$) and hybrid ($\nu_{\rm h} \equiv \nu_2$) frequencies, respectively. The relation between the kHz QPO peaks is given by

$$\nu_{\rm h} = [\nu_{\rm K}^2 + (\Omega/\pi)^2]^{1/2}, \qquad (3)$$

where Ω is the angular velocity of the magnetosphere. The oscillation mode perpendicular to the disk surface is defined as

$$\nu_L = (\Omega/\pi)(\nu_K/\nu_h)\sin\delta. \quad (4)$$

Since all three characteristic frequencies ν_L, ν_K, and ν_h are known from observations, the sought-for angle δ can be calculated by using (4):

$$\delta = \arcsin[(\nu_h^2 - \nu_K^2)^{-1/2}(\nu_L\nu_h/\nu_K)]. \quad (5)$$

To a first approximation, the angular velocity of the magnetosphere Ω is constant. A more accurate equation that describes the dependence of Ω on the radius can be derived in the multipole magnetic-field approximation (see Osherovich *et al.* 1984). Assuming the contribution of the quadrupole component to the magnetic-field strength in the equatorial plane to be negligible and taking into account the dipole and octupole components, the final equation for the angular velocity can be represented as (Osherivich and Titarchuk 1999)

$$\Omega/2\pi = C_0 + C_1\nu_K^{4/3} + C_2\nu_K^{8/3} + C_3\nu_K^4, \quad (6)$$

with $C_2 = -2(C_1C_3)^{1/2}$.

To reconstruct the magnetospheric profile for Scorpius X-1, according to Eq. (3), it will suffice to have data only for the high-frequency range of the flux variability, i.e., ν_1 and ν_2. Therefore, we used all the data in which kHZ QPO peaks were found by removing the additional condition that the main HBO peak ν_{HBO} and its second harmonic ν_{2HBO} should be detected in the power-density spectrum at low frequencies at a confidence level above 4σ.

The angular velocity is plotted against Keplerian frequency in Fig. 4. Using (6), we managed to obtain the magnetospheric profile suggested by the model under consideration with the following parameters: $C_0 = 354$ Hz, $C_1 = -3.54 \times 10^{-2}$ Hz$^{-1/3}$, $C_2 = 9.99 \times 10^{-6}$ Hz$^{-5/3}$, and $C_3 = -7.21 \times 10^{-10}$ Hz^{-3}. In fitting the data, we assumed C_2 to be a free parameter, whereas in the model, $C_2 = -2(C_1C_3)^{1/2} = 1.01 \times 10^{-5}$. The similar values of C_2 determined by two independent methods are a weighty argument for the approximation used for the magnetospheric profile.

Using (5), we obtained δ for each triplet of frequencies: ν_{HBO}, ν_1, and ν_2. In Fig. 5 the HBO frequency ν_{HBO} is plotted against the angle δ between the normal to the disk surface and the magnetospheric axis. Among all of the three frequencies used in calculating δ, the strongest correlation is observed between δ and ν_{HBO}. For this reason, the dependence of δ on low-frequency QPOs is analyzed in the model under consideration (below, we show that this is also true for the relativistic precession model), because the model invariants must be conserved, irrespective of the measured QPO frequency range.

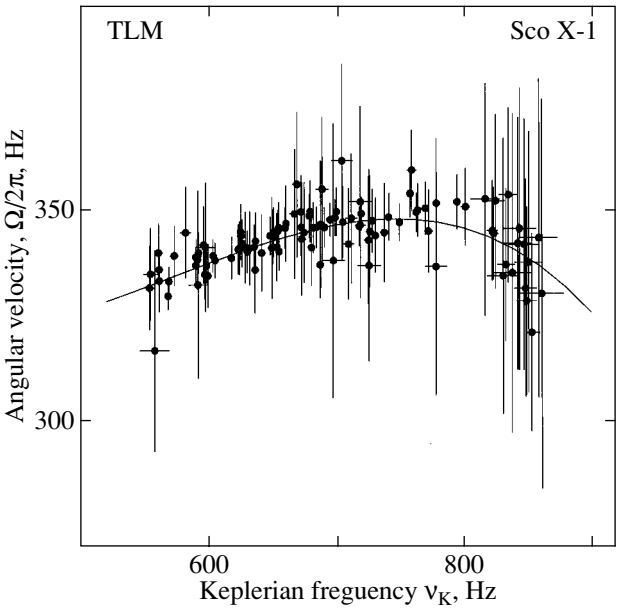

Fig. 4. The assumed angular velocity of the magnetosphere in the TLM, in units of $\Omega/2\pi$, versus Keplerian frequency ($\nu_K = \nu_1$).

Table 1 gives data on the constant fit to δ in two cases: when $\nu_L = \nu_{HBO}$ (see Fig. 5) and $\nu_L = \bar{\nu}_{HBO} = 1/2(\nu_{HBO} + 1/2\nu_{2HBO})$ (see Fig. 6), i.e., with the inclusion of the second HBO harmonic. The χ^2_{red} value is given in each case. The mean angle $\bar{\delta}$ and its rms deviation σ_D are also given in Table. 1.

To reduce the possible stochastic scatter of data points (which probably dominates over the statistical scatter), we performed averaging depending on the HBO frequency. The upper panels in Figs. 5 and 6 show the data obtained in this way. Whereas the data in Fig. 5 reveal a clear correlation between δ and ν_{HBO}, the data points in Fig. 6 virtually lie on the same

Table 1. The angle between the normal to the disk surface and the magnetospheric axis for various HBO values.

Parameter	$\nu_L = \nu_{HBO}$	$\nu_L = \bar{\nu}_{HBO}$[a]
δ	5.612 ± 0.007	5.545 ± 0.006
χ^2_{red}	5.53	2.94
$\bar{\delta}$[b]	5.600 ± 0.114	5.555 ± 0.086
N, bin	39	39

[a] $\bar{\nu}_{HBO} = 1/2(\nu_{HBO} + 1/2\nu_{2HBO})$.

[b] The quantity $\bar{\delta}$ is the mean of all δ with the error σ_D equal to the standard deviation.

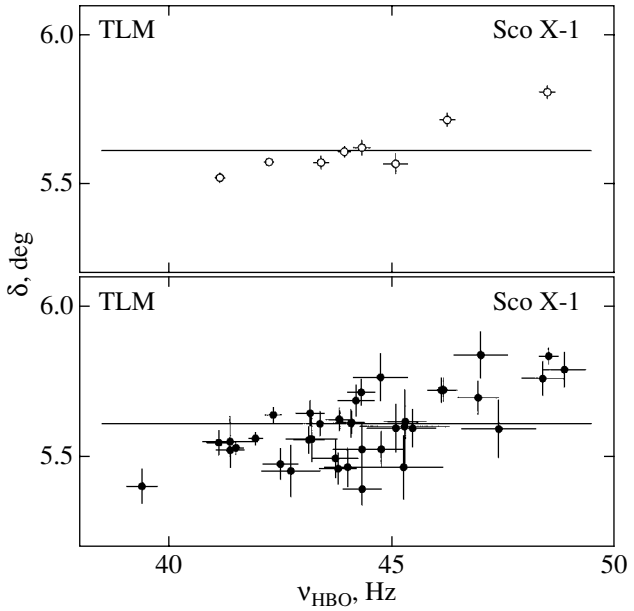

Fig. 5. The angle between the magnetospheric axis and the normal to the disk surface versus HBO frequency $\nu_{\rm HBO} \equiv \nu_{\rm L}$. A constant fit is indicated by the solid line. The lower panel shows individual observations of Scorpius X-1 with a duration up to ~3.5 ks. The upper panel shows the same observations as in the lower panel averaged over five points according to the frequency $\nu_{\rm HBO}$.

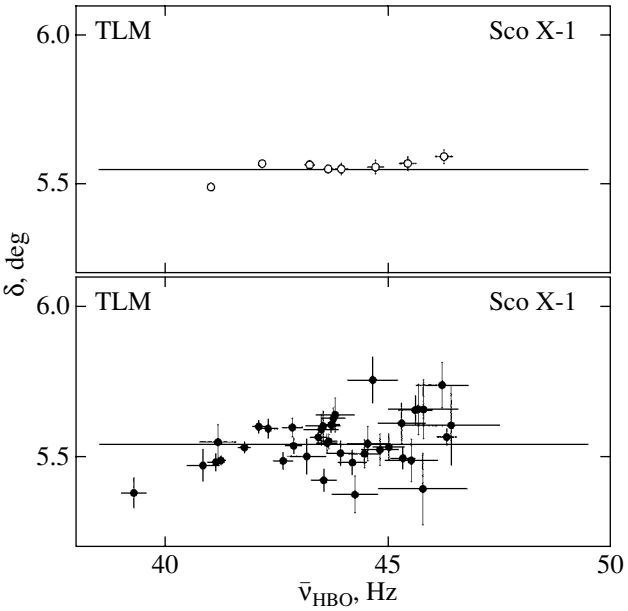

Fig. 6. The angle between the magnetospheric axis and the normal to the disk surface versus HBO frequency $\bar{\nu}_{\rm HBO} \equiv \nu_{\rm L} = 1/2(\nu_{\rm HBO} + 1/2\nu_{\rm 2HBO})$. A constant fit is indicated by the solid line. The lower panel shows individual observations of Scorpius X-1 with a duration up to ~3.5 ks. The upper panel shows the same observations as in the lower panel averaged over five points according to the frequency $\nu_{\rm HBO}$.

line. If a larger number of points in each bin were averaged (in our case, we combined them by five), then δ (see Fig. 6, where δ is plotted against $\bar{\nu}_{\rm HBO}$) would be even more compatible with a constant, according to the χ^2 test.

Let us compare the *rms* deviation between the HBO harmonic ratio $r_{2/1}$ determined above and δ (see Table 1). It turns out that $\sigma_{r_{2/1}} \approx 2.5\%$, while $\sigma_\delta \approx 2.0\%$. Since, according to (5), $\delta \propto \nu_{\rm HBO}$ at small angles and since $\nu_{\rm HBO}$ increasingly deviates from $\omega/2\pi$ to larger values with decreasing $r_{2/1}$, the correlation for δ (clearly seen only in Fig. 5) can result from the emergence of the nonlinear oscillations considered in the previous sections.

The Relativistic Precession Model (RPM)

The high-velocity motion of matter in a strong gravitational field can generate oscillations attributable to general-relativity effects. The RPM (see, e.g., Morsink *et al.* 1999) considers the motion of a point mass around a gravitating center. If a particle moves in an orbit that does not lie exactly in the equatorial plane of a compact object but is inclined at an infinitesimal angle, then the particle orbit will precess. For a nonrotating gravitating center (i.e., in the Schwarzschild approximation), the expression for the particle angular velocity matches the classical formula for Keplerian motion. However, for an NS or a black hole with an intrinsic angular momentum, the azimuthal frequency can be expressed (Bardeen *et al.* 1972; Stella *et al.* 1999) in a system of units with $G = 1$ and $c = 1$ as

$$\nu_\phi = \sqrt{\frac{M}{r^3}}\left[2\pi\left(1 + a\sqrt{\frac{M}{r^3}}\right)\right]^{-1}. \qquad (7)$$

Below, we consider only the case where the compact object and the test particle corotate: $\nu_\phi > 0$ and $a > 0$ (a is the relative angular momentum). The epicyclic frequency ν_r together with the azimuthal frequency ν_ϕ determine the orbital periastron rotation, $\nu_{\rm per} \equiv \nu_\phi - \nu_r$, while the frequency in a direction perpendicular to the disk plane ν_θ determines the nodal precession, $\nu_{\rm nod} \equiv |\nu_\phi - \nu_\theta|$. The corresponding equations were derived by Okazaki *et al.* (1987) and Kato (1990):

$$\nu_r = \nu_\phi\sqrt{1 - 6\frac{M}{r} + 8a\sqrt{\frac{M}{r^3}} - 3\frac{a^2}{r^2}}, \qquad (8)$$

$$\nu_\theta = \nu_\phi\sqrt{1 - 4a\sqrt{\frac{M}{r^3}} + 3\frac{a^2}{r^2}}. \qquad (9)$$

Table 2. The NS mass and its relative angular momentum for various HBO values.

Parameter	$\nu_{\rm nod} = \nu_{\rm HBO}$	$\nu_{\rm nod} = \bar{\nu}_{\rm HBO}$[a]	$2\nu_{\rm nod} = \nu_{\rm HBO}$	$2\nu_{\rm nod} = \bar{\nu}_{\rm HBO}$[a]
$M_{\rm NS}, M_\odot$	2.680 ± 0.002	2.675 ± 0.002	2.339 ± 0.002	2.338 ± 0.002
$\chi^2_{\rm red}$	14.3	16.3	16.4	17.5
$\bar{M}_{\rm NS}$,[b] $M_\odot$	2.677 ± 0.050	2.674 ± 0.053	2.341 ± 0.045	2.341 ± 0.045
a[c], m	1367 ± 2	1358 ± 2	663 ± 1	658 ± 1
$\chi^2_{\rm red}$	8.2	13.7	8.2	13.6
N, bin	39	39	39	39

[a] $\bar{\nu}_{\rm HBO} = 1/2(\nu_{\rm HBO} + 1/2\nu_{\rm 2HBO})$.

[b] $\bar{M}_{\rm NS}$ corresponds to the mean of all $M_{\rm NS}$ with the error equal to the standard deviation σ_D.

[c] $a = J/(c \times M_{\rm NS})$.

In contrast to the TLM, the Keplerian rotation frequency in the RPM corresponds to the upper QPO peak, $\nu_2 = \nu_\phi$, while the observed periastron precession frequency corresponds to the lower QPO peak, $\nu_1 = \nu_{\rm per} \equiv \nu_\phi - \nu_r$. In the Kerr approximation, $\nu_\phi \neq \nu_\theta$ (for the Schwarzschild case with $a = 0$, the frequencies are equal: $\nu_\phi = \nu_\theta$), the HBOs are identified with nodal precession: $\nu_{\rm nod} \equiv |\nu_\phi - \nu_\theta|$. Some authors (e.g., Stella *et al.* 1999) believe that $\nu_{\rm HBO}$ is an even harmonic of $\nu_{\rm nod}$. In contrast to $\nu_{\rm HBO} = \nu_{\rm nod}$, this relation causes the mass of the compact source required by the RPM in Eqs. (7)–(9) to decrease.

In the RPM approximation under consideration, the NS mass and relative angular momentum are invariants and do not depend on Keplerian frequency. Thus, we can determine $M_{\rm NS}$ and a from Eqs. (7)–(9) using the three observed main frequencies: $\nu_{\rm HBO}$, ν_1, and ν_2.

As in the section devoted to the TLM, here, the invariant (more specifically, the NS mass $M_{\rm NS}$ sug-

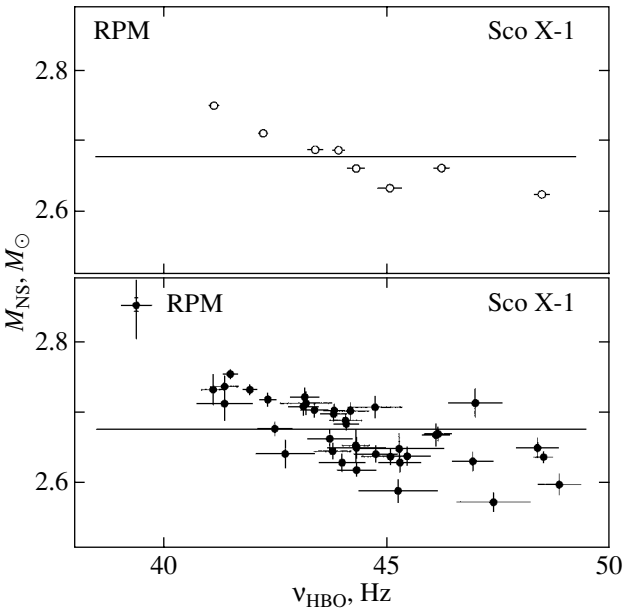

Fig. 7. NS mass versus observed HBO frequency $\nu_{\rm HBO}$. The solid line indicates a constant fit to the data. The lower panel shows individual observations of Scorpius X-1 with a duration up to ~3.5 ks. The upper panel shows the same observations as in the lower panel, averaged over five points according to the frequency $\nu_{\rm HBO}$.

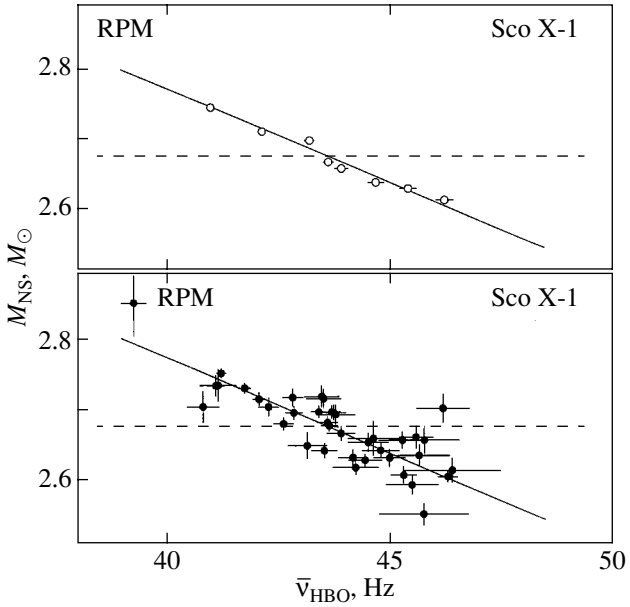

Fig. 8. NS mass versus observed HBO frequency $\nu_{\rm nod} \equiv \bar{\nu}_{\rm HBO} = 1/2(\nu_{\rm HBO} + 1/2\nu_{\rm 2HBO})$. The solid line indicates a constant fit to the data. The lower panel shows individual observations of Scorpius X-1 with a duration up to ~3.5 ks. The upper panel shows the same observations as in the lower panel, averaged over five points according to the frequency $\nu_{\rm HBO}$.

Table 3. Correlation between model invariants, δ in the TLM and $M_{\rm NS}$ in the RPM, and HBO frequency

Parameter	Model			
	TLM		RPM	
	$\nu_{\rm L} = \nu_{\rm HBO}$	$\nu_{\rm L} = \bar{\nu}_{\rm HBO}$[a]	$\nu_{\rm nod} = \nu_{\rm HBO}$	$\nu_{\rm nod} = \bar{\nu}_{\rm HBO}$[a]
r_s	0.567	0.359	−0.715	−0.789
Prob	2×10^{-4}	3×10^{-2}	3×10^{-7}	2×10^{-9}
N, bin	39	39	39	39

[a] $\bar{\nu}_{\rm HBO} = 1/2(\nu_{\rm HBO} + 1/2\nu_{\rm 2HBO})$.

Note: We used the individual observations shown in the lower panels of Figs. 5–8. The Spearman coefficient r_s close to 1 or −1 corresponds to a total positive or negative correlation between the two quantities. The probability that the observed correlation is the result of purely statistical fluctuations is given for each case.

Table 4. Correlation between model invariants, δ in the TLM and $M_{\rm NS}$ in the RPM, and HBO frequency

Parameter	Model			
	TLM		RPM	
	$\nu_{\rm L} = \nu_{\rm HBO}$	$\nu_{\rm L} = \bar{\nu}_{\rm HBO}$ [a]	$\nu_{\rm nod} = \nu_{\rm HBO}$	$\nu_{\rm nod} = \bar{\nu}_{\rm HBO}$[a]
r_s	0.738	0.595	−0.929	−1.000
Prob	3.7×10^{-2}	1.2×10^{-1}	8.6×10^{-4}	0.0
N, bin	8	8	8	8

[a] $\bar{\nu}_{\rm HBO} = 1/2(\nu_{\rm HBO} + 1/2\nu_{\rm 2HBO})$.

Note: We used the data (averaged over four or five observations) shown in the upper panels of Figs. 5–8. The Spearman coefficient r_s close to 1 or −1 corresponds to a total positive or negative correlation between the two quantities. The probability that the observed correlation is the result of purely statistical fluctuations is given for each case.

gested by the model) was also determined in two cases: $\nu_{\rm nod} = \nu_{\rm HBO}$ and $\nu_{\rm nod} = \bar{\nu}_{\rm HBO} = 1/2(\nu_{\rm HBO} + 1/2\nu_{\rm 2HBO})$ (i.e., with the inclusion of the second HBO harmonic). Since the derived $M_{\rm NS}$ proved to be most dependent (as in the TLM) on low-frequency HBOs, Figs. 7 and 8 show $M_{\rm NS}$ as a function of $\nu_{\rm HBO}$.

Table 2 gives a constant fit to the data (shown in Figs. 7 and 8). We clearly see a large $\chi^2_{\rm red}$ value for each $\nu_{\rm nod}$: compared to Table 1, which gives a fit to δ (in the TLM), the corresponding $\chi^2_{\rm red}$ values are larger by a factor of ∼3–6. Nevertheless, the *rms* deviation $\sigma_{M_{\rm NS}}$ is also ≈2.0%, as is σ_δ in the TLM. In contrast to Fig. 4, in which δ is plotted against $\bar{\nu}_{\rm HBO}$ and is essentially compatible with a constant, we clearly see a linear correlation of $M_{\rm NS}$ with $\bar{\nu}_{\rm HBO}$ in Fig. 8: as $\bar{\nu}_{\rm HBO}$ increases from ∼39.5 to ∼46.5 Hz, the required $M_{\rm NS}$ decreases from ∼2.8 to ∼2.6$M_\odot$.

The relativistic precession model makes it possible to estimate the compact-source mass and to determine the Keplerian orbital radius. For comparison, Fig. 9 shows the mass–radius relations for various equations of state for neutron stars taken from Miller *et al.* (1998).

Comparison between the Assumed Invariants of the Models under Consideration

To check whether the two models are self-consistent and to determine whether the derived invariants δ and $M_{\rm NS}$ correlate with the HBO frequency (see Figs. 5–9), we used Spearman's nonparametric correlation test. The coefficient r_s equal in magnitude to unity points to a total correlation between the two quantities. In each case under consideration, we give the probability (prob) that the correlation found is the result of statistical fluctuations. This test is also convenient in the case where it is necessary to establish which of the several correlations under consideration is strongest. Our estimates are given in Tables 3 and 4. Note that the data in Table 4 correspond to the case where the stochastic scatter was slightly reduced through averaging. Thus, the RPM model (see Table 4) is inconsistent ($r_s = -1$; the total negative correlation between $M_{\rm NS}$ and $\bar{\nu}_{\rm HBO}$) and the assumed NS mass is not an invariant in this model.

Allowance for the second harmonic in determining the low-frequency QPO peak (more specifically, $\bar{\nu}_{\rm HBO} = 1/2(\nu_{\rm HBO} + 1/2\nu_{\rm 2HBO})$) results in a reduction of the correlation coefficient r_s for δ in the TLM, while the reverse is true for $M_{\rm NS}$. In particular, we see from Fig. 8 that the data points are well fitted by a straight line: $\chi^2_{\rm red} = 4.31$ (see Table 2, where $\chi^2_{\rm red} = 16.3$ for the same case but for a constant fit to the data). Figures 6 and 8 (upper panels) show that averaging can reduce the stochastic scatter when determining the model invariants. However, for the TLM (see Fig. 6), δ is virtually constant, $\bar{\delta} = 5.55$, and the *rms* deviation $\sigma_{\bar{\delta}} = 0.03$ (which is $\approx 0.5\%$); while for the RPM (see Fig. 8), $M_{\rm NS}$ strongly correlates with $\bar{\nu}_{\rm HBO}$ and is incompatible with a constant (the *rms* deviation is $\sigma_{\bar{M}_{\rm NS}} \approx 1.7\%$, which roughly corresponds to $\sigma_{M_{\rm NS}}$; see Table 2).

DISCUSSION AND RESULTS

Both theoretical models suggest the existence of invariants. These invariants are the tilt of the magnetosphere to the normal disk δ for the TLM and the NS mass $M_{\rm NS}$ and its relative angular momentum a for the RPM in the Kerr approximation. Since the RPM did not consider the quadrupole moment of the compact source and disregarded its oblateness (which can give a contribution of ~ 10–15% to the nodal precession frequency), we managed to avoid the inclusion of various theoretical equations of state of neutron stars in our analysis. However, it was of interest to compare our results with the constraints imposed on the equations of state. Figure 9 shows some of these constraints taken from Miller *et al.* (1998). The curves correspond to the mass–radius relation for nonrotating neutron stars. Although the angular velocity for Scorpius X-1 is nonzero, the correction for spin (here, $\nu_s \approx 200$–400 Hz) can be disregarded.

The assumed NS mass $M_{\rm NS}$ and the Keplerian orbital radius R of the particle rotating around it (see Fig. 9) derived from Eqs. (7)–(9) must be consistent with the constraints imposed by the equations of state. More specifically, $M_{\rm NS} < M_{\rm EOS}$, $R > R_{\rm EOS}$ (here, $M_{\rm EOS}$ and $R_{\rm EOS}$ are the NS mass and radius for various equations of state). Only the equation of state "L" suggests that a massive NS (in our case, $\sim 2.7 M_\odot$) could exist and it agrees with the derived $M_{\rm NS}$ in the two cases ($\nu_{\rm nod} = \nu_{\rm HBO}$ and $2\nu_{\rm nod} = \nu_{\rm HBO}$). At the same time, the other two equations of state ("A" and "UU") are incompatible with the RPM results in the Kerr (i.e., with NS rotation) approximation. Moreover, we obtained $M_{\rm NS}$ for Cygnus X-2 that was compatible, within the error limits ($M_{\rm NS} = 2.69 \pm 0.10$ for $\nu_{\rm nod} = \nu_{\rm HBO}$ and $M_{\rm NS} = 2.29 \pm 0.09$ for $2\nu_{\rm nod} = \nu_{\rm HBO}$; Kuznetsov 2002), with $M_{\rm NS}$ for Scorpius X-1 (see Table 2). Such a coincidence is not an argument for the relativistic precession model either.

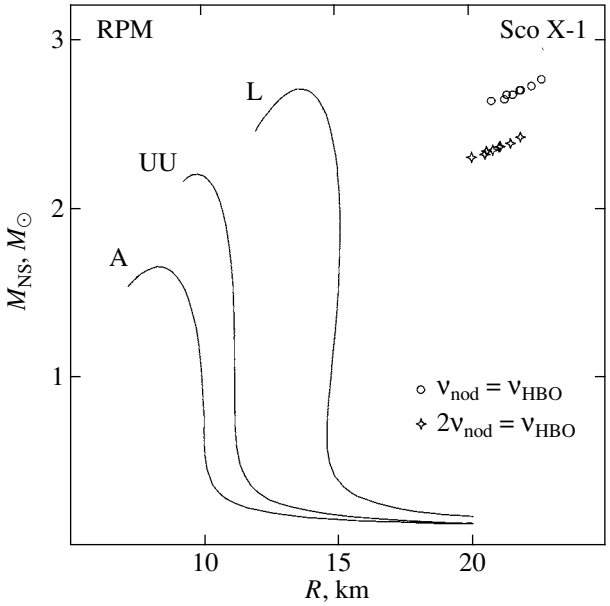

Fig. 9. Relationship of the NS mass to the nodal precession frequency and Keplerian orbital radius. The circles correspond to the mass–radius relation in the case where the nodal precession frequency is identically equal to the HBO frequency $\nu_{\rm HBO}$; the diamonds correspond to the case where it is assumed to be its even harmonic (for more details, see the text). The solid lines [taken from Miller *et al.* (1998)] represent the mass-radius relations for several equations of state for neutron stars.

In addition, we showed that a nonparametric test for correlation between the assumed NS mass in the RPM and the HBO frequency yields a positive result. Thus, the RPM is not a self-consistent model in which the invariants are conserved and the derived mass of the compact object is large enough for the existing equations of state for neutron stars. At the same time, for the transition-layer model, the derived value is compatible with a constant under certain conditions (e.g., using the theory of nonlinear oscillations; for more details, see Kuznetsov and Titarchuk 2002). If the uncertainty in the calculated angle δ does not exceed $\sim 2\%$ (which is lower than the *rms* deviation for δ in Scorpius X-1; see Table 1), then its value may be assumed to be constant.

The observed inconsistency of the RPM may stem from the fact that the orbital inclination of the test particle in the model simplification is assumed to be infinitesimal. An exact solution for an arbitrary inclination is given in Sibgatullin (2001). In such an analysis, the frequency $\nu_{\rm HBO}$ for a fixed mass and angular momentum can change by a factor of ~ 3 as the inclination changes from 0 to $\pi/2$ (for the marginally stable orbit at $M_{\rm NS} = 2M_\odot$ and $\nu_\phi = 1200$ Hz). This

dispenses with the need to take the nodal precession frequency ν_{nod} to be equal to 1/2 of ν_{HBO} to obtain more acceptable NS-star masses.

In addition, it is worth noting that the angle δ in the RPM may not be strictly an invariant. A higher energy release in the disk can affect the curvature of its inner region. The tilt angle δ between the magnetospheric axis and the normal to the disk surface can then differ for different source fluxes. As a result, the angles δ can differ for the same ν_{HBO} (see Figs. 5 and 6).

ACKNOWLEDGMENTS

This study was supported in part by the Program of the Russian Academy of Sciences "Astronomy: Nonstationary Astronomical Phenomena," the Russian Foundation for Basic Research (project no. 02-02-17347), and grant no. 00-15-99297 of the President of Russia. I used the RXTE data retrieved from the Goddard Space Flight Center Electronic Archive. I wish to thank L. Titarchuk, B. Stone, N. White, J. Swank, Ph. Newman, and J. Repaci for the opportunity to work with the RXTE archival data on CD-ROMs. I am grateful to the referee for helpful remarks and comments.

REFERENCES

1. J. M. Berdeen, W. H. Press, and S. A. Teukolski, Astrophys. J. **178**, 374 (1972).
2. H. Bradt, R. Rotschild, and J. Swank, Astron. Astrophys., Suppl. Ser. **97**, 335 (1993).
3. G. Hasinger and M. van der Klis, Astron. Astrophys. **225**, 79 (1989).
4. K. Jahoda, J. Swank, A. Giles, *et al.*, *EUV, X-ray and Gamma-ray Instrumentation for Astronomy VII,* Ed. by O. Siegmund and M. Gummin, Proc. SPIE **2808**, 59 (1996).
5. S. Kato, Publ. Astron. Soc. Jpn. **42**, 99 (1990).
6. S. I. Kuznetsov, Pis'ma Astron. Zh. **27**, 919 (2001) [Astron. Lett. **27**, 790 (2001)].
7. S. I. Kuznetsov, Pis'ma Astron. Zh. **28**, 88 (2002) [Astron. Lett. **28**, 73 (2002)].
8. S. Kuznetsov and L. Titarchuk, Astrophys. J. **571**, 137L (2002).
9. L. D. Landau and E. M. Lifshitz, *Course of Theoretical Physics,* Vol. 1: *Mechanics* (Nauka, Moscow, 1965; Pergamon, New York, 1988).
10. M. C. Miller, F. K. Lamb, and D. Psaltis, Astrophys. J. **508**, 791 (1998).
11. S. Morsink and L. Stella, Astrophys. J. **513**, 827 (1999).
12. T. Okazaki, S. Kato, and J. Fukue, Publ. Astron. Soc. Jpn. **39**, 457 (1987).
13. V. Osherovich and L. Titarchuk, Astrophys. J. **522**, 113 (1999).
14. V. Osherovich, I. Tzur, and E. Gliner, Astrophys. J. **284**, 412 (1984).
15. N. R. Sibgatullin, Pis'ma Astron. Zh. **27**, 929 (2001) [Astron. Lett. **27**, 799 (2001)].
16. L. Stella, M. Vietry, and S. M. Morsink, Astrophys. J. **524**, L66 (1999).
17. L. Titarchuk, V. Osherovich, and S. Kuznetsov, Astrophys. J. **525**, L129 (1999).
18. M. van der Klis, *Timing Neutron Stars,* Ed. by H. Ögelman and E. P. J. van der Heuvel (Kluwer, Dordrecht, 1989), NATO ASI Ser., Ser. C, Vol. 360, p. 27.
19. M. van der Klis, Annu. Rev. Astron. Astrophys. **38**, 717 (2000).
20. M. van der Klis, J. H. Swank, W. Zhang, *et al.*, Astrophys. J. **469**, L1 (1996).
21. M. van der Klis, R. Wijnands, K. Horne, and W. Chen, Astrophys. J. **481**, L97 (1997).
22. A. Vikhlinin, E. Churazov, and M. Gilfanov, Astron. Astrophys. **287**, 73 (1994).

Translated by V. Astakhov

Astronomy Letters, Vol. 28, No. 12, 2002, pp. 821–834. Translated from Pis'ma v Astronomicheskiĭ Zhurnal, Vol. 28, No. 12, 2002, pp. 913–927.

The Possibility of Emersion of the Outer Layers in a Massive Star Simultaneously with Iron-Core Collapse: A Hydrodynamic Model

V. S. Imshennik*, K. V. Manukovskii, D. K. Nadyozhin, and M. S. Popov

Institute for Theoretical and Experimental Physics, ul. Bol'shaya Cheremushkinskaya 25, Moscow, 117259 Russia

Received January 30, 2002; in final form, July 4, 2002

Abstract—We analyze the behavior of the outer envelope in a massive star during and after the collapse of its iron core into a protoneutron star (PNS) in terms of the equations of one-dimensional spherically symmetric ideal hydrodynamics. The profiles obtained in the studies of the evolution of massive stars up to the final stages of their existence, immediately before a supernova explosion (Boyes *et al.* 1999), are used as the initial data for the distribution of thermodynamic quantities in the envelope. We use a complex equation of state for matter with allowances made for arbitrary electron degeneracy and relativity, the appearance of electron–positron pairs, the presence of radiation, and the possibility of iron nuclei dissociating into free nucleons and helium nuclei. We performed calculations with the help of a numerical scheme based on Godunov's method. These calculations allowed us to ascertain whether the emersion of the outer envelope in a massive star is possible through the following two mechanisms: first, the decrease in the gravitational mass of the central PNS through neutrino-signal emission and, second, the effect of hot nucleon bubbles, which are most likely formed in the PNS corona, on the envelope emersion. We show that the second mechanism is highly efficient in the range of acceptable masses of the nucleon bubbles ($\leq 0.01 M_\odot$) simulated in our hydrodynamic calculations in a rough, spherically symmetric approximation.

Key words: *plasma astrophysics, hydrodynamics, and shock waves.*

INTRODUCTION

The root cause of supernova explosions in massive stars ($M_{\rm MS} \geq 10 M_\odot$) after the completion of their thermonuclear evolution is commonly assumed to be the gravitational collapse of their central iron cores with masses $M_{\rm Fe}$ in a narrow range ($1.2 M_\odot \leq M_{\rm Fe} \leq 2 M_\odot$); the lower limit is approximately equal to the Chandrasekhar mass of an iron white dwarf. To be more precise, iron-core collapse is followed by a number of hydrodynamic processes in the compact central part of the cavity left from the iron core.

Hydrodynamic spherically symmetric models for the gravitational collapse of iron stellar cores [see, e.g., the review article by Imshennik and Nadyozhin (1982)] showed a clear separation of the collapse into two stages. At the first stage, the inner iron core with mass $M_{i\rm Fe} \leq 1 M_\odot$ (Imshennik 1992) or, to be more precise, with mass $(0.6–0.8) M_\odot$ (Nadyozhin 1998) collapses homologically. The remaining outer iron core with mass $M_{e\rm Fe} = M_{\rm Fe} - M_{i\rm Fe} \cong (0.4–1.4) M_\odot$ in the above range of iron-core masses lags well behind the inner core in contraction parameters (density, etc.). In a rough approximation, it can even be assumed to maintain the hydrostatic equilibrium of the initial state. Since these issues were discussed previously (Imshennik and Zabrodina 1999; Imshennik and Popov 2001), the hydrodynamic behavior of the outer iron core and outer layers of a massive star may be called the problem of their post-shock accretion (Brown *et al.* 1992) onto the embryo of a protoneutron star (PNS) with a mass of about $1 M_\odot$ formed at the end of the first collapse stage. The second collapse stage of the matter surrounding this PNS embryo can be identified with this post-shock accretion. Literally, this implies that at the initial time, there is a collapsed central object with mass $1 M_\odot$ and its surrounding layers in an initially hydrostatic equilibrium. These initial conditions for the model of post-shock accretion considered below seem to be in qualitative agreement with hydrodynamic models for the collapse of iron stellar cores. They allow the hydrodynamic processes in the remaining onionlike part of the star surrounding the iron core in a massive star of arbitrary total mass ($M_{\rm MS} \geq 10 M_\odot$) to be included in the analysis. Here, we show that these processes do not result in an explosion of the outer stellar layers surrounding the iron core as during a supernova explosion ($\sim 10^{51}$ erg). However, in the

*E-mail: imshennik@vxitep.itep.ru

presence of low-mass ($\leq 0.01 M_\odot$) nucleon bubbles, they cause the emersion of the outer layers with a relatively low energy and with a total mass of several $M_\odot$ up to the inner boundary of the helium shell.

FORMULATION OF THE PROBLEM

The System of Equations

In most cases, the hydrodynamic behavior of the envelope in a massive star can be described by the system of equations of ideal hydrodynamics. In our spherically symmetric case $\left(\frac{\partial}{\partial\theta}, \frac{\partial}{\partial\varphi}, g_\theta = 0, g_\varphi = 0\right)$, this system in spherical coordinates (r, θ, φ) is known to be

$$\frac{\partial\rho}{\partial t} + \frac{1}{r^2}\frac{\partial}{\partial r}(r^2\rho V_r) = 0, \quad (1)$$

$$\frac{\partial\rho V_r}{\partial t} + \frac{1}{r^2}\frac{\partial}{\partial r}(r^2\rho V_r^2) + \frac{\partial P}{\partial r} = \rho g_r, \quad (2)$$

$$\frac{\partial\rho E}{\partial t} + \frac{1}{r^2}\frac{\partial}{\partial r}(r^2 V_r(\rho E + P)) = \rho V_r g_r. \quad (3)$$

Here, $E = \varepsilon + \frac{\mathbf{v}^2}{2}$ is the sum of the specific inner (ε) and kinetic energies. The radial acceleration of gravity g_r is the sum of two components: $g_r = g_{\rm pns} + g_{\rm env}$. The first component is attributable to the gravitational field produced by the PNS located exactly at the coordinate origin:

$$\mathbf{g}_{\rm pns} = \left(-\frac{GM_{\rm pns}}{r^2}, 0, 0\right). \quad (4)$$

The second component is attributable to the intrinsic gravitational field of the stellar envelope. The acceleration of this field is defined by the standard equation $\mathbf{g}_{\rm env} = -\nabla\Phi$ and the potential satisfies the Poisson equation

$$\Delta\Phi = 4\pi G\rho. \quad (5)$$

In our calculations, we actually used a numerical scheme based on the equations of ideal hydrodynamics written in axisymmetric form $\left(\frac{\partial}{\partial\varphi}, g_\varphi = 0\right)$ in spherical coordinates (r, θ, φ):

$$\frac{\partial\rho}{\partial t} + \frac{1}{r^2}\frac{\partial}{\partial r}(r^2\rho V_r) + \frac{1}{r\sin\theta}\frac{\partial}{\partial\theta}(\sin\theta\rho V_\theta) = 0, \quad (6)$$

$$\frac{\partial\rho V_r}{\partial t} + \frac{1}{r^2}\frac{\partial}{\partial r}(r^2\rho V_r^2) + \frac{1}{r\sin\theta}\frac{\partial}{\partial\theta}(\sin\theta\rho V_r V_\theta) + \frac{\partial P}{\partial r} - \frac{\rho(V_\theta^2 + V_\varphi^2)}{r} = \rho g_r, \quad (7)$$

$$\frac{\partial\rho V_\theta}{\partial t} + \frac{1}{r^2}\frac{\partial}{\partial r}(r^2\rho V_r V_\theta) + \frac{1}{r\sin\theta}\frac{\partial}{\partial\theta}(\sin\theta\rho V_\theta^2) + \frac{1}{r}\frac{\partial P}{\partial\theta} + \frac{\rho V_r V_\theta}{r} - \frac{\rho V_\varphi^2\cot\theta}{r} = \rho g_\theta, \quad (8)$$

$$\frac{\partial\rho V_\varphi}{\partial t} + \frac{1}{r^2}\frac{\partial}{\partial r}(r^2\rho V_r V_\varphi) + \frac{1}{r\sin\theta}\frac{\partial}{\partial\theta}(\sin\theta\rho V_\theta V_\varphi) + \frac{\rho V_\varphi}{r}(V_r + \cot\theta V_\theta) = 0, \quad (9)$$

$$\frac{\partial\rho E}{\partial t} + \frac{1}{r^2}\frac{\partial}{\partial r}(r^2 V_r(\rho E + P)) + \frac{1}{r\sin\theta}\frac{\partial}{\partial\theta}(\sin\theta V_\theta(\rho E + P)) = \rho(V_r g_r + V_\theta g_\theta). \quad (10)$$

As can be easily verified, this system transforms to the system of equations (1)–(3) if we set V_θ, V_φ, and g_θ equal to zero.

Equations (6)–(10) are written in divergence form; since they do not contain viscosity, including artificial viscosity, shock and contact discontinuities can emerge in their solutions. The absence of heat conductivity in these equations makes discontinuities in specific internal energy and density admissible. This can be taken into account when choosing a finite-difference scheme.

Initial Data

As we noted in the Introduction, the formation time of the PNS embryo with the mass ($\sim 1 M_\odot$) characteristic of our problem, when the neutron signal also increases most steeply (even before its maximum), may by arbitrarily taken as the initial time ($t = 0$). In that case, the outer layers may still be considered in a hydrostatic equilibrium. We used the distributions of thermodynamic quantities obtained in the studies of the evolution of massive stars (Boyes *et al.* 1999) as the initial data. From this paper, we took the density and temperature profiles, which, in turn, serve to determine the initial pressure and internal energy by using a specified equation of state. Of course, the equation of state used in our calculations slightly differs from the equation of state used in obtaining these profiles. The main difference is that we took a large number of isotopes into account in our numerical calculations of stellar evolution. However, a detailed comparison of the equations of state shows that, quantitatively, these differences are moderately large and passing to a simpler equation of state in our calculations has no significant effect on the radial distributions of thermodynamic quantities. The pressure calculated from fixed density and temperature using our equation of state differs by no more than 2% along the entire profile from the pressure taken from

Boyes *et al.* (1999); the pressure from Boyes *et al.* (1999) is lower approximately by 2% near the iron core and higher by the same ~2% in the profile tail. Nevertheless, to exactly specify hydrostatically equilibrium distributions of thermodynamic quantities in our calculations as the initial data, we recalculated the initial profiles using a new equation of state. As was noted above, by the formation of a PNS embryo with a typical mass of $\sim 1M_\odot$, the outer layers surrounding the iron core are virtually in hydrostatic equilibrium, as suggested by hydrodynamic collapse calculations (Nadyozhin 1977). To be more precise, the radial temperature distribution from Boyes *et al.* (1999) was used in these calculations and the new distributions of pressure and the remaining thermodynamic quantities (ρ, e) were reconstructed by solving the system of hydrostatic equilibrium equations

$$\frac{\partial P}{\partial r} = -\frac{Gm\rho}{r^2}, \tag{11}$$

$$\frac{\partial m}{\partial r} = 4\pi r^2 \rho; \tag{12}$$

the pressure P and mass m at the inner boundary were also taken from Boyes *et al.* (1999). The dimensions of the computed region were chosen in such a way that the inner boundary was equal to the radius that bounded the region of mass $1M_\odot$ in the initial profile and the outer (in radius) boundary coincided with the inner boundary of the helium shell. The calculations were performed for the evolutionary models of stars with masses of 11, 20, and $25M_\odot$ and solar metallicity Z.

The initial values of the velocity component V_r were taken to be zero in all cases, except for an additional calculation in which we imparted a velocity approximately equal to the free-fall velocity in magnitude and directed away from the center.

In all of our calculations, we took into account the presence of a neutrino signal. The gravitational collapse of massive stellar cores gives rise to a powerful neutrino signal, as predicted by Nadyozhin (1978) and experimentally confirmed by the observations of the SN 1987A explosion in the Large Magellanic Cloud. The neutrino signal carries away almost all of the gravitational binding energy of the forming neutron star, which is released during the collapse. The total gravitational mass defect of the neutron star was calculated by using the formula $\Delta M_G = 0.084\dfrac{M_{\rm Fe}^2}{M_\odot}$ (Lattimer and Yahil 1989), which is $\Delta M_G = 0.054$, 0.165, and $0.336M_\odot$ for iron cores with masses $M_{\rm Fe} = 0.8$, 1.4, and $2.0M_\odot$, respectively. It should be immediately noted that these values of ΔM_G refer to cold neutron stars; i.e., they definitely overestimate the effect under consideration, because a hot PNS still has high internal energy and temperature. The shape of the neutrino-signal curve in time was taken from Nadyozhin (1978). During the calculation, it was fitted by a set of exponentials that were continuously joined at the boundary points.

Boundary Conditions

The region of the solution of the problem or the computed region has the shape of a spherical envelope (see above), $r_{\rm min} \le r \le r_{\rm max}$; the choice of $r_{\rm min}$ and $r_{\rm max}$ is determined by the physical considerations outlined in the Subsection "Initial Data." Sufficient boundary conditions must be specified precisely on these constant values of the Eulerian radius.

Thus, in our problem, the computed region has the Eulerian outer and inner boundaries, $r_{\rm min}$ and $r_{\rm max}$. The inner boundary is a transparent wall; i.e., the derivatives of all physical quantities (v_r, ρ, and ε) are assumed to be zero. Matter can then freely flow through the inner boundary. In that case, the accretion rate or, more precisely, the total mass of the matter passing through it per unit time is calculated at this boundary. At the outer boundary, the condition simulates a vacuum outside the computed region; i.e., the thermodynamic quantities (ρ, ε, and P) are set equal to nearly zero. The boundary condition for the gravitational potential is $\Phi \to -GM/r$ for $r \to \infty$. Recall that we use the numerical scheme of a two-dimensional problem (see the Section "The System of Equations").

THE EQUATION OF STATE

We use the equation of state for matter treated as a mixture of a perfect Boltzmann gas of nuclei, a perfect Fermi–Dirac electron–positron gas, and blackbody radiation. In a wide temperature range, the matter is assumed to be a mixture of a perfect iron gas of nuclei, a perfect electron–positron gas, and blackbody radiation. However, in order that the equation of state be applicable under nuclear-statistical-equilibrium (NSE) conditions, i.e., at high temperatures $T > T_{\rm c}$, where $T_{\rm c} = (3\text{–}5) \times 10^9$ K (Imshennik and Nadyozhin 1965, 1982), virtually independent of the matter density ρ (Imshennik *et al.* 1981), we assume that at $T > T_{\rm c}$, the matter is a mixture of perfect gases of four nuclides, ${}_0^1n$, ${}_1^1p$, ${}_2^4$He, ${}_{26}^{56}$Fe, with a perfect gas of e^-, e^+ leptons and blackbody radiation. Including many other nuclides should not significantly affect the thermodynamic functions of the matter.

The contribution of the electron–positron component is given by general integral equations with arbitrary degeneracy and relativity. The difference between the electron and positron number densities can be determined from the necessary condition of

electrical neutrality. In turn, the latter in the form of a simple integral equation serves to calculate the electron chemical potential (μ):

$$\frac{1}{\lambda^3}\int_0^\infty [F_-(\xi)-F_+(\xi)]d\xi \qquad (13)$$
$$=\frac{\rho}{m_u}\left(\frac{26}{56}X_{\rm Fe}+\frac{1}{2}X_{\rm He}+X_p\right),$$

where $X_{\rm Fe}$, $X_{\rm He}$, and X_p are the mass fraction of iron, helium, and free protons; and $F_\pm(\xi)$ under the integral are the Fermi–Dirac functions. For arbitrary degeneracy and relativity of $e^\pm$ leptons, these functions can be expressed explicitly:

$$F_\pm(\xi)=\xi^2\left(1+\exp z_\pm(\xi)\right)^{-1}, \qquad (14)$$
$$z_\pm(\xi)=\alpha(\sqrt{1+\xi^2}\pm w),$$

because $\mu\equiv\mu_-=-\mu_+$. Here, we introduced the dimensionless parameters $\alpha\equiv\dfrac{m_{\rm e}c^2}{k_{\rm B}T}$ and $w\equiv\dfrac{\mu}{m_{\rm e}c^2}$, where T is the temperature, $k_{\rm B}$ is the Boltzmann constant, $m_{\rm e}$ is the electron mass, μ is the chemical potential (including the fermion rest energy), and the quantity λ as the natural unit of length (of the order of the Compton length) $\lambda^3=\dfrac{1}{8\pi}\left(\dfrac{h}{m_{\rm e}c}\right)^3$.

The equation of state proper, i.e., the expressions for the pressure and specific internal energy of the matter, is then (Imshennik and Nadyozhin 1965, 1982)

$$P=P_-+P_++\frac{1}{3}aT^3 \qquad (15)$$
$$+\frac{k_{\rm B}}{m_u}\rho T\left(X_n+X_p+\frac{1}{4}X_{\rm He}+\frac{1}{56}X_{\rm Fe}\right),$$

$$\varepsilon=\varepsilon_-+\varepsilon_++\frac{aT^4}{\rho}+\frac{3}{2}\frac{k_{\rm B}}{m_u}T \qquad (16)$$
$$\times\left(X_n+X_p+\frac{1}{4}X_{\rm He}+\frac{1}{56}X_{\rm Fe}\right)$$
$$+\left[\frac{Q_{\rm Fe}+26\Delta Q_n}{56m_u}(1-X_{\rm Fe})\right.$$
$$\left.-\frac{Q_{\rm He}+2\Delta Q_n}{4m_u}X_{\rm He}-\frac{\Delta Q_n}{m_u}X_p\right].$$

Here, $\Delta Q_n=(m_n-m_p)c^2=1.294$ MeV is the energy threshold of β decay and $a=7.5644\times10^{-15}$ erg cm^{-3} K^{-1} is the neutron radiation density constant.

The contributions of the lepton pressure and specific internal energy to the complete equation of state are given by standard general relations (Landau and Lifshitz 1976) [with definitions (14)]:

$$P_-+P_+=\frac{m_{\rm e}c^2}{3\lambda^3}\int_0^\infty\frac{\xi^2}{\sqrt{1+\xi^2}}[F_-(\xi)+F_+(\xi)]d\xi, \qquad (17)$$

$$\varepsilon_-+\varepsilon_+=\frac{m_{\rm e}c^2}{\lambda^3\rho}\int_0^\infty\sqrt{1+\xi^2}\,[F_-(\xi)+F_+(\xi)]\,d\xi \qquad (18)$$
$$-m_{\rm e}c^2\left(\frac{26}{56}\frac{1}{m_u}\right).$$

Note that a constant electron rest energy at zero temperature (in the absence of positrons) is subtracted from the sum of ε_+ and ε_-. Clearly, the specific internal energies can generally be determined to within an arbitrary constant.

The mass fractions of iron, helium, free neutrons, and free protons under NSE conditions at a given density and temperature are defined by the system of equations (Imshennik and Nadyozhin 1965, 1982; Imshennik and Zabrodina 1999)

$$X_i=\omega_iA^{5/2}\left(\frac{h^2}{2\pi m_uk_{\rm B}T}\right)^{\frac{3}{2}(A_i-1)}\frac{1}{2^{A_i}} \qquad (19)$$
$$\times\left(\frac{\rho}{m_u}\right)^{A_i-1}X_n^{A_i-Z_i}X_p^{Z_i}\exp\left(\frac{Q_i}{kT}\right),$$

$$\theta_0=\frac{X_n+(1/2)X_{\rm He}+(30/56)X_{\rm Fe}}{X_p+(1/2)X_{\rm He}+(26/56)X_{\rm Fe}}=\frac{30}{26}, \qquad (20)$$

$$X_n+X_p+X_{\rm He}+X_{\rm Fe}=1, \qquad (21)$$

where $i=$ He, Fe; m_u is the atomic mass unit; Q_i is the binding energy in the ground state of the nuclides ($Q_{\rm He}=28.296$ MeV, $Q_{\rm Fe}=492.26$ MeV); A_i and Z_i are the mass and charge numbers of these nuclides; and ω_i are the partition functions, which may be taken to be unity without any particular error. Here, we assumed the ratio of the total numbers of neutrons and protons to be constant; $\theta=30/26=\theta_{\rm Fe}$ is the value typical for the $^{56}_{26}$Fe nuclide (Imshennik and Zabrodina 1999). Actually, this implies that we completely ignore the β processes and disregard the variety of iron-peak elements among the explosion products of a low-mass neutron star and in the surrounding iron gas. Clearly, only iron nuclei are available at $T<T_{\rm c}$; i.e., $X_{\rm Fe}=1$ and $X_{\rm He}=X_n=X_p=0$.

The term in the square brackets from (16) is the rest energy of the matter as a function of the mass fractions, which, obviously, becomes zero at $X_{\rm Fe}=1$. This means that the energy of pure iron is taken as

a zero level, being, of course, the lowest value of the above term.

Since the pressure and the specific internal energy must regularly be used in solving the system of hydrodynamic equations, it would be appropriate to use a tabulated equation of state. This would allow us to avoid complex calculations at each step of the solution of system (6)–(10) if the thermodynamic functions were calculated once and with a high accuracy. Our numerical method for solving the system of hydrodynamic equations (6)–(10) uses the density and specific internal energy as the main variables. Therefore, the equation of state is $P = f(\rho, \varepsilon)$. In the numerical method (see below), this equation is simulated by the so-called binomial equation of state

$$P = \left[(\bar{\gamma} - 1)\,\varepsilon + c_0^2\right]\rho - \rho_0 c_0^2. \qquad (22)$$

This simulation is local in nature. The constants $\bar{\gamma}$, c_0^2, and ρ_0 are determined by the pressure and its derivatives at a given point:

$$c_0^2 = \left(\frac{\partial f}{\partial \rho}\right)_\varepsilon - \frac{\varepsilon}{\rho}\left(\frac{\partial f}{\partial \varepsilon}\right)_\rho, \qquad (23)$$

$$\rho_0 c_0^2 = \rho\left(\frac{\partial f}{\partial \rho}\right)_\varepsilon - f, \quad \bar{\gamma} - 1 = \frac{1}{\rho}\left(\frac{\partial f}{\partial \varepsilon}\right)_\rho.$$

By directly substituting (23) into (22), it can be verified that the simulation of equation of state (22) with specified [according to (23)] constants satisfies the requirement that the pressure and the speed of sound derived from (22) be equal to those derived from the real equation of state $P = f(\rho, \varepsilon)$. Using the binomial approximation for the equation of state considerably simplifies the solution of the problem of discontinuity breakup, which underlies the numerical method. Thus, for the system of hydrodynamic equations to be numerically solved, we must know the pressure and its first derivatives with respect to density and specific internal energy as a function of these variables.

Equations (15)–(16) do not allow us to obtain P as a function of ρ and ε in explicit form. Therefore, it is necessary to first determine all of the thermodynamic quantities concerned as functions of density and temperature. To this end, we used an approach related to the Gaussian quadrature method (Krylov 1967). This approach has a sufficient accuracy over the entire range of densities and temperatures concerned (Blinnikov *et al.* 1996). To solve the system of hydrodynamic equations (6)–(10), we must also know the first derivatives of the pressure with respect to density ρ and specific internal energy ε. Using standard relations for the derivatives of thermodynamic quantities (Landau and Lifshitz 1976), we find the thermodynamic derivatives of the pressure needed for the numerical scheme to be implemented

$$\left(\frac{\partial P}{\partial \rho}\right)_\varepsilon = \left(\frac{\partial \tilde{P}}{\partial \rho}\right)_T - \frac{\left(\dfrac{\partial \tilde{P}}{\partial T}\right)_\rho}{\left(\dfrac{\partial \varepsilon}{\partial T}\right)_\rho}\left(\frac{\partial \varepsilon}{\partial \rho}\right)_T, \qquad (24)$$

$$\left(\frac{\partial P}{\partial \varepsilon}\right)_\rho = \frac{\left(\dfrac{\partial \tilde{P}}{\partial T}\right)_\rho}{\left(\dfrac{\partial \varepsilon}{\partial T}\right)_\rho},$$

where $\tilde{P}(\rho, T) = P(\rho, \varepsilon(\rho, T))$.

Finally, for the equation of state to be derived in final form, we must reinterpolate the computed tables of thermodynamic quantities and their derivatives, which depend on density and temperature, to the domain of the ρ and ε variations.

Clearly, using our equation of state, we can simulate the formation of a nucleon bubble within the computed region by artificially raising the temperature in the initial conditions compared to the temperature obtained by Boyes *et al.* (1999). In the above recalculations of the hydrostatic equilibrium conditions with the inevitable decrease in density on the simulation segments, we need not be concerned about the conservation of a purely nucleon composition, because the decrease in density only facilitates it.

THE NUMERICAL METHOD OF SOLUTION

The numerical solution of our problem is based on the popular and universal PPM method. This method uses the Eulerian finite-difference scheme (Colella and Woodward 1984) and is a modification of Godunov's method.

The numerical calculation was performed in spherical coordinates. To construct the finite-difference scheme, we rewrote the initial system of equations (6)–(10) in variables $\mathbf{U} = \{\rho, \rho V_r, \rho V_\theta, \rho V_\varphi, \rho E\}^T$:

$$\frac{\partial \mathbf{U}}{\partial t} + \frac{\partial (A_r \mathbf{F}_r(\mathbf{U}))}{\partial D_r} + \frac{\partial (A_\theta \mathbf{F}_\theta(\mathbf{U}))}{\partial D_\theta} + \frac{\partial \mathbf{G}}{\partial r} + \frac{\partial \mathbf{H}}{\partial \theta} = \mathbf{J},$$

$$\mathbf{F}_r(\mathbf{U}) = \begin{pmatrix} \rho V_r \\ \rho V_r^2 \\ \rho V_r V_\theta \\ \rho V_r V_\varphi \\ \rho V_r E + V_r P \end{pmatrix},$$

$$\mathbf{F}_\theta(\mathbf{U}) = \begin{pmatrix} \rho V_\theta \\ \rho V_\theta V_r \\ \rho V_\theta^2 \\ \rho V_\theta V_\varphi \\ \rho V_\theta E + V_\theta P \end{pmatrix}, \qquad (25)$$

$$\mathbf{G} = \begin{pmatrix} 0 \\ P \\ 0 \\ 0 \\ 0 \end{pmatrix}, \quad \mathbf{H} = \begin{pmatrix} 0 \\ 0 \\ P/r \\ 0 \\ 0 \end{pmatrix},$$

$$\mathbf{J} = \begin{pmatrix} 0 \\ \rho g_r + \rho(V_\theta^2 + V_\varphi^2)/r \\ \rho g_\theta + \rho(V_\varphi^2 \mathrm{cot}\theta - V_r V_\theta)/r \\ -\rho V_\varphi(V_r + V_\theta \mathrm{cot}\theta)/r \\ \rho(g_r V_r + g_\theta V_\theta) \end{pmatrix},$$

$$A_r = r^2, \quad D_r = \frac{r^3}{3},$$

$$A_\theta = \frac{\sin\theta}{r}, \quad D_\theta = -\cos\theta.$$

System (25) is hyperbolic; to solve it, we broke down the computed region into cells using a grid composed of surfaces of constant radius (r) and constant polar angle (θ). Next, we formally averaged the equations of system (25) over the cell volume ΔV_{ijk} and over the time step $\Delta t = t^{n+1} - t^n$. The problem of determining the distribution of the physical quantities $\{\rho, \rho V_r, \rho V_\theta, \rho V_\varphi, \rho E\}_{ij}$ at a later time t^{n+1} from their known distribution at a given time t^n is then reduced to determining the time-averaged fluxes at the cell boundaries and the time- and cell-volume-averaged free terms if, of course, the latter exist. To calculate the average fluxes, the interaction between two adjacent cells is considered as the problem of discontinuity breakup, whose solution is the main procedure of our numerical method. In general, an arbitrary discontinuity self-similarly breaks up into a configuration composed of four flow regions, which differ in properties and which are separated from one another by shock (or rarefaction) waves and a contact discontinuity (see, e.g., Landau and Lifshitz 1986; Kibel *et al.* 1963). In constructing the finite-difference scheme, we simulated the equation of state by the binomial formula (22). The use of this formula made it possible to properly describe strong rarefaction waves, which is of particular importance in astrophysical problems characterized by density variations over a wide range and by large density jumps. In this case, we can avoid numerically solving a system of ordinary differential equations and, without resorting to the formal replacement of rarefaction waves by shock waves (Colella and Glas 1985), can easily write out analytic formulas for shock and rarefaction waves. These formulas are required to construct an iterative process of calculating the pressure and velocity in the central region formed after a discontinuity breakup.

Godunov's method can be generalized to a multidimensional case (Godunov *et al.* 1976). However, the difficulty in determining the regions of influence for the problem of discontinuity breakup arises for our algorithm based on the Eulerian scheme. A possible solution of this problem is that several regions of influence, each corresponding to a certain characteristic (Riemann invariant), are found for the boundary between adjacent cells. The interpolation distributions of the physical quantities are averaged over all the derived regions of influence and the initial data for the problem of discontinuity breakup are obtained as the sums of these means with weighting coefficients proportional to the absolute values of the increments of the Riemann invariants along the corresponding directions. As a result, the characteristic properties of the system are properly taken into account (Dai and Woodward 1997). We use a parabolic interpolation for the physical quantities within a cell, which is monotonic and continuous at the cell boundaries in the region of smooth flow and conserves the total volume integrals for the quantities being interpolated (Colella and Woodward 1984). The constructed scheme is explicit; there is a restriction on the time step, the Courant condition, to maintain the stability of the calculation. In addition, the method does not require a special choice of artificial viscosity for each specific calculation. A finite-difference discrete approximation of the functions that describe the fields of the physical quantities automatically smears and smoothes out the discontinuities.

Below, we also give the system of units used in our calculations. The scales of the physical quantities in this system are

$$[r] = R_0, \quad [V_r] = [V_\theta] = [V_\varphi] = (GM_0/R_0)^{1/2}, \qquad (26)$$

$$[\rho] = M_0/(4\pi R_0^3), \quad [t] = R_0^{3/2}/(GM_0)^{1/2},$$

$$[P] = GM_0^2/(4\pi R_0^4),$$

$$[E] = GM_0/R_0, \; [T] = (GM_0^2/(4\pi R_0^4 a_r))^{1/4},$$

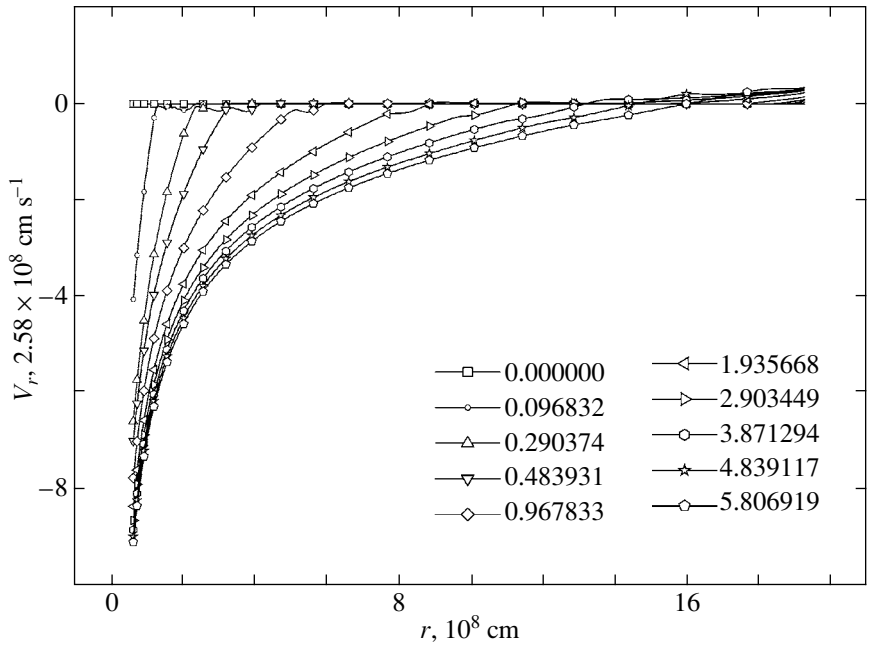

Fig. 1. The radial velocity component versus the radius at consecutive times (seconds) for data set [1].

where R_0 and M_0 are some length and mass scales. In units (26), the hydrodynamic equations with Newtonian gravitation contain no dimensionless parameters. It would be natural to use the following characteristic values from our problem as R_0 and M_0: $R_0 = 10^8$ cm and $M_0 = 10^{32}$ g. The numerical values for the scales of the physical quantities from (26) are then

$$[r] = 10^8 \text{ cm}, \tag{27}$$
$$[V_r] = [V_\theta] = [V_\varphi] = 2.583 \times 10^8 \text{ cm s}^{-1},$$
$$[\rho] = 7.958 \times 10^6 \text{ g cm}^{-3}, \quad [t] = 3.871 \times 10^{-1} \text{ s},$$
$$[P] = 5.310 \times 10^{23} \text{ erg cm}^{-3},$$
$$[E] = 6.674 \times 10^{16} \text{ erg}, \quad [T] = 2.894 \times 10^9 \text{ K}.$$

An efficient algorithm is used to solve the Poisson equation (5) and to determine the gravitational acceleration $\mathbf{g}$. This algorithm is convenient to use in the finite-difference scheme for integrating the hydrodynamic equations on a stationary grid in spherical coordinates (Aksenov 1999). The method is based on the expansion of the potential in integral representation,

$$\Phi = -G \int \frac{\rho(\mathbf{r}', t)}{|\mathbf{r}' - \mathbf{r}|} d\mathbf{r}', \tag{28}$$

by defining the Legendre polynomials in terms of the generating function. Using the addition theorem for associated Legendre polynomials, expression (28) can be reduced to a form convenient for averaging over the cell volume in spherical coordinates. This procedure can be used in problems with any number of measurements and it is efficient: it requires $\sim l_{\max}$ operations per cell, where $l_{\max}$ is the number of associated Legendre polynomials used in the calculation. In addition, the boundary condition $\Phi \to -GM/r$ for $r \to \infty$ is automatically satisfied for the potential.

NUMERICAL RESULTS

Let us turn to the results obtained when numerically integrating the system of hydrodynamic equations (6)–(10) with the initial data and boundary conditions given above. We performed two series of calculations: in the first series, we only took into account the effect of the decrease in the central gravitational mass due to the emission of a neutrino signal; in the second series, apart from allowance for this effect, we also analyzed the influence of hot nucleon bubbles that are presumably formed in the PNS corona.

In the first series of our calculations, we considered the following models of presupernova stars: [1] the total stellar mass $M_{\text{tot}} = 11M_\odot$, the iron-core mass (the mass of the central stellar region in which the mass fraction of iron-peak nuclei is more than 80%) $M_{\text{core}} = 1.266M_\odot$, the gravitational iron-core mass defect $\Delta M_G = 2.676 \times 10^{32}$ g, the mass of the matter inside the computed region $M_{\text{in}} = 0.627M_\odot$, the inner radius of the computed region $r_{\min} = 6.250 \times 10^7$ cm, its outer radius $r_{\max} = 1.937 \times 10^9$ cm, and the mass of the central region (up to the radius $r_{\min}$) $M_{\text{center}} = 0.9987M_\odot$; [2] $M_{\text{tot}} = 20M_\odot$, $M_{\text{core}} = 1.485M_\odot$, $\Delta M_G = 3.552 \times 10^{32}$ g, $M_{\text{in}} =$

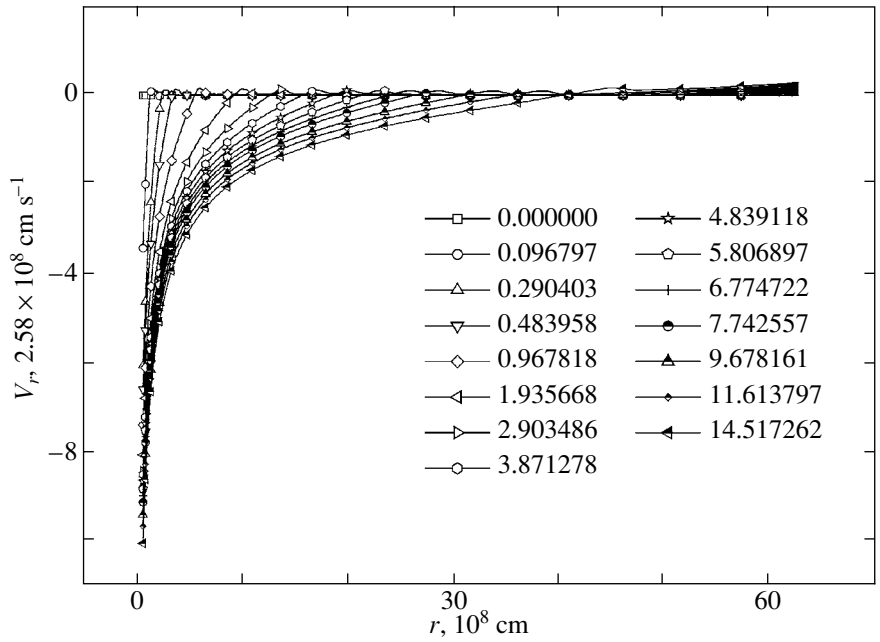

Fig. 2. Same as Fig. 1 for data set [2].

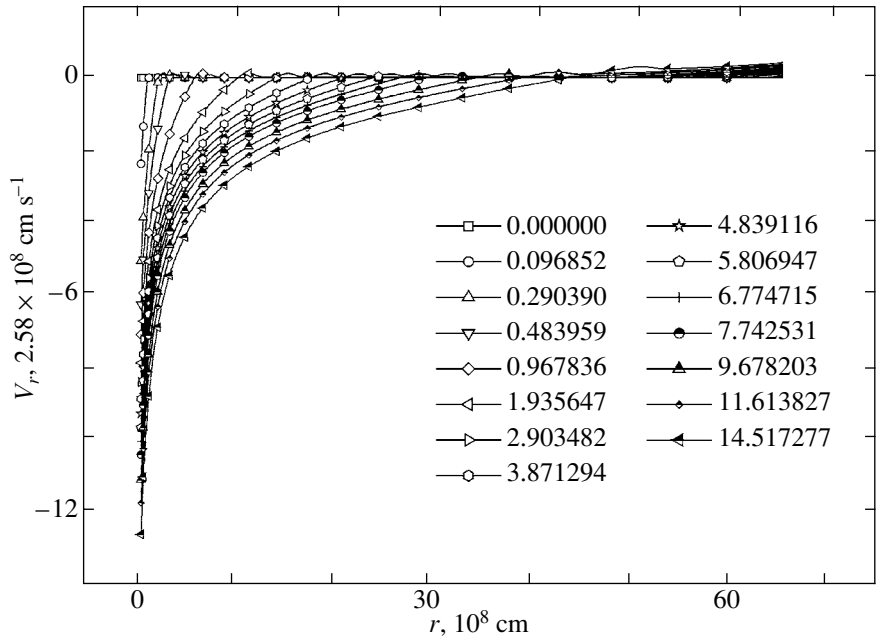

Fig. 3. Same as Fig. 1 for data set [3].

$2.825M_\odot$, $r_{\min} = 6.952 \times 10^7$ cm, $r_{\max} = 6.308 \times 10^9$ cm, and $M_{\text{center}} = 0.9992M_\odot$; [3] $M_{\text{tot}} = 25M_\odot$, $M_{\text{core}} = 1.620M_\odot$, $\Delta M_G = 4.386 \times 10^{32}$ g, $M_{\text{in}} = 5.458M_\odot$, $r_{\min} = 8.764 \times 10^7$ cm, $r_{\max} = 6.607 \times 10^9$ cm, and $M_{\text{center}} = 1.0001M_\odot$. In all of these calculations, we took the constant, relatively low specific internal energy $\varepsilon_{\text{b}} = 10^{16}$ erg g^{-1} and density $\rho_{\text{b}} = 500$ cm s^{-3} as the boundary condition at the outer (in radius) boundary $r_{\max}$ and assumed the radial velocity to be zero. A grid of 200 computed zones in radius was used in the numerical integration. An expansion in Legendre polynomials up to the number $l_{\max} = 20$ was used to solve the Poisson equation.

A similar flow pattern was observed in all of these cases. Figures 1–3 show plots of the radial veloc-

ity against the radius (profiles) at consecutive times. As we see from these figures, the matter inside the computed region in all calculations falls through the transparent inner boundary to the center under the effect of gravity in a regime resembling free fall. The neutrino signal, which causes the mass of the PNS located at the center to decrease, manifests itself only in the existence of a modest maximum in the radial-velocity profile. In calculations [2, 3] with more massive stars ($20M_\odot$ and $25M_\odot$), the velocity maximum emerges immediately ahead of the front of a strong rarefaction wave: the maximum radial velocity is positive but low; it does not exceed $\sim 2.8 \times 10^7$ cm s^{-1}. In calculation [1] with a low-mass star ($11M_\odot$), the maximum lies in the range of negative velocities, so there are no positive radial velocities along the entire profile. We also see from Figs. 1–3 that in each case, a zone of positive velocities appears near the outer boundary of the computed region. This fact can be explained in terms of the boundary condition at the outer radius, which simulates a vacuum. This boundary condition has no fundamental effect on the properties of the flow as a whole; it only gives rise to a weak rarefaction wave. The main conclusion drawn from all calculations [1]–[3] is that almost all of the matter inside the computed region is accreted onto the central PNS. The plots of the radial velocity against the mass coordinate (profiles) show that the point of zero velocity (the point of separation) moves along the mass coordinate outward during the entire calculation. This implies that if the outer stellar envelope is actually ejected, then the point of separation cannot be closer to the center than the inner boundary of the helium shell.

The second series of our calculations was devoted to the effect of hot nucleon bubbles, which are most likely formed in the PNS corona, on the behavior of the onionlike structure of a massive star after the onset of gravitational iron-core collapse. In the initial data of these calculations, a hot bubble was specified in the following artificial way: the temperature in several adjacent cells near the inner boundary of the computed region was raised compared to the surrounding matter to the extent that, according to the adopted equation of state, the mass fractions of iron and helium nuclei became zero. The distribution of the remaining thermodynamic quantities was constructed to satisfy the hydrostatic equilibrium conditions (11), (12) as before. All calculations were performed with the same model of a $25M_\odot$ star; only the mass of the hot nucleon gas in the bubble was varied. Since the problem was solved in the one-dimensional approximation, the region of hot nucleon gas was actually a spherical shell rather than a bubble. The system of hydrodynamic equations (6)–(10) was integrated with the following initial data: [4] the minimum bubble radius $r_{\min}^{\mathrm{NB}} = 8.901 \times 10^7$ cm, the maximum bubble radius $r_{\max}^{\mathrm{NB}} = 1.042 \times 10^8$ cm, the hot-gas mass $M_{\mathrm{NB}} = 0.396 \times 10^{-2} M_\odot$, and the mass of the matter inside the computed region $M_{\mathrm{in}} = 5.779 M_\odot$; [5] $r_{\min}^{\mathrm{NB}} = 8.901 \times 10^7$ cm, $r_{\max}^{\mathrm{NB}} = 1.248 \times 10^8$ cm, $M_{\mathrm{NB}} = 0.693 \times 10^{-2} M_\odot$, $M_{\mathrm{in}} = 5.858 M_\odot$; [6] $r_{\min}^{\mathrm{NB}} = 8.901 \times 10^7$ cm, $r_{\max}^{\mathrm{NB}} = 1.499 \times 10^8$ cm, $M_{\mathrm{NB}} = 0.996 \times 10^{-2} M_\odot$, and $M_{\mathrm{in}} = 6.036 M_\odot$. Calculation [7] differs from case [6] only in that a positive velocity, $V_{\mathrm{NB}} = 1.734 \times 10^9$ cm s^{-1}, equal in magnitude to the local free-fall velocity was assigned to the matter in the cells that fell within the region of hot gas. In calculations [4]–[7], the parameters of the computed region were taken to be identical: the total stellar mass $M_{\mathrm{tot}} = 25M_\odot$, the iron-core mass $M_{\mathrm{core}} = 1.620M_\odot$, the gravitational iron-core mass defect $\Delta M_G = 4.386 \times 10^{32}$ g, the inner radius of the computed region $r_{\min} = 8.764 \times 10^7$ cm, its outer radius $r_{\max} = 6.607 \times 10^9$ cm, and the mass of the central region $M_{\mathrm{center}} = 1.0001 M_\odot$. Thus, all of the latter parameters are identical to those in case [3].

In Figs. 4–7, the radial velocity is plotted against radius at consecutive times for cases [4]–[7], respectively. As we see from these figures, the shock wave produced through energy release in the nucleon bubble due to proton and neutron recombination into iron nuclei has an amplitude that is qualitatively proportional to the initial mass of the hot gas. In case [4], the shock wave is rather weak and the velocity of the post-shock matter barely reaches $\sim 3 \times 10^8$ cm s^{-1}. In this case, a strong rarefaction wave is formed at the inner boundary of the computed region, as in the calculations that only took into account the gravitational effect of neutrino radiation, and the matter begins to be accreted onto the gravitating center at a high rate. We see from Fig. 8 that almost all of the matter that was initially inside the computed region passes through the inner boundary, whereas the escape of the matter through the outer boundary is negligible and is entirely attributable to the artificial rarefaction wave produced by a fixed boundary condition. The time it took for the shock wave to reach the helium shell is ~ 13 s. In cases [6]–[7], the nucleon-gas mass is at a maximum ($\sim 0.01 M_\odot$). The appearance of a strong shock wave and envelope ejection were shown in both cases: the post-shock radial velocity is $\sim 1.1 \times 10^9$ and $\sim 1.5 \times 10^9$ cm s^{-1} for calculations [6] and [7], respectively. Therefore, the positive velocity ($\sim 1.7 \times 10^9$ cm s^{-1}) imparted to the hot gas of the nucleon bubble at the initial time in case [7] has a marginal effect on the envelope ejection. The rarefaction wave formed at the inner computed boundary is found to be much weaker than that in calculation [4]. As a result, the amount of matter accreted onto the center

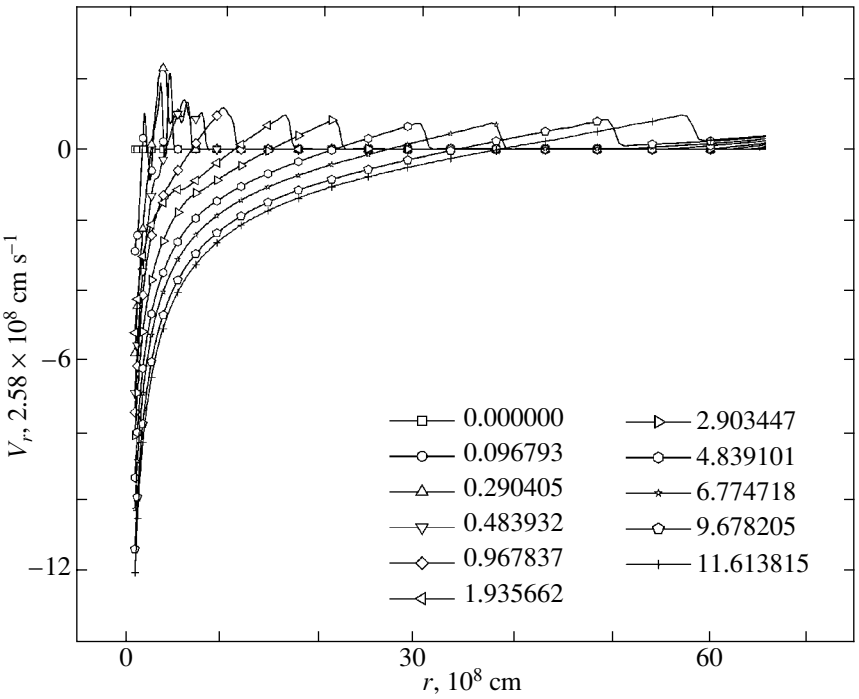

Fig. 4. Same as Fig. 1 for data set [4].

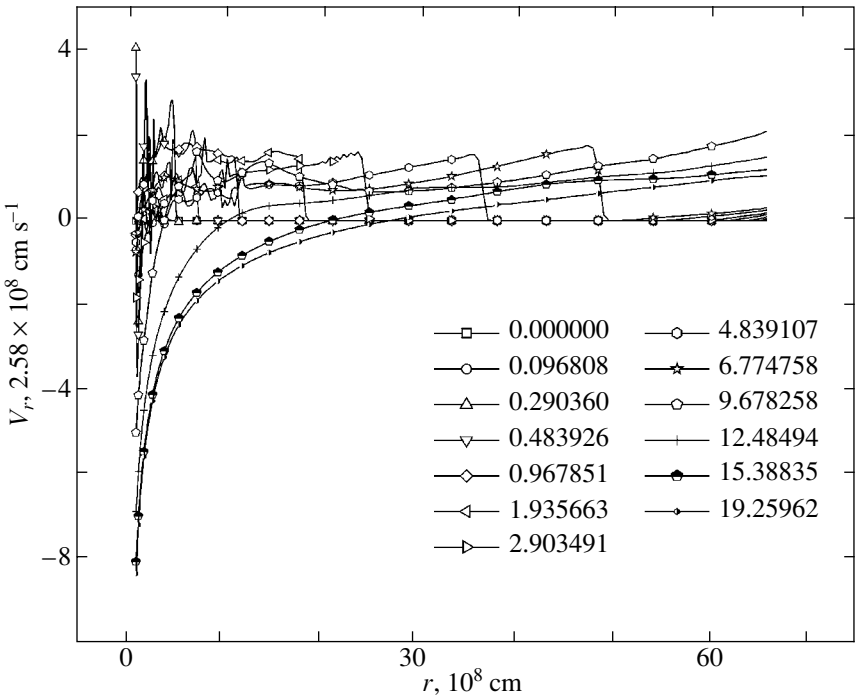

Fig. 5. Same as Fig. 1 for data set [5].

in these two calculations is modest: $\sim 0.045 M_\odot$ and $\sim 0.020 M_\odot$ for a zero and nonzero velocity of the hot gas, respectively. Almost all of the matter inside the computed region is ejected outward by the shock wave, as clearly confirmed by the plots in Figs. 9 and 10. In case [6], it took ~6 s for the shock wave to reach the helium shell and ~8 s for all of the matter to pass through the outer boundary; in case [7], both processes take about 4 s.

The calculation with the initial data [5] is interme-

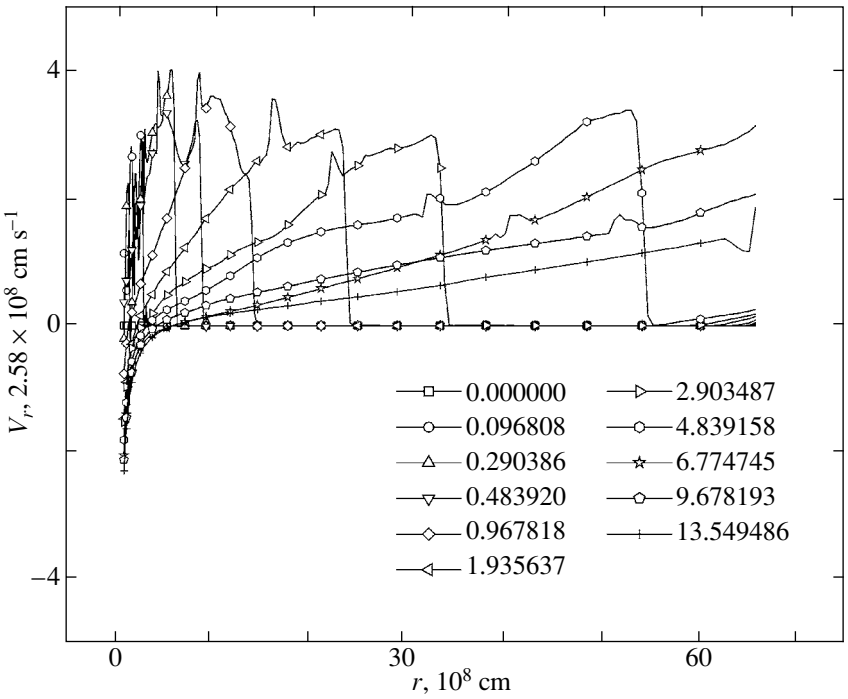

Fig. 6. Same as Fig. 1 for data set [6].

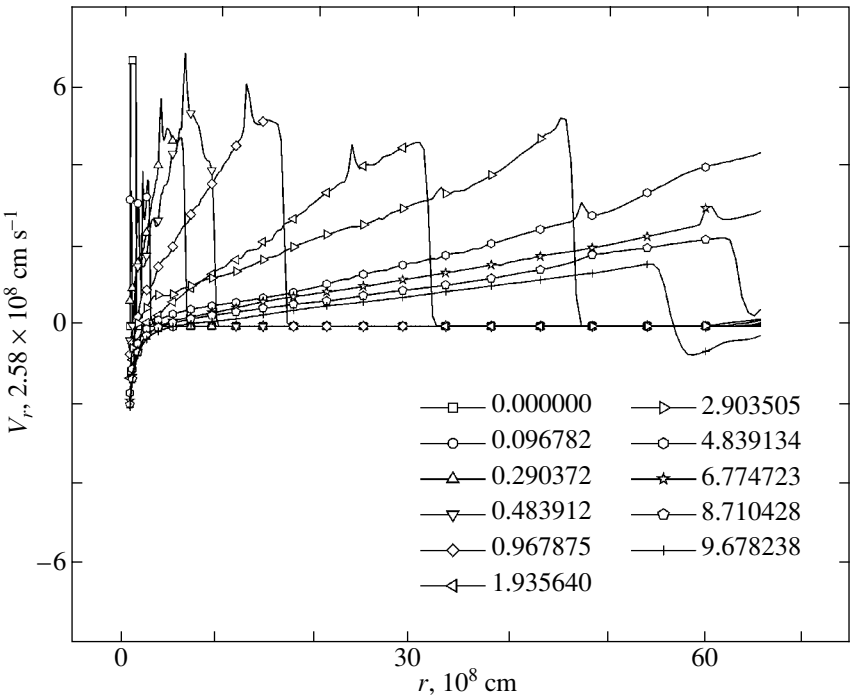

Fig. 7. Same as Fig. 1 for data set [7].

diate between case [4], on the one hand, and cases [6] and [7], on the other hand. A moderate rarefaction wave is formed near the inner boundary and the post-shock gas velocity is $\sim 5 \times 10^8$ cm s^{-1} (Fig. 5). The shock wave reaches the helium shell in $\sim$10 s. In this case, mass accretion at the inner computed boundary begins with an appreciable delay of $\sim$12 s and the matter flows outward from the center at a rate that is approximately twice the rate of the gas accretion onto the PNS (Fig. 11).

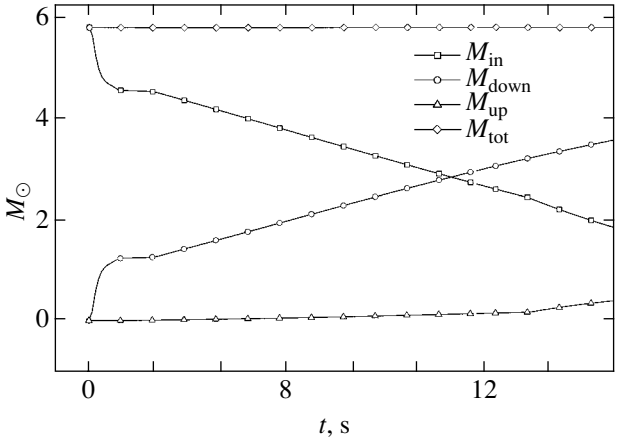

Fig. 8. Total mass fluxes through the outer and inner boundaries of the computed region versus time for the calculations with data set [4]; (M_{in} is the total mass of the matter inside the computed region, M_{down} is the total mass flux through the inner boundary, M_{up} is the total mass flux through the outer boundary, and $M_{tot} = M_{in} + M_{down} + M_{up}$ is the total mass of the matter.

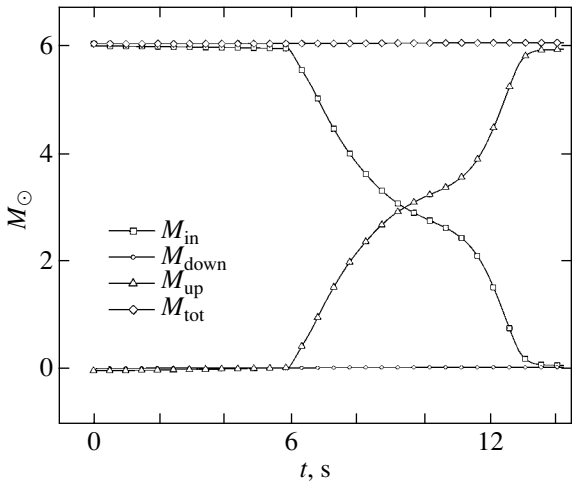

Fig. 9. Same as Fig. 8 for data set [6].

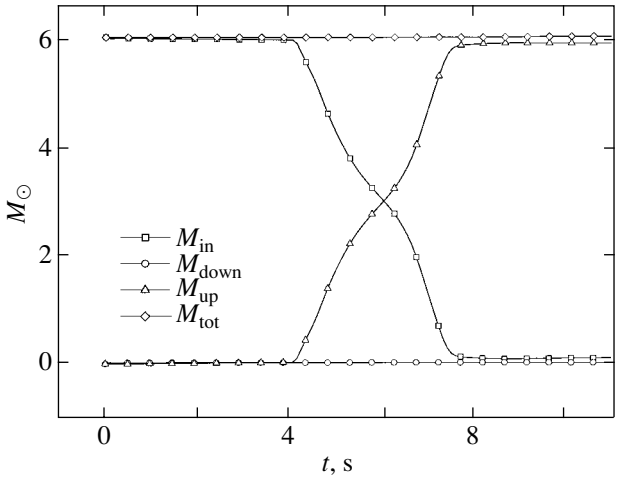

Fig. 10. Same as Fig. 8 for data set [7].

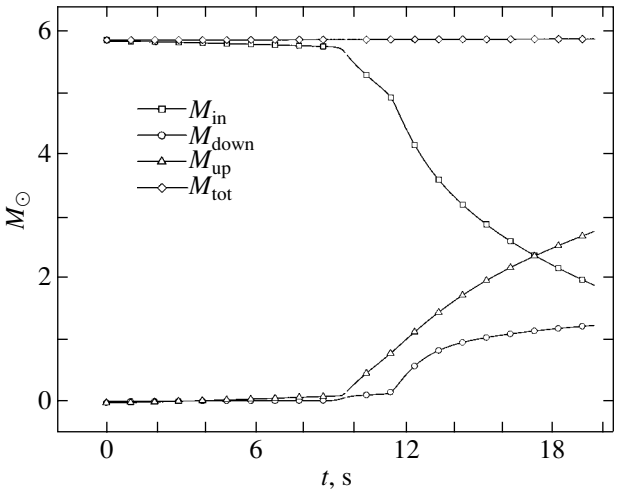

Fig. 11. Same as Fig. 8 for data set [5].

In cases [4]–[7], nucleons are recombined into iron nuclei rapidly and in approximately the same time for all cases of initial data, which does not exceed $\sim$1 s. For cases [4]–[7], we also calculated the kinetic energy flux through the outer boundary in radius $r_{\max}$. The following values were obtained for the total flux, which may prove to be of use in assessing the possibility of emersion of the outer stellar layers: [4] the total kinetic energy flux through the outer boundary by the completion of the calculation $E_{\text{kin out}} = 1.80 \times 10^{49}$ erg and the completion time of the calculation $t_{\text{end}} = 16.84$ s; [5]: $E_{\text{kin out}} = 3.87 \times 10^{50}$ erg and $t_{\text{end}} = 19.65$ s; [6]: $E_{\text{kin out}} = 2.23 \times 10^{51}$ erg and $t_{\text{end}} = 14.23$ s; [7]: $E_{\text{kin out}} = 5.46 \times 10^{51}$ erg and $t_{\text{end}} = 11.03$ s.

CONCLUSIONS

Of course, the conclusions regarding the ejection of the entire outer envelope of a massive star during the collapse of its iron core should have been reinforced by hydrodynamic calculations of the propagation of a strong shock wave through the helium shell and through the outer hydrogen–helium shell, certainly if they were preserved during the stellar evolution of this star. However, the velocity of the post-shock matter derived in the calculations with supercritical nucleon-bubble masses, which exceeds 10^9 cm s^{-1} for a radius of $\sim 6.6 \times 10^9$ cm, is, in turn, appreciably higher than the characteristic free-fall velocity with an inner mass of $6.8 M_\odot$ ($M =$

$M_{\rm in} + M_{\rm center} - \Delta M_G$), by more than a factor of 2 in case [6] $\left(v_{ff} = \left(\frac{2GM}{r_{\max}}\right)^{1/2} = 5.23 \times 10^8 \text{ cm/s}\right)$. The total outward kinetic energy flux through the outer boundary (see Sect. "Numerical Results") and the estimated recombination energy of the nucleon bubble simulated in the initial conditions of our problem suggest that complete ejection is possible. For the nucleon-bubble mass, we obtain $M_{\rm NB} = 0.996 \times 10^{-2} M_\odot$, so $E_{\rm NB} = M_{\rm NB} \times \frac{8.79 \text{ MeV}}{m_0} = 1.68 \times 10^{50}$ erg. This energy is close in absolute value to the gravitational energy of the outer stellar layers, $\sim 2.5 \times 10^{50}$ erg.

It should be particularly emphasized that our calculations yielded the critical nucleon-bubble mass $(M_{\rm NB})_{\rm crit} = M_{\rm NB}([5]) = 0.7 \times 10^{-2} M_\odot$ (see case [5]). It should be remembered that here, we deal with the most massive star with $M_{\rm MS} = 25 M_\odot$. For less massive stars, $(M_{\rm NB})_{\rm crit}$ is most likely much lower, although this suggestion needs to be verified by further calculations. Can such nucleon bubbles, which assist in the envelope ejection more than the other gravitational effect of energy losses in the form of a neutrino signal taken into account in our calculations, be formed? In the one-dimensional hydrodynamic theory of gravitational collapse (in many studies with an allowance made for neutrino radiation, including that at the neutrinosphere formation stage, which virtually coincides with the second collapse stage mentioned in the Introduction), a rather thick spherical shell has long been shown to appear above the neutrinosphere, which is semitransparent to neutrino radiation [see Imshennik and Nadyozhin (1982) for a review]. Burrows and Goshy (1993) showed that this shell has a quasi-steady-state structure in the typical case of a frozen accretion wave whose front represents the outer shell boundary. It is important that this shell is composed of a Boltzmann gas of free nucleons and electron–positron plasma. Imshennik (2002) refined such quasi-steady-state solutions and showed its strong convective instability virtually in the entire solution region that encompasses all the possible conditions for gravitational collapse or, to be more precise, its second stage (post-shock accretion). The typical masses in these shells called neutrino PNS coronas are $10^{-3} M_\odot < M_{\rm CPNS} < 10^{-2} M_\odot$; i.e., they are roughly equal to the critical mass $M_{\rm NB}$ derived above. The possibility of such nucleon bubbles being ejected due to the nonlinear development of convection is supported by the well-known considerations given by Burrows *et al.* (1994) based on their calculations of a two-dimensional model for gravitational collapse and by the interesting self-similar solutions of a neutrino wind that drags nucleon bunches into the outer stellar envelopes (Thompson *et al.* 2001). Here, we demonstrated the hydrodynamic effect of the ejection of the outer stellar envelope in the rough one-dimensional approximation. However, to reach the final conclusion regarding the ejection of the entire outer envelope, strictly speaking, requires further calculations of the passage of the shock wave obtained in our calculations through the helium shell and the outer hydrogen–helium shell. Still, it is qualitatively clear that a significant fraction of the kinetic energy accumulated behind the shock front will be spent on overcoming the gravitational binding energy of these outermost layers. For this reason, the resulting mean ejection velocities of the entire envelope can be much lower than the calculated velocities; i.e., the envelope will be essentially emersed rather than ejected.

ACKNOWLEDGMENTS

We wish to thank A.V. Zabrodin and his coworkers for valuable advice and help in developing the finite-difference method for solving the problem. We are also grateful to S.K. Godunov for attention given to this work. This study was supported by the Russian Foundation for Basic Research (project no. 00-15-96572) and the CRDF (grant no. MO-011-0).

REFERENCES

1. A. G. Aksenov, Pis'ma Astron. Zh. **25**, 226 (1999) [Astron. Lett. **25**, 185 (1999)].
2. S. I. Blinnikov, N. V. Dunina-Barkovskaya, and D. K. Nadyozhin, Astrophys. J., Suppl. Ser. **106**, 171 (1996).
3. H. Boyes, A. Heger, and S. Woosley, www.supersci.org (1999).
4. G. E. Brown, S. W. Bruenn, and J. S. Wheeler, Comments Astrophys. **16**, 153 (1992).
5. A. Burrows and J. Goshy, Astrophys. J. Lett. **416**, L75 (1993).
6. P. Colella and H. M. Glas, J. Comput. Phys. **59**, 264 (1985).
7. P. Colella and P. R. Woodward, J. Comput. Phys. **54**, 174 (1984).
8. W. Dai and P. R. Woodward, J. Comput. Phys. **134**, 261 (1997).
9. S. K. Godunov, A. V. Zabrodin, M. Ya. Ivanov, A. N. Kraĭko, and G. P. Prokopov, *Numerical Solution of Multidimensional Problems of Gas Dynamics* (Nauka, Moscow, 1976).
10. V. S. Imshennik, *Astrophysics on the Threshold of the 21st Centure,* Ed. by N. S. Kardashev (Gordon and Breach, Philadelphia, 1992), p. 167.
11. V. S. Imshennik, Yad. Fiz. **65** (11), (2002) (in press) [Phys. At. Nucl. **65** (11), (2002) (in press)].
12. V. S. Imshennik and E. A. Zabrodina, Pis'ma Astron. Zh. **25**, 123 (1999) [Astron. Lett. **25**, 93 (1999)].

13. V. S. Imshennik and D. K. Nadyozhin, Astron. Zh. **42**, 1154 (1965) [Sov. Astron. **9**, 896 (1965)].
14. V. S. Imshennik and D. K. Nadyozhin, Itogi Nauki Tekh., Ser. Astron. **21**, 63 (1982).
15. V. S. Imshennik and M. S. Popov, Pis'ma Astron. Zh. **27**, 101 (2001) [Astron. Lett. **27**, 81 (2001)].
16. V. S. Imshennik, S. S. Filippov, and A. M. Khokhlov, Pis'ma Astron. Zh. **7**, 219 (1981) [Sov. Astron. Lett. **7**, 121 (1981)].
17. I. A. Kibel, N. E. Kochin, and N. V. Roze, *Theoretical Hydrodynamics* (Fizmatgiz, Moscow, 1963).
18. V. I. Krylov, *Approximate Calculation of Integrals* (Nauka, Moscow, 1967; Macmillan, New York, 1962).
19. L. D. Landau and E. M. Lifshitz, *Course of Theoretical Physics,* Vol. 5: *Statistical Physics* (Nauka, Moscow, 1976; Pergamon, Oxford, 1980),
20. L. D. Landau and E. M. Lifshitz, *Course of Theoretical Physics,* Vol. 6: *Fluid Mechanics* (Nauka, Moscow, 1986; Pergamon, New York, 1987).
21. J. M. Lattimer and A. Yahil, Astrophys. J. **340**, 426 (1989).
22. D. K. Nadyozhin, Astrophys. Space Sci. **51**, 283 (1977).
23. D. K. Nadyozhin, Astrophys. Space Sci. **53**, 131 (1978).
24. D. K. Nadyozhin, Surv. High Energy Phys. **11**, 121 (1998).
25. T. A. Thompson, A. Burrows, and B. S. Meyer, Astrophys. J. **562**, 887 (2001).

Translated by V. Astakhov

Astronomy Letters, Vol. 28, No. 12, 2002, pp. 835–842. Translated from Pis'ma v Astronomicheskiĭ Zhurnal, Vol. 28, No. 12, 2002, pp. 928–935.

Analysis of HST Ultraviolet Spectra for T Tauri Stars: Estimating the Interstellar Extinction and the Contribution from an Accretion Shock to the Emission-Continuum Formation

A. S. Kravtsova* **and S. A. Lamzin**

Sternberg Astronomical Institute, Universitetskiĭ pr. 13, Moscow, 119992 Russia

Received June 28, 2002

Abstract—We analyzed the spectra of eight T Tauri stars (T Tau, RY Tau, CO Ori, EZ Ori, GW Ori, GX Ori, V1044 Ori, and SU Aur) in the wavelength range from 1200 to 3100 Å taken with the STIS spectrograph from the Hubble Space Telescope. For each star, we found an upper limit on the interstellar extinction A_V, which proved to be lower than the values obtained by different authors from optical observations. For T Tau and RY Tau, we found the upper limits on their luminosities, masses, and radii as well as the bolometric luminosity of the excess emission continuum. The latter is most likely associated with mass accretion from a protoplanetary disk. We show that the bulk of the emission continuum is radiated in the infrared. For these stars, we determined the ratio of the flux in the C IV 1550 doublet lines to the excess-continuum flux. This ratio proved to be two orders of magnitude lower than its values predicted by the accretion-shock (AS) models developed by Lamzin (1998) and Calvet and Gullbring (1998). This result leads us to believe that for T Tau and RY Tau, the emission continuum originates in the accretion disk and/or in the boundary layer rather than in the AS, as has been assumed previously. This implies that in these stars, only a small fraction of the accreted matter passes through the AS, while the bulk of this matter settles in the equatorial plane of the star, passing through the boundary layer.

Key words: *stars, T Tauri stars, disk accretion, stellar wind.*

INTRODUCTION

The T Tauri stars are young stars with masses $\leq 2M_\odot$ at the stage of contraction toward the main sequence. Their activity is currently believed to be due to mass accretion from a protoplanetary disk onto the central star with a large-scale magnetic field of strength $\sim 10^3$ G, which halts the disk at a distance of ~ 3–$5\,R_*$ from the stellar surface. Next, the matter falls to the star along magnetic field lines, accelerates to a velocity of ~ 300 km s^{-1}, and then decelerates in the shock wave. Thus, the line and continuum emission observed in classical T Tauri stars is assumed to be attributable to accretion-shock radiation [see Najita *et al.* (2000) and references therein].

Previously (Kravtsova and Lamzin 2002), we compared the observed spectral energy distribution of DR Tau at $\lambda \leq 2\ \mu$m with the flux in the C IV 1550 doublet lines and reached the following conclusion: although the activity of this star is attributable to disk accretion, less than 10% of all the accreted matter passes through the accretion shock, while the main flow of matter reaches the star through the disk that touches its surface. Since DR Tau is one of the most active young stars, the question arises as to whether the described situation is applicable to other T Tauri stars.

When estimating the parameters of young stars, it is necessary to correct the observed spectral energy distribution for interstellar extinction. This applies both to the parameters of the stars themselves (the luminosity, mass, and radius) and to the parameters that describe accretion (the accretion luminosity and accretion rate). Meanwhile, the value of A_V for young stars is determined from their optical spectra with a large error, because the photospheric spectra of T Tauri stars are distorted not only by interstellar extinction, but also through emission-continuum veiling.

The value of A_V can be independently determined by analyzing ultraviolet (UV) spectra based on the fact that the interstellar extinction curve has a local maximum near 2200 Å. Here, we estimate A_V from the UV spectra taken with the Hubble Space Telescope (HST) for eight young stars: T Tau, RY Tau, CO Ori, EZ Ori, GW Ori, GX Ori, V1044 Ori, and SU Aur. For two of them (T Tau and RY Tau), we

*E-mail: kravts@sai.msu.ru

1063-7737/02/2812-0835$22.00

Table 1. Information on the STIS observations

Star	Date (2000)	Spectrum code	$\Delta\lambda$, Å
RY Tau	Sep. 20	o5ex01010	1572–3156
		o5ex01020	1119–1715
T Tau	Feb. 7	o5ex05010	1119–1715
		o5ex05020	1572–3156
SU Aur	Feb. 13	o5ex02010	1119–1715
		o5ex02020	1119–1715
		o5ex02030	1572–3156
CO Ori	Feb. 25	o5ex03010	1119–1715
		o5ex03020	1119–1715
		o5ex03030	1572–3156
GW Ori	Feb. 22	o5ex04010	1119–1715
		o5ex04020	1119–1715
		o5ex04030	1572–3156
GX Ori	Feb. 20	o5ex06010	1572–3156
EZ Ori	Feb. 25	o5ex08010	1572–3156
		o5ex08020	1119–1715
V1044 Ori	Feb. 15	o5ex07010	1572–3156
		o5ex07020	1119–1715

study the relative contribution of the accretion shock to the formation of the emission-line spectrum.

OBSERVATIONAL DATA

The spectra of T Tau, RY Tau, CO Ori, EZ Ori, GW Ori, GX Ori, V1044 Ori, and SU Aur analyzed below were taken in 2000–2001 with the Space Telescope Imaging Spectrograph (STIS) in low-resolution mode (program ID 8317). These spectra were retrieved from the HST archival database (http://archive.stsci.edu/hst/target_descriptions.html). We reduced the spectra by means of the IRAF v2.11 (http://iraf.noao.edu/iraf) and STSDAS/TABLES v2.02 (http://ra.stsci.edu/STSDAS) software packages. The standard procedures described in Chapter 21 of the HST Data Handbook (http://www.stsci.edu/documents/data-handbook.html) were used; for calibration, we used the files recommended in the archival database. For each star, Table 1 gives the date of observations, the identification spectrum numbers in the archive, and the spectral range covered.

Table 2. Upper limits for A_V

Star	Sp	W(Hα)	A_V	A_V
T Tau	K0	60	0.6	1.7,[a] 1.46[e]
RY Tau	K1	20v	0.4	0.55[b]
GW Ori	G5	46	0.6	0.8[a]
CO Ori	F8	10v	0.4	2.2,[c] 1.08[d]
GX Ori	K1	28	0.2	0.43[d]
EZ Ori	G0	20	0.4	0.57,[b] 0.40[d]
V1044 Ori	G5	8.7	0.3	–
SU Aur	G2	4v	0.4	0.9,[a] 0.64[b]

Data sources: [a] Gullbring *et al.* (2000); [b] Skrutskie *et al.* (1996); [c] Gagne *et al.* (1995); [d] Cohen and Kuhi (1979); [e] White and Ghez (2001).

THE CONTINUUM ENERGY DISTRIBUTIONS OF THE STARS AND ESTIMATING THE INTERSTELLAR EXTINCTION A_V

We estimated the interstellar extinction A_V toward each of the eight stars under study using their observed continuum energy distributions. For each star, the continuum level F_λ^c was determined at several points using spectral regions with reliably identified absorption and emission lines. Therefore, F_λ^c was estimated accurately, at least in the region of interest near 2200 Å (see below). We drew a cubic spline through the set of $F_\lambda^c(\lambda)$ values and took the resulting curve as the continuum level.

Let us explain the procedure of determining A_V using T Tau as an example. Figure 1a shows the original spectrum of the star, and Fig. 1b shows its continuum energy distribution obtained by the method described above. Suppose that the wavelength dependence of the interstellar extinction A_λ is described by the so-called normal law with $R_V \equiv A_V/E(B-V) = 3.1$ (Seaton 1979). Correcting the original energy distribution for interstellar extinction with various A_V, we obtained a number of curves shown in Fig. 1c. We see that for $A_V \geq 0\overset{m}{.}6$, the curves exhibit a hump near 2200 Å, which would be natural to associate with the presence of a local maximum of the function $A_\lambda(\lambda)$ (Bless and Savage 1972). Since the true spectral energy distribution of T Tau is unknown, we restrict ourselves to the following assertion: if $A_\lambda(\lambda)$ toward this star corresponds to the normal law, then $A_V \leq 0\overset{m}{.}6$ for it.

The interstellar extinction law for several stars in Taurus is known to be anomalous, and R_V can reach 5 (Mathis 1990). Let us consider how strongly the form of $A_\lambda(\lambda)$ affects the estimate of A_V for the

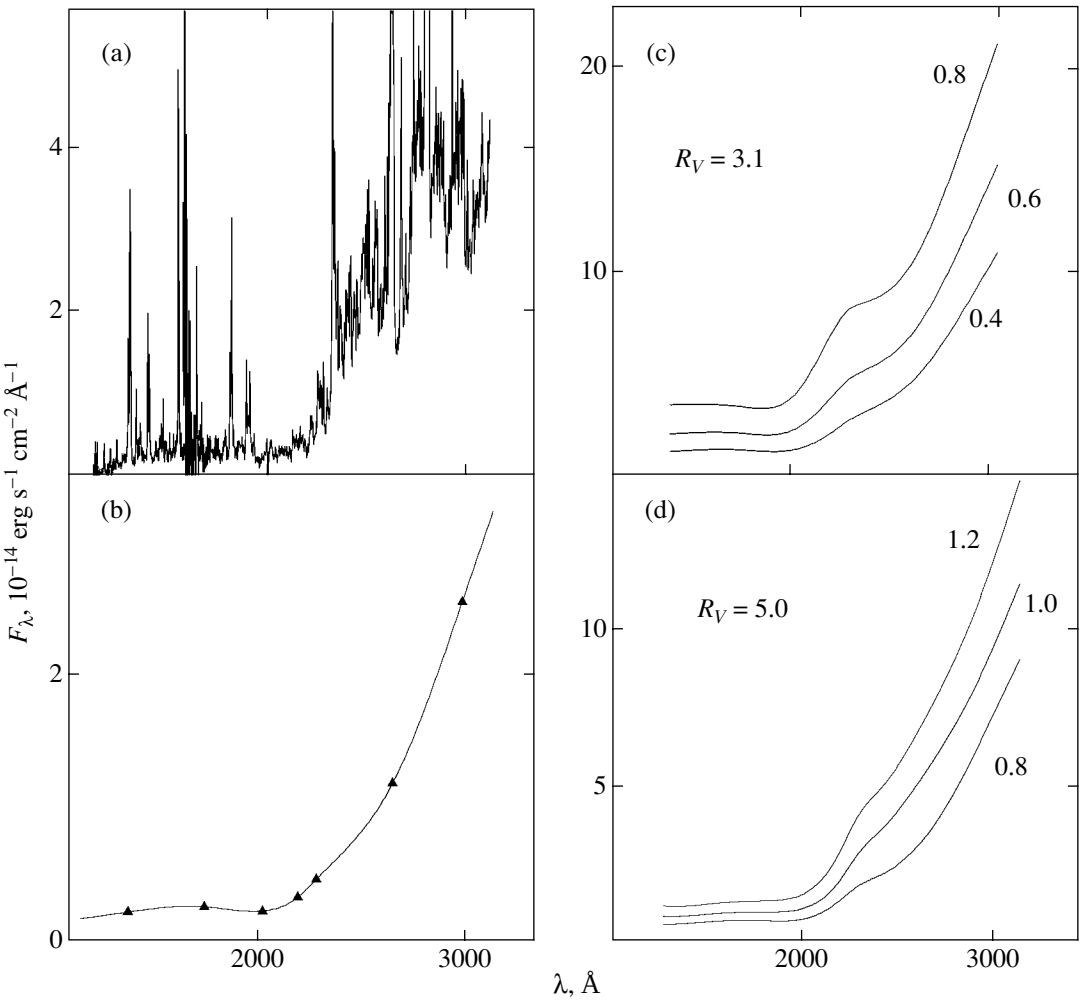

Fig. 1. The UV spectra of T Tau: the observed spectrum (a); the fit to the observed continuum (b); the continuum energy distribution corrected for interstellar extinction with various values of A_V, for $R_V = 3.1$ (c) and $R_V = 5$ (d).

stars under study. Figure 1d shows the curves corresponding to the spectral energy distribution of T Tau corrected for interstellar extinction with various A_V and $R_V = 5.0$; the corresponding dependence $A_\lambda(\lambda)$ was taken from Mathis (1990). We see that, in this case, the hump in the curves appears at $A_V \geq 0^m.8$. Thus, the lack of information on the interstellar extinction law results in an uncertainty in the upper limit on A_V of the order of $0^m.2$. Such an accuracy is sufficient for our purposes if we bear in mind that the value of A_V derived for T Tau from optical spectra is $1^m.46$ (White and Ghez 2001) or even $1^m.7$ (Gullbring *et al.* 2000).

For the remaining seven stars under study, we corrected the spectral energy distributions for interstellar extinction using only the standard extinction law with $R_V = 3.1$. Figure 2 shows the original spectrum for each star along with the observed and extinction-corrected (with various A_V) continuum energy distributions. The upper limits on A_V derived from these curves are given in Table 2 for each of the stars. In addition, the table gives the spectral types of the stars and the Hα-line equivalent widths from the catalog by Herbig and Bell (1988), as well as the A_V estimates obtained by different authors from optical observations.

It follows from the table that our upper limits for A_V are lower than the values derived from optical observations, with the discrepancy being particularly large for CO Ori and T Tau. We may assume that because of the difficulties noted in the Introduction, the values of A_V determined from optical observations were significantly overestimated. However, we cannot rule out an alternative explanation of the discrepancy found. Our method for determining A_V is based on the presence of a local maximum in the $A_\lambda(\lambda)$ curve, which is probably attributable to the smallest interstellar dust grains (Kaplan and Pikel'ner 1979). Additional extinction may arise inside a star-forming region, in which, for one reason or another, there

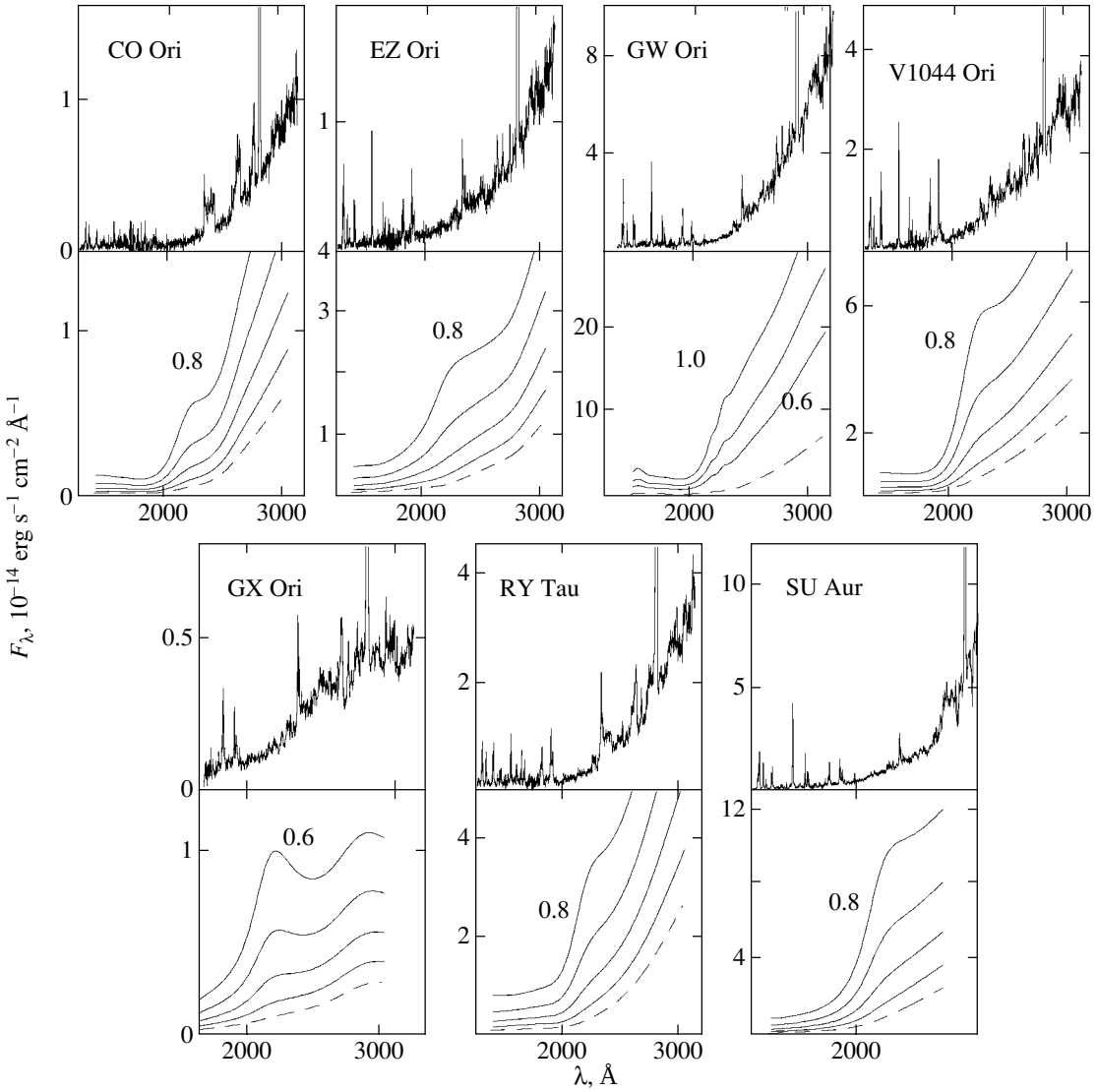

Fig. 2. The UV spectra of the stars under study: the upper panel shows the observed spectrum, and the lower panel shows the observed continuum energy distribution (dashed line) and the continuum energy distribution corrected for interstellar extinction with $R_V = 3.1$ and various A_V (solid lines). The values of A_V for two adjacent curves differ by $0^m.2$.

are no small dust grains [see the review article by Bertout (1989)]. Special studies beyond the scope of this study are required to elucidate how realistic this hypothesis is.

ESTIMATING THE CONTRIBUTION OF THE FLUX IN THE C IV 1550 DOUBLET LINES TO THE TOTAL LUMINOSITY

An accretion shock is generally believed to be the main source of excess continuum in young stars (Calvet and Gullbring 1998). The C IV 1550 doublet lines, which are the most intense emission lines in the UV spectra of young stars, are also formed in the accretion shock. It follows from calculations that, if all of the excess continuum originates in the accretion shock, then the ratio ξ of the luminosity in the doublet lines to the emission-continuum luminosity must be no less than 0.05 (Lamzin 1998). It can be shown that a similar conclusion also follows from the calculations of Calvet and Gullbring (1998). However, we found this ratio to be much smaller for DR Tau (Kravtsova and Lamzin 2002). As a result, the accretion rate derived from the luminosity in the C IV 1550 lines

Table 3. UV fluxes

Star	$F_{-13}^{\mathrm{C\,IV}}$	$F_{-11}^{c,UV}$	$F_{\mathrm{C\,IV}}/F_c^{UV}$
T Tau	7.5	5.5	0.013
RY Tau	1.7	3.3	0.0052

proved to be three orders of magnitude lower than the accretion rate $\dot{M}_{ac}$ determined from the bolometric emission-continuum luminosity.

Since the photospheres of F- and G-type stars radiate considerable energy in the wavelength range from 2000 to 3000 Å, the fraction of the UV flux due to accretion is difficult to determine for these stars. For this reason, we chose K-type stars to estimate ξ: T Tau (K0) and RY Tau (K1). GX Ori is also of the K0 type, but it has no spectra in the 1550 Å range.

For T Tau and RY Tau, we determined the fluxes in the C IV 1550 lines, F_{CIV}, and in the UV continuum, F_c^{UV}, to be more precise, at $\lambda \leq 3000$ Å. These fluxes corrected for interstellar extinction (see Table 1) are given in Table 3 in units of 10^{-13} erg s^{-1} cm^{-2} for F_{CIV} and 10^{-11} erg s^{-1} cm^{-2} for F_c^{UV}. The last column gives the F_{CIV}/F_c^{UV} ratio, which proved to be lower than the theoretical value of 0.05 for both stars. Note that this ratio weakly depends on A_V and R_V: in particular, if we take $A_V = 1^m.0$ and $R_V = 5.0$ for T Tau, then the ratio will be virtually the same.

Since the theory deals with the bolometric emission-continuum luminosity, ξ must be lower than the derived ratio. To ascertain how much lower it is, we attempted to estimate the continuum bolometric flux. For this purpose, we used the mean U, B, V, R_c, I_c, J, H, and K brightnesses of T Tau and RY Tau (Kenyon and Hartmann 1995) supplemented with our UV data.

Let us initially consider the situation with T Tau, whose spectral energy distribution is shown in Fig. 3a for $A_V = 0^m.6$ and $R_V = 3.1$. But first we make two remarks. First, T Tau is a triple system consisting of the optical component T Tau N and the binary system T Tau S offset by $0''.7$ from it. According to Duchene *et al.* (2002), the contribution from T Tau S to the total light is negligible at $\lambda < 2.5$ μm, so our analysis applies solely to T Tau N. Second, our flux F_{CIV} is approximately half the mean flux obtained from IUE observations (Gómez de Castro and Franqueira 1997). However, this does not imply that the UV-continuum flux during the observations was also half the mean flux, because, in general, the emission-line and continuum fluxes do not correlate for T Tauri stars (Johns-Krull and Valenti 2001). But this uncertainty is of no particular importance, because, as we will see below, a comparatively small fraction of the total energy is emitted in the UV.

Figure 3a also shows the curve that describes the spectral energy distribution of a K0 subgiant taken from Pickles (1998). It is inscribed in the curve that represents the observed (mean) spectral energy distribution of T Tau and, hence, may be considered as an upper limit for the photospheric radiation from T Tau N. We can now estimate an upper limit on the total flux from the photosphere of T Tau N and the bolometric emission-continuum flux F_c^{bol}. Assuming the distance to the two stars to be equal to the mean distance of the Tau–Aur star-forming region, 140 pc (Elias 1978), we found upper limits on the bolometric luminosity of T Tau N, L_*, and on the emission-continuum luminosity, L_c. Their values, in $L_\odot$, are given in Table 4.

We see from Fig. 3a that the bulk of the continuum radiation is emitted in the near infrared, suggesting that the F_c^{bol} estimate weakly depends on the uncertainty in A_V. To verify this, we constructed the spectral energy distribution of T Tau for $A_V = 1.46$ (White and Ghez 2001) and $R_V = 3.1$ in Fig. 3b. Although the contribution of the star itself to the total energy in this case became slightly larger (80% instead of 50% for $A_V = 0.6$), the luminosity of the veiling continuum changed only slightly. Similar calculations for $A_V = 1^m.0$ and $R_V = 5.0$ indicate that the final result also changes little in this case (see Table 4).

Changes in A_V affect the luminosity in the C IV 1550 doublet lines and, hence, ξ to a much greater extent. However, we see from Table 4 that in both cases, the value of ξ (in units of 10^{-4}) is almost two orders of magnitude lower than its theoretically predicted value (0.05). The same low value is obtained for $A_V = 1.46$ (White and Ghez 2001) and $R_V = 3.1$.

It may be assumed that the infrared excesses in T Tau and RY Tau are, to some extent, attributable to the radiation from as yet undetected cool companions. Recall, however, that even in the UV, the ratio of the fluxes in the C IV 1550 doublet lines and in the continuum is appreciably lower than its theoretical value. Therefore, although the presence of infrared companions would increase ξ, it would still be several times lower than its theoretically predicted value.

The stars CO Ori, EZ Ori, GW Ori, V1044 Ori, and SU Aur also exhibit substantial infrared excesses, but the UV emission-continuum luminosity cannot be easily estimated for them (see above). In addition, we cannot rule out the possibility that the infrared excesses in these stars are entirely attributable to cool companions. For this reason, we did not estimate ξ and other parameters for them.

According to Cohen and Kuhi (1979), the effective temperature of K0 stars is 5240 K. This allows us to determine an upper limit on the radius of T Tau N and, using evolutionary tracks from D'Antona and Mazzitelli (1994), an upper limit on its mass. Their values are listed in Table 4 in units of $R_\odot$ and $M_\odot$, respectively.

Figure 3c shows the mean spectral energy distribution of RY Tau constructed from the data of

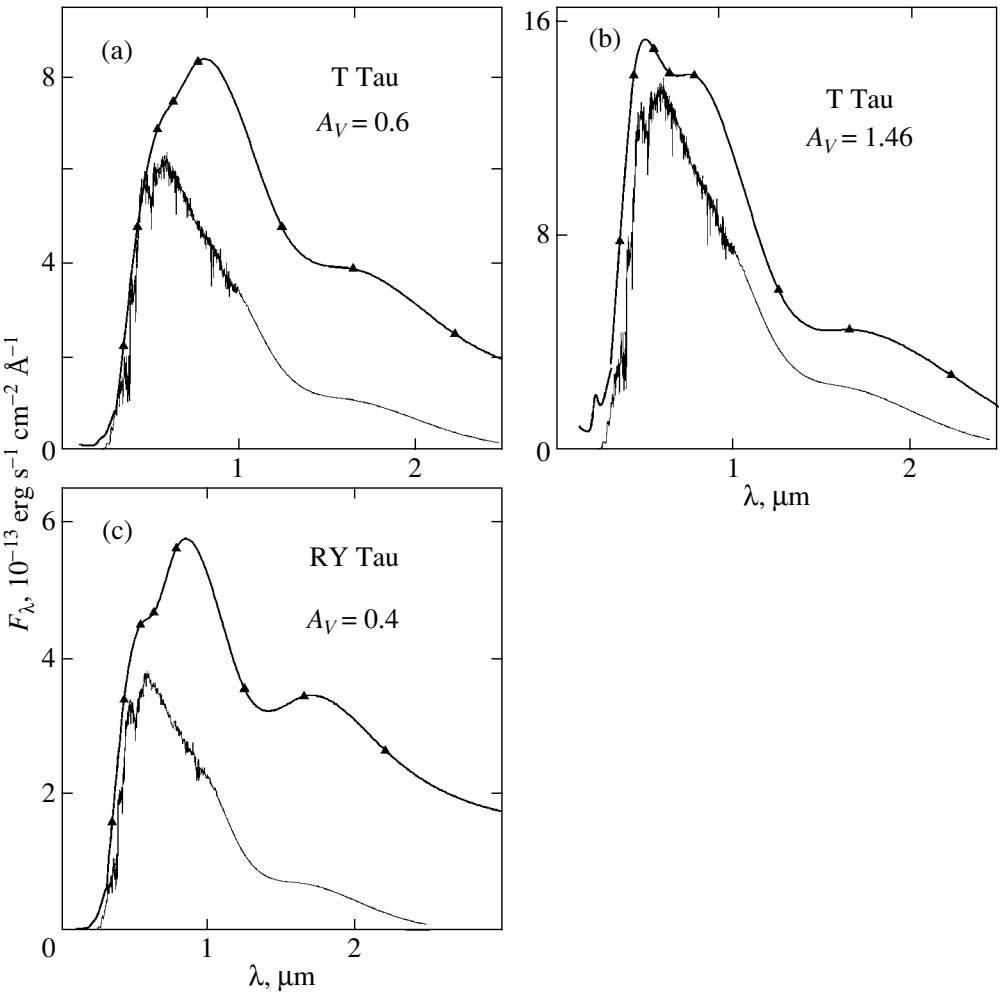

Fig. 3. The spectral energy distributions of T Tau and RY Tau corrected for interstellar extinction with $R_V = 3.1$ and $A_V = 0^m.6$ (a), $A_V = 1^m.46$ (b), and $A_V = 0^m.4$ (c). (a, b) The thin line indicates the spectral energy distribution of a K0 subgiant for T Tau and (c) a K1 subgiant for RY Tau.

Kenyon and Hartmann (1995), in which we inscribed the spectrum of a K1 subgiant (Pickles 1998). We see that, as with T Tau, the main excess is observed in the infrared. Having determined all parameters of the star using the same technique, we found ξ to also be abnormally low for RY Tau (see Table 4).

It thus follows that the C IV 1550 doublet lines and the emission continuum cannot simultaneously originate in the accretion shock [for details, see Kravtsova and Lamzin (2002)]. Therefore, we think that the following two suggestions previously made for DR Tau are valid for T Tau and RY Tau.

(1) The emission continuum of these stars originates mainly in the accretion disk and/or in the boundary layer. Since the accretion energy in our case is almost completely emitted in the continuum, we can determine the accretion rate from the relation $L_c = \dot{M}_{\rm ac} G M_*/R_*$. The inferred values are given in Table 4 in units of $10^{-7} M_\odot$ yr^{-1}.

(2) Only a small fraction of the matter falling to the star passes through the accretion shock, whereas the bulk of it settles in the equatorial plane of the star, passing through the boundary layer.

We see from Fig. 1 that the continuum of T Tau at $\lambda \leq 1700$ Å has an almost constant intensity. The situation for RY Tau is similar (see Fig. 2). It could be assumed that the "flat" short-wavelength continuum is related to the accretion-shock radiation. However, the continuum intensity is very low in this range and we are not completely sure that we correctly determined its level.

Herbst *et al.* (1986) detected periodic brightness variations in T Tau with a period of $\simeq 2^d.8$. These brightness variations are generally believed to be due to the rotational modulation of a hot spot on the stellar surface produced by the accretion shock. The broadening of photospheric lines in T Tau N due to its axial rotation is $v \sin i \simeq 20$ km s^{-1} (Hartmann

Table 4. Parameters of the stars

Star	R_V	A_V	$L_{\rm bol}$	L_*	L_c	$\xi, 10^{-4}$	R_*	M_*	$\dot{M}, 10^{-7}$	i
T Tau	3.1	0.6	5.3	2.6	2.7	2	2.0	1.8	1.3	35
	3.1	1.46	8.6	6.9	1.7	5	3.2	2.1	0.85	20
	5.0	1.0	6.7	3.5	3.2	1	2.2	1.8	1.6	30
RY Tau	3.1	0.4	8.0	1.6	6.4	0.2	1.6	1.7	1.9	–

et al. 1986). Using these data and our values of the stellar radius, we calculated the angle i between the rotation axis of the star and the line of sight or, to be more precise, a lower limit on this quantity given in Table 4 (in degrees). If we determined A_V correctly, then the angle i is appreciably larger than that assumed previously. This conclusion can be verified by observations of the T Tau disk with the VLTI interferometer.

At the same time, since the energy emitted in the accretion shock is approximately a factor of 100 lower than that assumed previously, the following question arises: whether the hot spot responsible for the periodic brightness variations in T Tau N is actually located on the stellar surface. If not, then the above estimate of the angle i is meaningless.

CONCLUSIONS

Our analysis of the UV spectra for eight classical T Tauri stars (T Tau, RY Tau, CO Ori, EZ Ori, GW Ori, GX Ori, V1044 Ori, and SU Aur) has yielded upper limits on the interstellar extinction A_V. The derived values are appreciably lower than the published A_V determined for these stars from optical observations.

This fact may be indicative of additional extinction toward stars within star-forming regions. The extinction law $A_\lambda(\lambda)$ in these regions must then significantly differ from the standard law, at least near 2200 Å. If there is no additional extinction, then the mass, radius, and luminosity taken up until now for T Tau and RY Tau were overestimated. Our upper limits for these quantities are given in Table 4.

For T Tau and RY Tau, we found that the ratio of the flux in the C IV 1550 doublet lines to the bolometric emission-continuum flux (ξ in Table 4) is lower than its theoretically predicted value approximately by two orders of magnitude. Therefore, we believe the following two suggestions to be valid for these two stars:

(1) the emission continuum of these stars originates mainly in the accretion disk and/or in the boundary layer; and

(2) only a small fraction of the matter falling to the star passes through the accretion shock, whereas the bulk of it settles in the equatorial plane of the star, passing through the boundary layer.

Since we previously reached similar conclusions for DR Tau (Kravtsova and Lamzin 2002), there is reason to suspect that the role of accretion-shock radiation in forming the emission-line spectra of classical T Tauri stars is much less than is generally believed.

REFERENCES

1. C. Bertout, Ann. Rev. Astron. Astrophys. **27**, 351 (1989).
2. R. C. Bless and B. D. Savage, Astrophys. J. **171**, 293 (1972).
3. N. Calvet and E. Gullbring, Astrophys. J. **509**, 802 (1998).
4. M. Cohen and L. V. Kuhi, Astrophys. J., Suppl. Ser. **41**, 743 (1979).
5. F. D'Antona and I. Mazzitelli, Astrophys. J., Suppl. Ser. **90**, 467 (1994).
6. G. Duchene, A. M. Ghez, and C. McCabe, Astrophys. J. (2002) (in press).
7. J. H. Elias, Astrophys. J. **224**, 857 (1978).
8. M. Gagne, J.-P. Caillault, and J. R. Stauffer, Astrophys. J. **445**, 280 (1995).
9. A. I. Gómez de Castro and M. Franqueira, ESA SP-1205 (Noordwijk, The Neetherlands, 1997).
10. E. Gullbring, N. Calvet, J. Muzerolle, and L. Hartmann, Astrophys. J. **544**, 927 (2000).
11. L. Hartmann, R. Hewett, S. Stahler, and R. Mathieu, Astrophys. J. **309**, 275 (1986).
12. G. H. Herbig and K. R. Bell, Lick Obs. Bull. **1111** (1988).
13. W. Herbst, J. F. Booth, P. F. Chugainov, *et al.*, Astrophys. J. Lett. **310**, L71 (1986).
14. C. M. Johns-Krull and J. A. Valenti, Astrophys. J. **561**, 1060 (2001).
15. S. A. Kaplan and S. B. Pikel'ner, *The Interstellar Medium* (Nauka, Moscow, 1979; Harvard Univ. Press, Cambridge, 1970).
16. S. J. Kenyon and L. Hartmann, Astrophys. J., Suppl. Ser. **101**, 117 (1995).
17. A. S. Kravtsova and S. A. Lamzin, Pis'ma Astron. Zh. (2002) (in press) [Astron. Lett. (2002) (in press)].

18. S. A. Lamzin, Astron. Zh. **75**, 367 (1998) [Astron. Rep. **42**, 322 (1998)].
19. J. S. Mathis, Ann. Rev. Astron. Astrophys. **28**, 37 (1990).
20. J. Najita, S. Edwards, G. Basri, and J. Carr, in *Protostars and Planets IV,* Ed. by V. Mannings, A. P. Boss, and S. S. Russell (University of Arizona Press, Tucson, 2000), p. 457.
21. A. J. Pickles, Publ. Astron. Soc. Pac. **110**, 863 (1998).
22. M. J. Seaton, Mon. Not. R. Astron. Soc. **187**, 75p (1979).
23. M. F. Skrutskie, M. R. Meyer, D. Whalen, and C. Hamilton, Astron. J. **112**, 2168 (1996).
24. R. J. White and A. M. Ghez, Astrophys. J. **556**, 265 (2001).

Translated by N. Samus'

Astronomy Letters, Vol. 28, No. 12, 2002, pp. 843–846. Translated from Pis'ma v Astronomicheskiĭ Zhurnal, Vol. 28, No. 12, 2002, pp. 936–939.

A Preliminary Radial-Velocity Curve for the Star θ^1 Ori D

É. A. Vitrichenko*

Space Research Institute, Russian Academy of Sciences, ul. Profsoyuznaya 84/32, Moscow, 117810 Russia

Received June 27, 2002

Abstract—We measured the radial velocity of the star θ^1 Ori D from IUE spectra and used published observations. Based on these data, we determined the period of its radial-velocity variations, $P = 20.2675 \pm 0.0010$ days, constructed the phase radial-velocity curve, and solved it by least squares. The spectroscopic orbital elements were found to be the following: the epoch of periastron passage Ep = JD 2430826.6 ± 0.1, the system's center-of-mass velocity $\gamma = 32.4 \pm 1.0$ km s^{-1}, $K = 14.3 \pm 1.5$ km s^{-1}, $\omega = 3.3 \pm 0.1$ rad, $e = 0.68 \pm 0.09$, $a_1 \sin i = 3 \times 10^6$ km, and $f_1 = 0.0025 M_\odot$. Twice the period, $P = 40.528 \pm 0.002$ days, is also consistent with the observations. © *2002 MAIK "Nauka/Interperiodica"*.

Key words: *stars—properties, classification.*

INTRODUCTION

The star θ^1 Ori D (=HD 37023) is a member of the Orion Trapezium and lies to the east of the other stars. Its brightness is believed to be constant and it was commonly used as a comparison star when studying the Trapezium stars.

Based on an excessively large spread in its radial velocities (~50 km s^{-1}), Plaskett and Pearce (1931) were the first to detect the star's spectroscopic binarity. However, they failed to find any period.

The objective of this study was to collect all published radial-velocity measurements, perform new observations, and attempt to determine the period of the radial-velocity variations by analyzing these data.

OBSERVATIONAL DATA

Table 1 provides information on the radial-velocity observations. The first and second columns give references and the number of measured spectra, respectively; the next columns give the measurement errors of the radial velocity and the number N of measured lines. A total of 68 spectra were measured. The last row in Table 1 contains information on our measurements. These measurements were carried out by using IUE archival spectra. The last two are explaned below.

The spectra that we measured are listed in Table 2. The first column gives the IUE spectrum numbers. All of the spectra were taken with the SWP camera with a high dispersion and a small aperture. Low-quality spectra are marked by a colon. The second column list midexposure Julian dates. The last two columns contain the measured radial velocities and the number of lines used. The measurement error, in the units of the last figure, is given in parentheses next to the radial velocity. We used only Fe IV lines for our radial-velocity measurements, because they were numerous and were not blended with interstellar and circumstellar lines (Vitrichenko 2002).

ANALYSIS OF THE RADIAL-VELOCITY MEASUREMENTS

An examination of Table 1 shows that the measurements by different authors significantly differ in accuracy. The entire set of measurements can be divided into two accuracy groups: high- and medium-accuracy observations. We place the observations by Struve and Titus (1944) and our observations into the first group and all of the remaining observations into the second group. We exclude the observations by Ismailov (1988) from our analysis, because they are outliers.

Different authors used different techniques to determine the radial velocity; hence the difference in random and systematic errors. For example, Abt *et al.* (1991) measured only hydrogen lines. The system possesses a stellar wind that produces additional absorption in the short-wavelength wings of the hydrogen lines. This results in a systematic error that shows up in the measurements by Plaskett and Pearce (1931) and by Morell and Levato (1991). These authors also measured hydrogen lines. The large hydrogen-line width also causes the random error to increase.

*E-mail: vitrich@nserv.iki.rssi.ru

1063-7737/02/2812-0843$22.00

Table 1. Sources of radial-velocity observations

Reference	Number of spectra	σ_1, km s^{-1}	N	Δ, km s^{-1}	σ_2, km s^{-1}
Plaskett and Pearce (1931)	6	10	11	−3	11
Struve and Titus (1944)	18	4	6–7	0	4
Ismailov (1988)	5	9–10	8	–	–
Abt *et al.* (1991)	22	4–9	5	−3	10
Morell and Levato (1991)	11	2–9	3–9	−16	12
This paper	6	1–3	42–71	1	4

The observations by Struve and Titus (1944) are of particular value. They are not only highly accurate, but also were performed on every clear night over a period of 45 days. These observations have yet another important feature. The paper presents individual velocity measurements by each of the authors. This increases the accuracy and makes it possible to estimate the internal measurement error σ_1, which is given in Table 1. This error can be used to estimate the significance of the period: if the scatter of measurements σ_2 about the theoretical radial velocity is approximately equal to the error, then the period found is correct.

Our observations are the most accurate, but they are few in number and were performed with a larger sampling interval. Nevertheless, our observations are in good agreement with those of Struve and Titus (1944) and with the final theoretical radial-velocity curve (see Table 1).

The remaining observations have a comparatively low accuracy and a significant sampling interval. For these reasons, they are difficult to use in searching for a period. This is clearly seen from an examination of the last two columns in Table 1. They give the mean deviations of the observations from the final theoretical radial-velocity curve, Δ, and rms deviations of the observations from the theoretical curve with a 20.2675-day period.

Periodicities in the radial-velocity variations were analyzed in two steps. First, we constructed a periodogram that allowed several regions with a probable period to be separated. Subsequently, we fitted the parameters of the radial-velocity curve in each of the separated regions by least squares.

The periodogram was constructed by a direct period-by-period examination. We constructed the phase curve for each period from all observations, which was then broken down into fragments. Subsequently, we determined the deviation from the mean value in each fragment. The minimum mean deviation was assumed to be evidence of a probable period. We found about ten probable periods, but the smallest mean deviation was for periods near 20.25 and 40.5 days.

Figure 1 shows the radial-velocity curve whose parameters are listed in the second column of Table 3. In this table, the errors in the parameters, in units

Table 2. The radial velocities measured from IUE spectra

Spectrum no.	JD 2440000+	V_r, km s^{-1}	N
10006	4487.284	13(3)	46
10007	4487.375	12(3)	42
49013	9285.931	39(1)	71
49014	9285.997	37(2)	65
49270	9311.808	32(1)	71
50205	9425.438	31(3)	45

Table 3. Spectroscopic orbital elements

Quantity	P_1	P_2
Period, days	20.2675(10)	40.528(2)
Epoch, JD	2430826.6(1)	2430826.2(3)
γ, km s^{-1}	32.4(10)	35.8(10)
K, km s^{-1}	14.3(15)	13.7(18)
ω, rad	3.3(1)	3.03(12)
e	0.68(9)	0.76(8)
$a_1 \sin i$, 10^7 km	0.30	0.50
f_1, $M_\odot$	0.0025	0.030
Min I	0.933	0.960

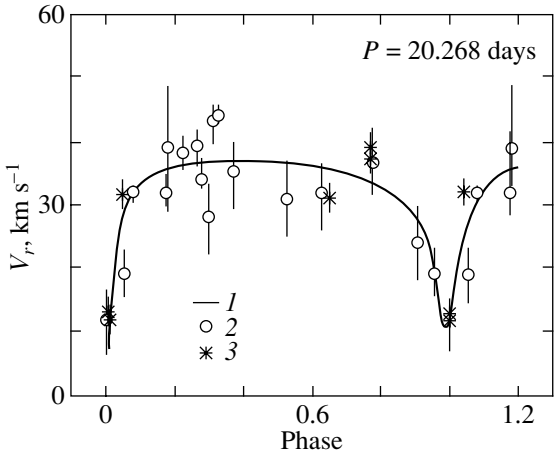

Fig. 1. The radial-velocity curve with a 20.2675-day period. (*1*) The theoretical curve constructed with the elements from the second column in Table 3; (*2*) the observations by Struve and Titus (1944); (*3*) our observations. The error are indicated by bars.

of the last figure, are given in parentheses. The error in counting the epochs is unlikely, because only ~673 cycles passed between the measurements describing the radial-velocity minima. A miscount of a single cycle would be noticeable in the radial-velocity curve.

Figure 2 shows a sample periodogram for a narrow range of periods. In the figure, we see a narrow and sharp minimum that points to one of the probable periods, 40.5 days. The period is along the horizontal axis and the rms deviation of the observations from the theoretical radial-velocity curve constructed by least squares is along the vertical axis. In this case, we used the observations by Struve and Titus (1944) and our observations.

Figure 3 shows the radial-velocity curve with a double period. We had to reject one of the observations from Struve and Titus (1944) by the 3σ criterion. The epoch of this observation is JD 2430804.707. The scatter of observations about the theoretical radial-velocity curve with the new period is virtually the same as for the double period. In constructing Fig. 3, we found that the measurement error was equal to the error in the deviation of the observations from the radial-velocity curve. This convincingly shows that the 40.528-day period is a probable period. However, a close examination of Fig. 3 revealed that there were virtually no observations near phase 0.5. This leads us to conclude that period shorter by a factor of 2 can also be reconciled with the observations, as confirmed by Fig. 1.

The spectroscopic orbital elements for this period are listed in the last column of Table 3. The last row gives the conjunction phase; an eclipse may be expected near this phase.

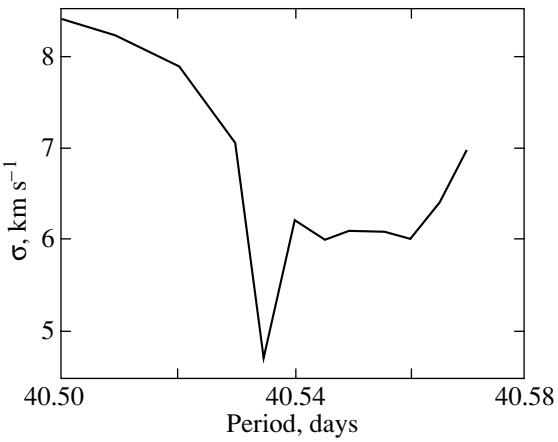

Fig. 2. A portion the periodogram near days 40.54.

DISCUSSION

Which of the two periods is the true period is still the most important question. A critical experiment is a radial-velocity measurement for phase 0.5 at the double period. In this case, it is desirable to measure the radial velocity with an accuracy of ~1 or 2 km s^{-1}. Unfortunately, we have no such measurements at our disposal.

Nevertheless, the 20.2675-day period may be considered to be the true period with a high probability. The point is that the observations by Plaskett and Pearce (1931), Abt *et al.* (1991), and Morell and Levato (1991) exhibit a "cloud" of measurements near phase 0.5 shifted toward lower radial velocities in the curve with the double period. Because of their low

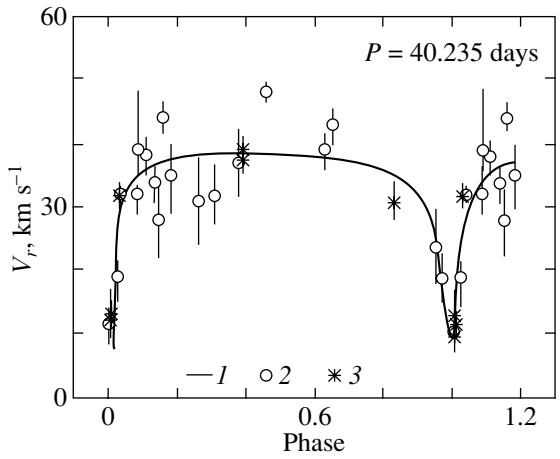

Fig. 3. The radial-velocity curve with a 40.528-day period. The notation is the same as in Fig. 1. The elements of the theoretical curve are given in the last column of in Table 3.

accuracy, these observations show a low correlation, but no such effect is observed at other phases.

ACKNOWLEDGMENTS

I am grateful to I.F. Bikmaev, N.I. Bondar', O.B. Kostina, K.A. Kraush, V.P. Fedotov, and V.V. Tsymbal for a helpful discussion of the problem. I also wish to thank the staff of the IUE archive for putting the spectra at my disposal and to the SIMBAD staff for the opportunity to gather information on the star.

REFERENCES

1. H. A. Abt, R. Wang, and O. Cardona, Astrophys. J. **367**, 155 (1991).
2. N. Z. Ismailov, Pis'ma Astron. Zh. **14**, 327 (1988) [Sov. Astron. Lett. **14**, 138 (1988)].
3. N. Morell and H. Levato, Astrophys. J., Suppl. Ser. **75**, 965 (1991).
4. J. S. Plaskett and J. A. Pearce, Publ. Dom. Astrophys. Obs., Victoria, BC **5** (1) (1931).
5. O. Struve and J. Titus, Astrophys. J. **99**, 84 (1944).
6. E. A. Vitrichenko, Pis'ma Astron. Zh. **28**, 370 (2002) [Astron. Lett. 28, (2002)].

Translated by N. Samus'

Astronomy Letters, Vol. 28, No. 12, 2002, pp. 847–852. Translated from Pis'ma v Astronomicheskiĭ Zhurnal, Vol. 28, No. 12, 2002, pp. 940–946.

A Moderate-Resolution Nasmyth-Focus Spectrograph of the 6-m BTA Telescope

D. N. Monin* **and V. E. Panchuk**

Special Astrophysical Observatory, Russian Academy of Sciences, Nizhnii Arkhyz, Karachai-Cherkessian Republic, 357147 Russia

Received January 14, 2002; in final form, May 29, 2002

Abstract—We report on the development of a fast crossed-dispersion spectrograph (CRAB) mounted at the Nasmyth focus of the 6-m telescope. The spectrograph is designed for visible and near-infrared (3800–10 500 Å) CCD observations with the spectral resolution $R = 4000$. We give the basic parameters of the optical scheme and the parameters of the echelle frame. We determined the gain involved in putting the spectrograph into observational practice and discuss the possible range of spectroscopic problems for which the instrument is optimal. © *2002 MAIK "Nauka/Interperiodica"*.

Key words: *methods of astronomical observations, devices and instruments, echelle spectrograph.*

INTRODUCTION

In the last quarter of the 20th century, altazimuth mountings of optical telescopes were put into astrophysical practice. An advantage of these mountings is the presence of Nasmyth-focus platforms, which allow large instruments to be mounted in a stationary configuration. Nasmyth-focus spectrographs can compete with rapidly developing systems in which a telescope is combined with a spectrograph through optical fibers. Since the 6-m (BTA) telescope has a multiprogram status, each of the programs has a short duration [for the usage statistics of various spectroscopic methods, see Panchuk (1998)]. Therefore, to reduce the operational costs involved in replacing the attached equipment at the prime focus of the telescope, apart from the development of the attached equipment, it is necessary to improve the capabilities of spectrographs mounted at Nasmyth foci in stationary configurations. This program is under way; spectroscopic methods of CCD observations in the range of spectral resolutions $R = 5000$–$60\,000$ have been devised (Panchuk 2001; Panchuk *et al.* 1999a, 1999b). All of the above instruments were mounted at the Nasmyth-2 focus of the BTA telescope. Two interchangeable spectrographs were developed for the Nasmyth-1 focus: a planetary (SP-124) spectrograph (Gusev *et al.* 1976) and a stellar crossed-dispersion spectrograph (Zandin *et al.* 1977), but these instruments were essentially unused. Subsequently, these spectrographs were significantly reequipped to work with one-dimensional and two-dimensional photon counters, respectively (Afanasiev *et al.* 1991; Klochkova and Panchuk 1991).

The reconstructed SP-124 spectrograph with a photon counter, which was equipped with a CCD array in 1995, has been constantly at the Nasmyth-1 focus for more than 20 years. The instrument was difficult to improve further because of its popularity and frequent use. Therefore, it was decided to produce a new spectrograph with parameters that justify the expediency of replacing the old instrument.

THE SPECTROGRAPH SCHEME

In designing a new scheme, we adhered to the following conditions: (a) the spectrograph should be adapted to solve the range of tasks that were previously accomplished with the preceding instrument; (b) it should efficiently use the detector size; (c) it should be able to record the entire spectral range accessible to observation with a given detector; (d) its spectral resolution should complement the capabilities of the existing stationary spectroscopic BTA equipment; and (e) the spectrograph should be easy to prepare for work and to use in observations. We managed to realize these conditions in a crossed-dispersion spectrograph with an echelette operating in low orders, with a prism as the crossed-dispersion element, and with the mirror optics of a collimator and a camera. The optical scheme of the CRAB spectrograph is shown in Fig. 1.

The CRAB spectrograph has the following parameters:

*E-mail: mosha@sao.ru

1063-7737/02/2812-0847$22.00

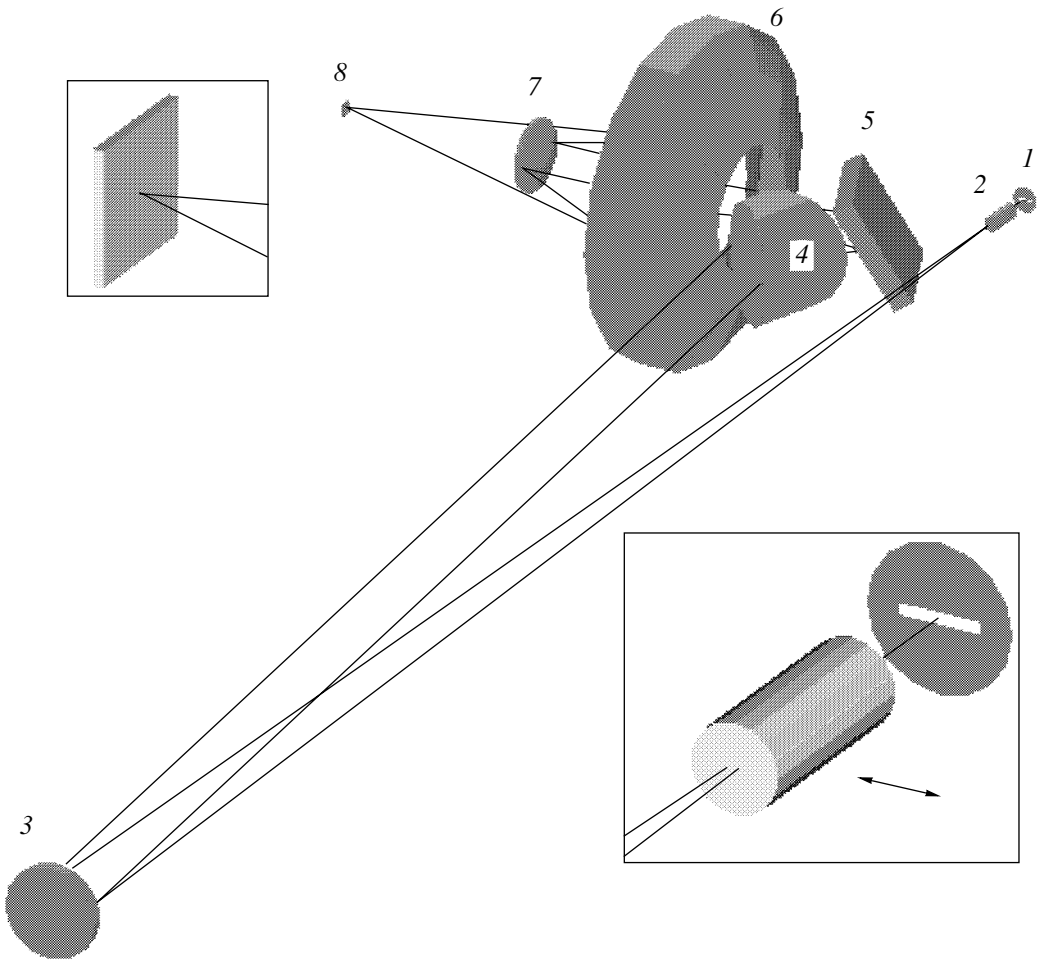

Fig. 1. The optical scheme of the spectrograph: (*1*) slit wheel; (*2*) polarimetric analyzer; (*3*) collimator; (*4*) prism; (*5*) grating; (*6*) and (*7*) large and small camera mirrors, respectively; and (*8*), CCD array. The slit wheel, the polarimetric analyzer, and the CCD array are shown separately in a magnified form. The analyzer is put into and taken out of the beam as indicated by the arrow.

Simultaneously recordable spectral range	3800–10 500 Å
Spectral resolution ($R = \lambda/\delta\lambda$)	4000
Maximum slit height	30″
Collimated-beam diameter	115 mm
Slit width corresponding to two detector pixels	1″
Reciprocal linear dispersion	18–52 Å mm^{-1}

Consider the light-ray path in the spectrograph and the parameters of its individual optical elements. A wheel with slit wheels of various sizes *1* as well as calibration and slit wheel-viewing units are set at the spectrograph entrance. A circular polarization analyzer *2* can be introduced after the slit wheels. In Fig. 1, the slit wheel and the analyzer are shown separately in a magnified form. The spectrograph optics allows us to work with a high slit, i.e., to study extended objects or to effectively take into account the contribution from sky background. The slits are oriented horizontally. A diverging beam falls on a single-mirror collimator *3* ($F = 3500$ mm). Oblique ray incidence on its concave spherical mirror is used. The angle of incidence is $2^{\circ}.8$. At such a small angle and low aperture ratio of the beam, the principal mirror aberrations are unnoticeable. The image elongation due to astigmatism is along the slit height and does not affect the spectrograph resolution.

A moderate spectral resolution over a wide wavelength range during one exposure can be achieved by using the principle of crossed dispersion. Achieving a moderate spectral resolution and, concurrently, a sufficient separation of spectral orders necessitates using an echelle grating with a small blaze angle, echelette *5*, as the main dispersing element (with low working spectral orders). Such a grating and, subsequently, its replica were produced at the Research

Parameters of the spectrum with a 150 lines mm^{-1} grating

m	6	7	8	9	10	11	12	13	14	15	16
D, Å $pixel^{-1}$	1.25	1.07	0.92	0.81	0.73	0.65	0.59	0.54	0.50	0.46	0.43
D, Å mm^{-1}	52	44	38	34	30	27	25	22	21	19	18
λ_c, Å	9820	8430	7400	6610	5970	5450	5020	4660	4350	4080	3850
QE, %	1	3	5	6	5.8	5	3.5	2	1		

Note. QE is the quantum efficiency of the telescope + spectrograph + CCD system. The quantum efficiency was determined from observations of the spectrophotometric standard Feige 34.

Institute of Optical Instrument Building (St. Petersburg). The grating replica has the following parameters: the number of lines per mm is 150 lines mm^{-1}, the working spectral orders are 6–16, and the blaze angle of the working face is $30\overset{\circ}{.}0$. We managed to achieve a reflectance of 70% at blaze maximum by using a special grating-cutting technology.

The prism unit *4* serves to spatially separate echellette orders. The prism material is TF5 optical glass; the prism angle is 50°. The prisms are set at the position of minimum deviation. With such a configuration, the prism transmittance is highest and the clear aperture is used most efficiently. It should be noted that the principle of crossed dispersion makes it possible to achieve the same resolution over the entire spectral range or, in other words, the same resolution in radial-velocity space.

The beam deflected by the prism by 47°, on average, falls on the grating *5* whose center lies on the axis of a Bowen–Popov camera ($F = 182$ mm). The dispersed light falls through a central hole in the large mirror *6* of the camera on its small mirror *7*. After the small mirror, the diverging beam of rays falls on the large mirror and is then focused on detector *8* (the detector CCD array is additionally shown in Fig. 1 in a magnified form). The detector is a Photometrics CCD system with a TK1024 array provided by the Potsdam Institute for Astrophysics (Germany). The detector has the following parameters: the detector size is 1024×1024 pixels, the pixel size is 24×24 μm, the readout noise is 3.5 electrons, and the spectral sensitivity range is 2500–11 000 Å. Since the focal length of the Bowen–Popov camera is large (about 360 mm), the shutter can be placed in the immediate vicinity of the detector.

The basic principles and technical solutions laid in designing the optical scheme and at the production stage of the CRAB spectrograph, as well as testing details, were described in more detail previously (Monin and Panchuk 2001).

RESULTS

We analyzed the principal aberrations and admissible deviations in the positions of individual elements. The results were used to check the quality of the spectrograph assembly and alignment. As a result, we managed to obtain a high-quality spectrum. Figure 2 shows a portion of the comparison spectrum. It exhibits three lines separated by 3.6 and 3.8 Å. The wavelength resolution $\Delta\lambda$ is no lower than 1.4 Å and the spectral resolution R is, accordingly, no lower than 4200.

We took spectra of the planetary nebula NGC 6543. The bright central part of the nebula is 25″ in size. The spectra were obtained with a 30″-high slit. The slit position angle was 328°. The echelle-frame parameters are given in the table.

The spectrum exhibits numerous nebular emission lines, as well as the continuum and emission lines of the central star. Paschen hydrogen lines and the seven Balmer lines up to H I λ3835 are recorded simultaneously. Two sample portions of the spectrum for the nebula NGC 6543 are shown in Figs. 3 and 4. They, respectively, present part of the ninth spectral

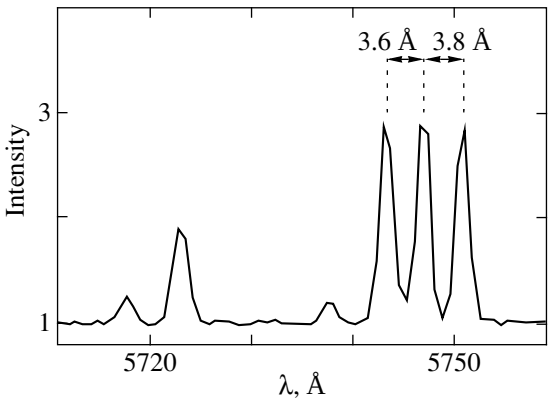

Fig. 2. A portion of the tenth order of the comparison spectrum demonstrating the spectral resolution with a 150 lines mm^{-1} grating. The intensities are in arbitrary units.

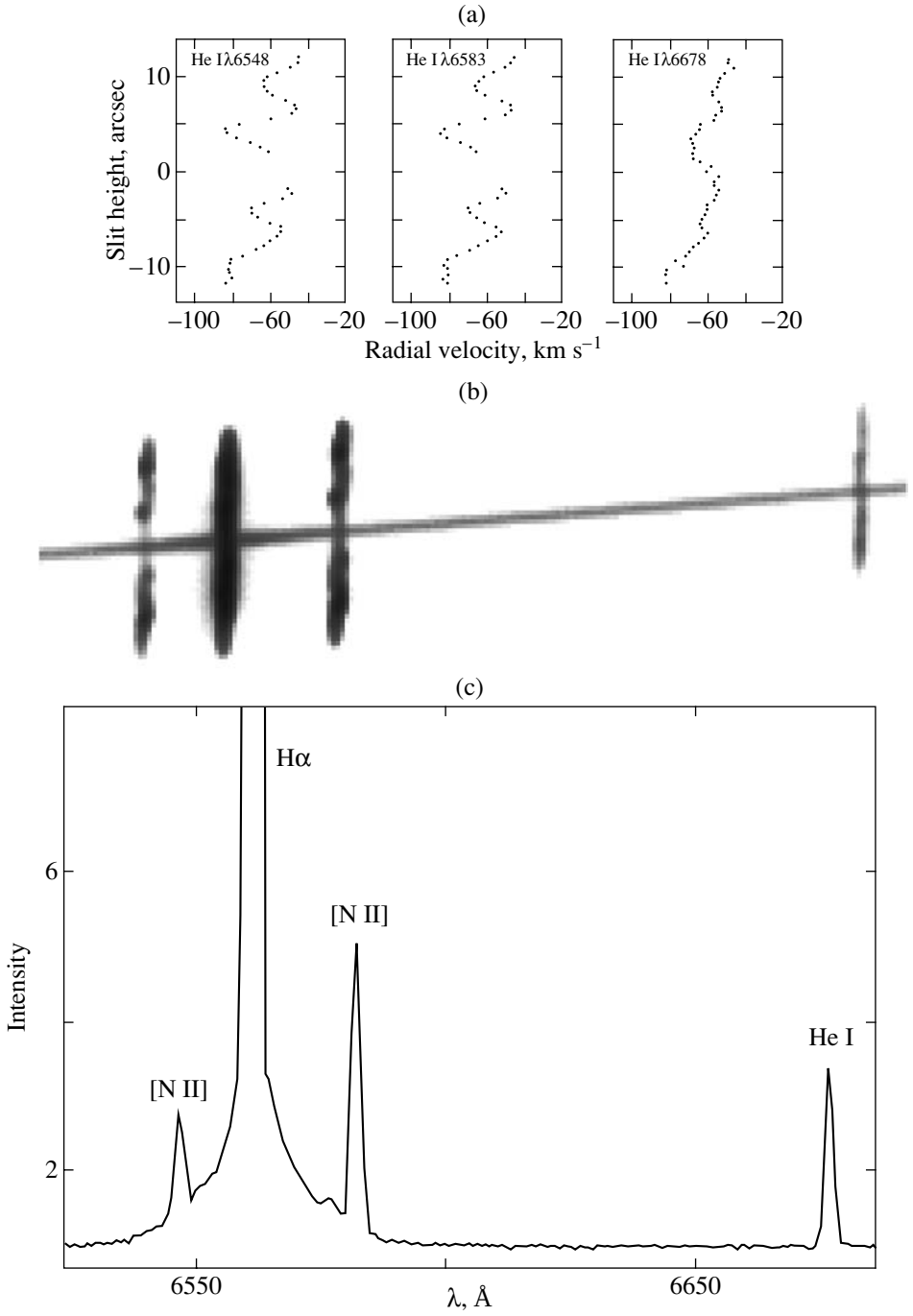

Fig. 3. A portion of the ninth order of the spectrum for the planetary nebula NGC 6543. (a) The radial-velocity behavior along the slit height for three lines: [N II] λ6548, 6583, and He I λ6678. The slit height is measured in arcsecs from the central star. (b) Part of the echelle frame. We see intense nebular emission lines: Hα, [N II] λ6548, 6583, and He I λ6678, as well as the continuum of the central star. (c) The one-dimensional spectrum "central star + nebula." The flux was summed within a 4″-high slit.

order containing the Hα line and part of the tenth spectral order including two intense emission lines, C IV λ5802 and 5812, belonging to the central star. Since the widths of the C IV lines significantly exceed the width of the spectrograph instrumental profile, their detailed structure can be studied.

The nebular emission lines have a complex structure along the slit height, which is different for lines of different elements (Miranda and Solf 1992; Bryce

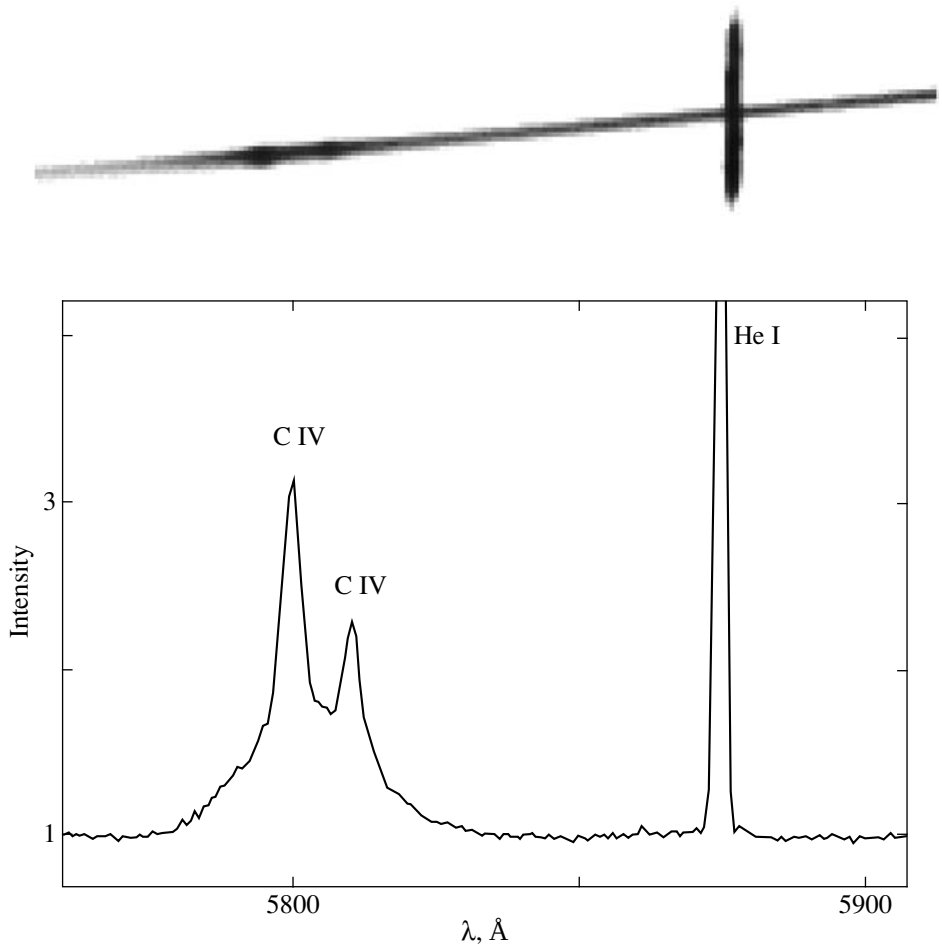

Fig. 4. A portion of the tenth order of the spectrum for the planetary nebula NGC 6543 containing the He I λ5875 line and the C IV λ5802 and 5812 emission lines belonging to the central star. The C IV lines are several times wider than the He I line.

et al. 1992). Figure 3 (upper panel) shows how the radial velocities of individual lines vary along the slit height. The constant component at -64 km s^{-1} is close to the radial velocity of the nebula (Miranda and Solf 1992; Hyung *et al.* 2000). The velocities of different parts of the nebula in the [N II] line differ from the mean velocity by no more than 20 km s^{-1}, which is in agreement with the expansion velocity of the nebula in this line (Hyung *et al.* 2000). As we see from Fig. 3, the radial velocities in the He I and [N II] lines differ in behavior.

The neighboring orders partially overlap, which is important for spectrophotometric studies over a wide wavelength range.

Let us estimate the gain in informativeness of the spectrograph under consideration in comparison with the one used previously. The new spectrograph loses a factor of 1.3 (30″ against the previous 40″) in the number of simultaneously transmitted image elements M. The new spectrograph gains a factor of 11 (11 spectral orders instead of 1) in the number of simultaneously transmitted spectral elements N. Thus, the gain of the new CRAB spectrograph in informativeness (the product MN) is 8.4. The gain in spectral resolution R (with the same slit width) is 5.5 in the blue and 2.1 in the red; we take a factor of 3.8, on average. Let us estimate the gain in quantum efficiency. The detector is the same as that in the old spectrograph, so we exclude the quantum sensitivity parameter from our analysis. The quantum efficiency of the telescope + spectrograph + CCD system varies between 1 and 6% (see the table), being, on average, 3%. For the SP-124 spectrograph, this parameter was 1–1.5% (Neizvestnyi *et al.* 1998). Therefore, the gain of the CRAB spectrograph in quantum efficiency is at least 2.

The theory of spectral devices introduces generalized criteria for comparing both spectrographs of the same type and fundamentally different devices: the quality factor (Jacquinot 1960) and the potential

quality (Meaburn 1976). Following these criteria, to assess the advantages offered by the new spectrograph, the gains in informativeness, spectral resolution, and quantum efficiency can be multiplied. The generalized gain of the CRAB spectrograph in comparison with the previous Nasmyth-1-focus spectrograph is 64.

CONCLUSIONS

In conclusion, we list the possible applications of the CRAB spectrograph by also proceeding from the tasks that remain optimal for other stationary BTA spectrographs:

(1) observations of unexpected low-brightness phenomena (supernova explosions in other galaxies and the like) in those cases where the prime focus of the telescope is occupied by equipment that is less suitable for such observations;

(2) observations in spectrophotometer mode (energy calibration of the spectral elements over a wide wavelength range). Here, a crucial factor is the invariable positions of all optical elements in the spectrograph;

(3) spectropolarimetric observations over a wide wavelength range (the spectropolarimetric equipment on large-diameter telescopes increases in importance);

(4) observations of faint pointlike objects in those cases where it is necessary to simultaneously record a wide spectral range with a moderate resolution (the CRAB spectrograph surpasses prime-focus spectroscopic systems in combination of these parameters, being inferior to them in quantum efficiency); and

(5) observations with a relatively high readout speed in those cases where it is necessary to follow synchronous variations in widely separated spectral features;

(6) the large focal length of the mirror camera and the spectrograph dimensions also allow other detectors that are unsuitable for use in the cabin of the BTA prime focus by their design to be mounted.

Thus, we designed, produced, and tested a new spectrograph, which significantly enhances the capabilities of the 6-m BTA telescope. The spectrograph is mounted on the telescope in a stationary configuration and is easy to maintain and to observe with. We preliminary defined the range of tasks preferred for solving with this instrument.

ACKNOWLEDGMENTS

A.V. Pritychenko helped in adapting the spectrograph to the telescope. The optical elements were assembled and aligned by N.A. Vikul'ev. V.L. Afanasiev gave helpful advice. We wish to thank all of them. The study was supported by the Program "Upgrading the BTA Complex."

REFERENCES

1. V. L. Afanasiev, V. A. Lipovetskii, V. P. Mikhailov, *et al.*, Astrofiz. Issled. (Izv. SAO) **31**, 128 (1991).
2. M. Bryce, J. Meaburn, J. R. Walsh, and R. E. S. Clegg, Mon. Not. R. Astron. Soc. **254**, 477 (1992).
3. O. N. Gusev, N. G. Zandin, and M. V. Lobachev, Opt.-Mekh. Prom–st'. **43** (12), 63 (1976) [Sov. J. Opt. Technol. **43**, 753 (1976)].
4. S. Hyung, L. H. Aller, W. A. Feibelman, *et al.*, Mon. Not. R. Astron. Soc. **318**, 77 (2000).
5. P. Jacquinot, Rep. Prog. Phys. **23**, 267 (1960).
6. V. G. Klochkova and V. E. Panchuk, Preprint No. 70, SAO (1991).
7. J. Meaburn, *Detection and Spectrometry of Faint Light* (Reidel, Dordrecht, 1976).
8. L. F. Miranda and J. Solf, Astron. Astrophys. **260**, 397 (1992).
9. D. N. Monin and V. E. Panchuk, Preprint No. 162, SAO (2001).
10. S. Neizvestnyi, A. Knyazev, V. Shergin, *et al.*, Instruction on Observations for SFK N-1 (SAO RAN, 1998).
11. V. E. Panchuk, Bull. Spec. Astrophys. Obs. **44**, 65 (1998).
12. V. E. Panchuk, Preprint No. 154, SAO (2001).
13. V. E. Panchuk, V. G. Klochkova, I. D. Naidenov, *et al.*, Preprint No. 139, SAO (1999a).
14. V. E. Panchuk, V. G. Klochkova, and I. D. Naidenov, Preprint No. 135, SAO (1999b).
15. N. G. Zandin, O. N. Gusev, and I. V. Peisakhson, Opt.-Mekh. Prom–st'. **44** (6), 20 (1977) [Sov. J. Opt. Technol. **44**, 336 (1977)].

Translated by V. Astakhov

Astronomy Letters, Vol. 28, No. 12, 2002, pp. 853–856. Translated from Pis'ma v Astronomicheskiĭ Zhurnal, Vol. 28, No. 12, 2002, pp. 947–951.

Localization of the Solar Flare SF900610 in X-rays with the WATCH Instrument of the GRANAT Observatory

O. V. Terekhov[1*], A. G. Kuzmin[1], A. V. Shevchenko[1], S. Yu. Sazonov[1,2], R. A. Sunyaev[1,2], and N. Lund[3]

[1] *Space Research Institute, Russian Academy of Sciences, Profsoyuznaya ul. 84/32, Moscow, 117810 Russia*

[2] *Max-Planck-Institut für Astrophysik, Karl Schwarzschild Strasse 1, Garching bei München, 86740 Germany*

[3] *Danish Space Research Institute, Copenhagen, Denmark*

Received June 11, 2002

Abstract—During the solar flare of June 10, 1990, the WATCH instrument of the GRANAT space observatory obtained 110 localizations of the X-ray source in the X-ray range 8–20 keV. Its coordinates were measured with an accuracy of ~2 arcmin at a 3σ confidence level. The coordinates of the X-ray source do not coincide with the coordinates of the Hα-line flare. The X-ray source moved over the solar disk during the flare. This probably implies that, as the X-ray emission was generated, different parts of one loop or a system of magnetic loops dominated at different flare times. © *2002 MAIK "Nauka/Interperiodica"*.

Key words: *the Sun, X-ray and gamma-ray sources*.

INTRODUCTION

The WATCH instrument of the GRANAT observatory designed at the Danish Space Research Institute (Lund 1985; Brandt *et al.* 1990) is an all-sky monitor. It is capable of simultaneously observing a significant part of the sky. A total of four identical WATCH detectors pointing in different directions were installed on the GRANAT observatory. The field of view of each detector corresponds to a cone with an opening angle of about 65°. Each detector includes a rotating modulation collimator (Schnopper *et al.* 1968). A distinctive feature of the design in comparison with the standard rotating collimator (Mertz 1968) is the absence of a second rotating lattice. Instead, the detector consists of parallel NaI (Tl) and CsI (Tl) scintillator strips, which allows the effective area to double compared to conventional detectors based on a rotating collimator (Lund 1981). The width of the scintillator strips and the lattice width are 5 mm. The modulation collimator rotates with a period of 1 s. The distance between the scintillator and the collimator is 50 mm. The detector diameter is 110 mm. To avoid exposure to visible light, the scintillator is covered from above with a 25-μm-thick aluminum foil transparent to X-rays with energies above 8 keV. The scintillator is viewed by a photomultiplier. The signals from the two types of scintillators were separated because of the difference between the characteristic pulse rise times. The total effective area along the detector axis is about 30 cm^2 in the energy range from ~8 to ~60 keV. The detector carried out continuous monitoring in two energy channels, ~8–20 and ~20–60 keV.

The GRANAT observatory was launched into a high-apogee orbit in December 1989. The revolution period of the satellite around the Earth was 4 days. The perigee and apogee of the orbit were 2000 and 200 000 km, respectively. Most of the time, such an orbit was outside the Earth's radiation belts. This allowed continuous observations to be carried out for ~3 days on each turn. Various astrophysical objects were observed by the SIGMA and ART-P telescopes from the GRANAT observatory in triaxial stabilization mode. The duration of a standard observing session was about one day. Data on the solar flares detected by the GRANAT observatory in the energy range from 100 keV to 100 MeV are given in Terekhov *et al.* (1996).

LOCALIZATION OF THE X-RAY SOURCE OF THE JUNE 10, 1990, SOLAR FLARE

The coordinates of the active region of this event on the solar disk were determined from optical Hα-line observations (Solar Geophysical Data 1990). The latitude of the active region is N09 and its longitude is W17 (the distance from the central meridian of the Sun); the optical class of the flare is SF. The serial number of the active region with which this flare was associated is A6089 (NOAA/USAF sunspot group

[*] E-mail: tern@hea.iki.rssi.ru

1063-7737/02/2812-0853$22.00

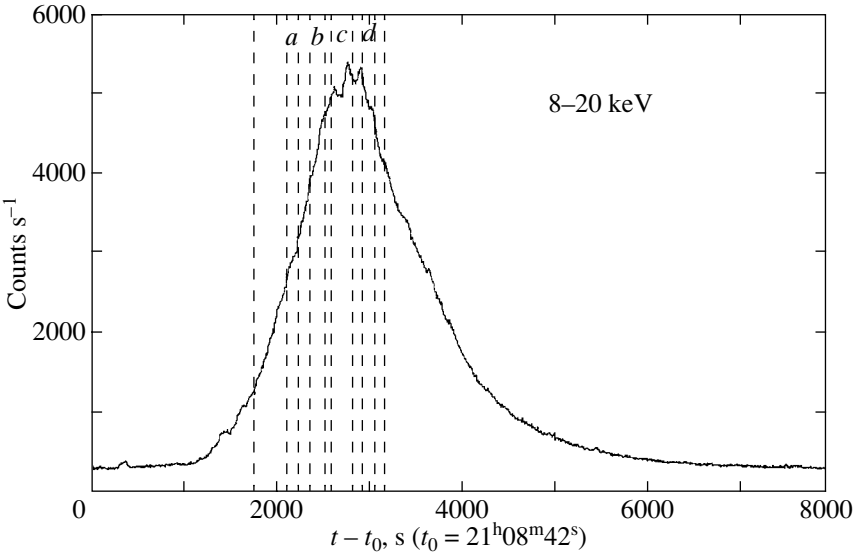

Fig. 1. The 8- to 20-keV light curve of the solar flare as constructed from the the WATCH data.

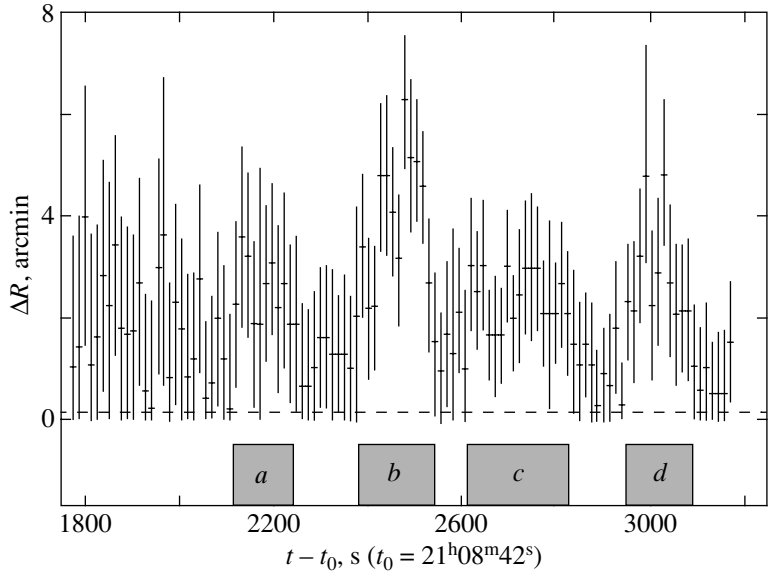

Fig. 2. Variation of the distance between the positions of the localization regions of X-ray (8–20 keV) radiation and the position of the Hα-line flare (in arcmin).

number). The X-ray class of this solar flare is M1.7. The time history of the X-rays flux detected in two energy channels on the GOES-6 satellite is shown in Fig. 1 from Terekhov *et al.* (2002).

The WATCH light curve of the solar flare in the energy range 8–20 keV is shown in Fig. 1. The 1430-s-long time interval during which 110 coordinates of this event were determined on the solar disk using the WATCH 8–20 keV X-ray data is highlighted in Fig. 1 by the dashed lines. During the flare, the WATCH instrument detected no significant excess of the count rate above the background level in the energy range 20–60 keV (Terekhov *et al.* 2002).

The evolution of the deviations of the WATCH coordinates for the flare from its coordinates in the Hα line is shown in Fig. 2. The flare coordinates in this line correspond to zero on the y axis. The measurement error of the coordinates shown in the figure is 1σ. At least four time intervals for which the X-ray coordinates of the flare source significantly differ from the flare coordinates in the Hα line can be identified in the data obtained. These intervals are shown in Fig. 2 and are denoted by the letters *a, b, c*,

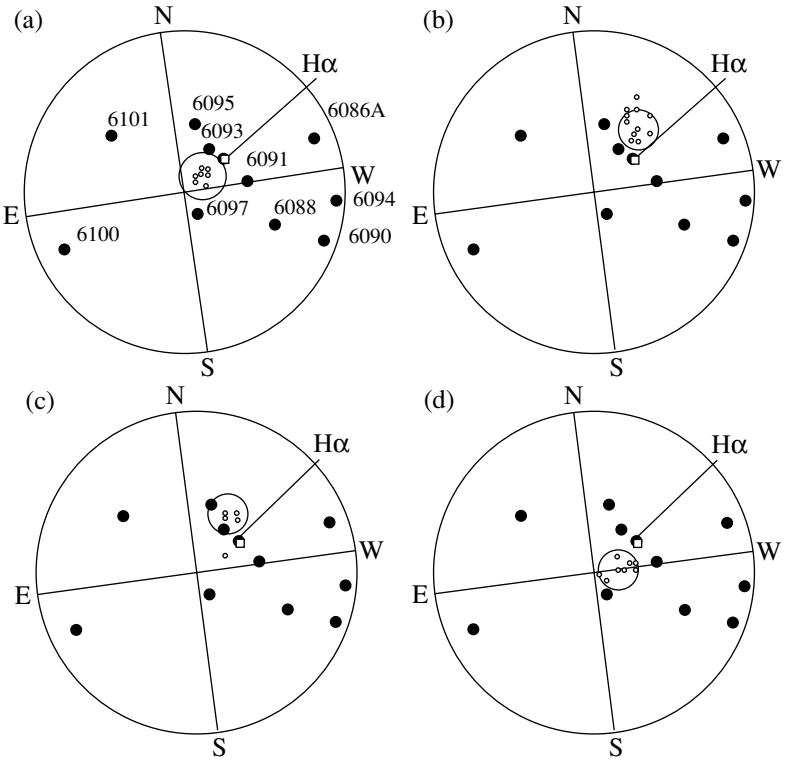

Fig. 3. The localization coordinates of X-ray sources on the solar disk obtained by the WATCH instrument for the corresponding time intervals *a, b, c*, and *d* indicated in Fig. 1. The filled circles represent active regions. An error circle (at a 3σ confidence level) is shown for one of the localizations in each figure.

and *d*. Note that the flare coordinates determined from X-ray data do not vary randomly, as one might expect in the case of a large statistical error, but undergo quite stable variations on a time scale of ~200–300 s. Each value is obtained in ~13 s.

The localizations of the X-ray source on the solar disk in each of these four time intervals denoted by the letters *a*, *b*, *c*, and *d* in Fig. 2 are shown separately in Figs. 3a, 3b, 3c, and 3d. The active regions on the solar disk (Fig. 3) are represented by filled circles. The coordinates of these active regions were taken from Solar Geophysical Data (1990). The points denote the WATCH localizations. The error circle at a 3σ confidence level is given for one of the X-ray coordinates in each group. No error circles of the remaining localizations are shown in Fig. 3 so as not to overload the figure. The square denotes the flare region in the Hα line.

DISCUSSION

During flares, the Sun can be an extremely intense X-ray source. The count rate in the WATCH detector during the solar flare SF900610 reached 5000 counts s^{-1}. At such fluxes, the statistical error in the WATCH coordinates of a source is small compared to the systematic errors and inaccuracies related to changes in the spatial orientation of the spacecraft during the measurement period come to the fore.

We checked the effect of changes in the GRANAT orientation on the WATCH coordinates. For this purpose, we used data from the star tracker of the SIGMA telescope. The GRANAT orientation changed appreciably during the flare, but these changes were smooth with characteristic rates of about $0\overset{\circ}{.}5$ in ~1000 s. Thus, in the time during which data were accumulated for one X-ray image (13 s), the changes in the GRANAT orientation were ~0.4 arcmin, which is much smaller than the WATCH localization errors (2 arcmin).

In analyzing our data on the flare localization, we can assume that the X-ray sources in the energy range 8–20 keV are located inside the flare loops. This, in turn, implies that the X-ray sources can be at large heights (up to several hundred thousand kilometers from the solar surface). Previously (Terekhov *et al.* 2002), we estimated the size of the magnetic loop, $\sim(1-3)\times10^{10}$ cm, responsible for the X-ray flux oscillations with a period of 143.2 s. Analyzing Fig. 3, we can assume that the X-ray sources of the solar flare SF910610 in the energy range 8–20 keV are several magnetic loops that connect the

active region A6089 with nearby active regions. As we see from Fig. 3, the distances between A6086 and neighboring active regions are $\sim(0.7–1.1) \times 10^{10}$ cm. Note an interesting feature noticeable when analyzing Fig. 2: basically, the coordinates of the X-ray source do not coincide with the coordinates of the Hα flare.

The WATCH instrument observed X-ray emission from behind-the-limb flares. The very fact of their observation supports the opinion that the X-ray source at energies above 8 keV is located far from the solar surface in the flare magnetic loops and not only at their footpoints. The WATCH observations of behind-the-limb solar flares will be considered in more detail in our next papers.

The flare under consideration is not intense. However, we must check whether dead-time effects in the WATCH instrument can cause the motion of a stationary source. The WATCH dead time was estimated from the observations of strong solar flares to be $\sim$25 μs. This value was included in the instrument specifications. Clearly, at a count rate below $\sim$5000 counts s^{-1}, the instrument is well below the saturation mode. However the modulation pattern produced by the detector can be distorted by dead-time effects. We should investigate the question of whether the measured position of the source changes due to its intensity variations. Comparing Figs. 3a and 3d, we can see that the source position does not change, although the count rate during these periods changes almost by a factor of 2 (2700 and $\sim$5000 counts s^{-1}, as we see from Fig. 1). Thus, we conclude that the source position determined by the WATCH instrument does not change significantly at count rates below 5000 counts s^{-1}.

Note that the localizations given here were determined for point X-ray sources in solar flares. For extended sources, the uncertainties in the coordinates must be increased in accordance with the source size. In this case, our results refer to the centroids of extended X-ray sources on the Sun.

Note also that the solar-flare localizations described here were obtained by using data from the star tracker of the SIGMA telescope. Previously, the WATCH detectors were referenced to the star tracker of the SIGMA telescope (Sazonov *et al.* 1998). The uncertainty in this referencing does not exceed $\sim$2 arcmin. This systematic error can not affect our results.

Thus, our observations suggest that the X-ray source moved over the solar disk during the flare. This probably implies that, when the X-ray emission was generated, different parts of one loop or a system of magnetic loops on the Sun dominate during different flare periods.

ACKNOWLEDGMENTS

This work was supported by the Russian Foundation for Basic Research (project no. 00-02-17251) and the Program of the Russian Academy of Sciences "Astronomy: Nonstationary Astrophysical Objects." We wish to thank the Foundation for Assistance to Russian Science. We are grateful to S.A. Grebenev for helpful remarks.

REFERENCES

1. S. Brandt, N. Lund, and A. R. Rao, Adv. Space Res. **10**, 239 (1990).
2. N. Lund, Astrophys. Space Sci. **75**, 145 (1981).
3. N. Lund, Proc. SPIE **597**, L95 (1985).
4. L. Mertz, Proc. Symp. Mod. Opt. **17**, 787 (1968).
5. S. Yu. Sazonov, R. A. Sunyaev, O. V. Terekhov, *et al.*, Astron. Astrophys., Suppl. Ser. **129**, 1 (1998).
6. H. W. Schnopper, R. I. Thompson, and S. Watt, Space Sci. Rev. **8**, 534 (1968).
7. Solar Geophysical Data, http://rsd.gsfc.nasa.gov/goes (1990).
8. O. V. Terekhov, A. G. Kuzmin, R. A. Sunyaev, *et al.*, Pis'ma Astron. Zh. **22**, 403 (1996) [Astron. Lett. **22**, 362 (1996)].
9. O. V. Terekhov, A. V. Shevchenko, A. G. Kuzmin, *et al.*, Pis'ma Astron. Zh. **28**, 452 (2002) [Astron. Lett. **28**, 397 (2002)].

Translated by O. Terekhov